Divertor Power Load Studies in ASDEX Upgrade and TCV

Michael Faitsch

München 2017

Divertor Power Load Studies in ASDEX Upgrade and TCV

Michael Faitsch

Dissertation
an der Fakultät für Physik
der Ludwig–Maximilians–Universität
München

vorgelegt von
Michael Faitsch
aus Deggenhausertal

München, den 02.11.2017

Erstgutachter: Prof. Dr. Hartmut Zohm
Zweitgutachter: Prof. Dr. Harald Lesch
Tag der mündlichen Prüfung: 12.01.2018

Zusammenfassung

Kernfusion ist eine mögliche CO_2 neutrale Quelle für die Stromerzeugung, die in Zukunft sowohl Kernspaltung als auch fossile Brennstoffe ersetzen könnte. Die Wärmebelastung der Wandkomponenten ist eine der wesentlichen Herausforderungen für ein zukünftiges thermonukleares Fusionskraftwerk.
Diese Arbeit stellt Studien über die Wärmebelastung in den Tokamaks ASDEX Upgrade (Garching, Deutschland) und TCV (Lausanne, Schweiz) vor.
Der Effekt von einer externen magnetischen Störung auf die Divertor Wärmebelastung ist in ASDEX Upgrade vermessen und mit Modellierungen verglichen worden. Die Verwendung einer nicht axialsymmetrischen magnetischen Störung führt zu einer toroidalen Variation des Wärmeflusses in L- und H-Mode Plasmen.
Der Einfluss der technischen Umsetzung dieser magnetischen Störung wird in L-Mode Plasmen untersucht. Die Untersuchungen zeigen, dass die toroidale Variation des Wärmeflusses von dem verwendeten poloidalen Spektrum abhängt. Dieses wird durch die differenzielle Phase zwischen den beiden Spulenreihen, die für die Erzeugung der magnetischen Störung benutzt werden, verändert. Die differenzielle Phase mit der größten toroidalen Variation lässt sich mit der Vakuumfeldnäherung beschreiben. Davon ausgehend wird ein Modell zur Beschreibung des Wärmeflusses in Anwesenheit einer magnetischen Störung entwickelt. Dieses Modell gibt den beobachteten Zuwachs der toroidalen Variation mit der Amplitude und eine Verringerung mit ansteigender toroidalen Modennummer des Störfeldes wieder.
Toroidal gemittelte Wärmeflussprofile in Gegenwart einer externen magnetischen Störung sind im Rahmen eines 1D diffusiven Modelles beschrieben und sind vergleichbar zu Wärmeflussprofilen ohne magnetische Störung.
In Plasmen mit erhöhter Dichte wird eine verringerte toroidale Variation des Wärmeflusses gemessen. Dabei wird die lokale Abnahme der Plasmatemperatur im Divertor als Folge der erhöhten Dichte als Ursache identifiziert.
In vorhergehenden Untersuchungen in H-Mode Plasmen wird ein Zusammenhang zwischen dem Pedestal-Druck und der Wärmebelastung durch randlokalisierte Moden (ELMs) beobachtet. Im Rahmen dieser Arbeit wurde dieser Zusammenhang auch in Anwesenheit einer magnetischen Störung bestätigt. Allerdings beeinflusst die externe magnetische Störung die toroidale Position der Wärmebelastung durch ELMs.
Experimente bei TCV zeigen einen Zusammenhang zwischen Triangularität und Plasmatemperatur am Rand. Mit steigender Triangularität und fallender Temperatur am Rand wird eine Zunahme der Leistungsabfalllänge in der Abschälschicht beobachtet. Dies erlaubt eine kürzlich für L-Mode Plasmen in ASDEX Upgrade eingeführte empirische Skalierung zu TCV zu erweitern. Dabei zeigt sich, dass es keinen direkten Einfluss der Maschinengröße auf die Leistungsabfalllänge in der Abschälschicht gibt.

Abstract

Nuclear fusion is a possible CO_2 neutral source for electricity production, potentially substituting both nuclear fission and fossil fuels in the future. Power load onto the wall components is one of the major challenges for a future thermonuclear fusion power plant. This thesis presents divertor power load studies in the tokamaks ASDEX Upgrade (Garching, Germany) and TCV (Lausanne, Switzerland).
The effect of an external magnetic perturbation on divertor power load is measured in ASDEX Upgrade and compared to modelling. The application of a non-axisymmetric magnetic perturbation leads to a toroidal variation of the heat flux in both L- and H-Mode plasmas.
The influence of the technical realization of the magnetic perturbation is studied in L-Mode plasmas. These studies show that the toroidal variation of the heat load depends on the applied poloidal spectrum. This is varied with the differential phase between the two rows of coils used to generate the magnetic perturbation. The differential phase with the largest toroidal variation is in line with the vacuum field approximation. Based on this vacuum field approximation a model describing heat flux in presence of magnetic perturbation is developed. This model reproduces the measured increase of the toroidal variation with the amplitude and a reduction with increasing toroidal mode number of the perturbation field. Toroidally averaged heat flux profiles in presence of an external magnetic perturbation are described by a 1D diffusive model and are comparable to heat flux profiles without magnetic perturbation.
Plasmas with an increased density have a reduced toroidal heat flux variation. The local decrease of the plasma temperature in the divertor caused by the increased density is the identified reason.
Previous studies reported that in H-Mode heat load caused by edge localized modes (ELMs) correlates with the pedestal pressure. In this thesis this correlation is confirmed in presence of a magnetic perturbation. However, the external magnetic perturbation affects the toroidal position of the heat load caused by ELMs.
Experiments in TCV show a correlation between triangularity and plasma temperature at the edge. With increasing triangularity and decreasing temperature at the edge a broadening of the scrape-off layer power fall-off length is observed. A recently established empirical scaling from ASDEX Upgrade L-Mode is extended towards TCV. No direct effect of the machine size on the scrape-off layer power fall-off length is observed.

Contents

Chapter 1

Background and Motivation

1.1 Motivation for Fusion Research as CO_2 Neutral Energy Source

The world wide demand for electricity will most certainly increase in the near future. This has many reasons, most prominent is the overall increase in population in combination with a projected increase of energy consumed per capita. Countries like China and India are currently increasing their life style with respect to energy consumption and hence the overall economic growth. To mitigate further climate change new technologies have to be developed for the limitation of worldwide CO_2 emission. One possible way is the usage of wind and solar energy. Those energy sources, however, require improvements in energy storage and smart electricity grids due to their intermittent power output.
Realistic scenarios combine these intermittent energies with a base load electricity production [Wagner, 2014]. In addition to renewable energies, nuclear fusion might be able to provide a base load substituting both nuclear fission and fossil fuels.
Nuclear fusion is the process of combining two or more nuclei into a heavier nucleus. For light elements the fusion process is exothermic, e.g. helium.
The envisaged fusion reaction for a power plant is the fusion of deuterium (D) and tritium (T):

$$ {}^{2}_{1}\mathrm{D} + {}^{3}_{1}\mathrm{T} \rightarrow {}^{4}_{2}\mathrm{He} + \mathrm{n} + 17.6\ \mathrm{MeV} \tag{1.1} $$

which fuse to a helium nucleus ($^{5}_{2}$He) that decays into $^{4}_{2}$He and a neutron (n), releasing 17.6 MeV of kinetic energy. Deuterium occurs naturally within water, with an isotope concentration of 0.015% [Wesson and Campbell, 2011]. Tritium has a half-life of 12.3 years and therefore does not occur in nature [Wesson and Campbell, 2011]. It can be bred using lithium (Li) and the neutrons from the fusion reaction.

$$ {}^{6}_{3}\mathrm{Li} + \mathrm{n} \rightarrow {}^{3}_{1}\mathrm{T} + {}^{4}_{2}\mathrm{He} + 4.8\ \mathrm{MeV} \tag{1.2} $$

The required lithium is sufficiently available on Earth.

One possible condition to sustain nuclear fusion is the so called thermonuclear fusion which takes place in a thermalized environment.
Due to the high energies needed to overcome the Coulomb barrier high temperature is needed so that the atoms are ionized and in the *plasma* state. For the D-T fusion reaction in a thermal plasma the maximum of the rate coefficient is at a temperature around 14 keV (approximately 150 million K).
The point where a fusion plasma generates enough heating power to run self-sustained without further external heating is called *ignition*. The criterion to reach ignition is given by the so called Lawson criterion [Wesson and Campbell, 2011]. For a deuterium and tritium plasma, ignition is achieved when the product of density n and energy confinement time τ_E meets the following condition:

$$n \cdot \tau_\mathrm{E} \geq 1.5 \cdot 10^{20} \qquad \left[\mathrm{sm}^{-3}\right] \tag{1.3}$$

at a temperature around 25 keV. The energy confinement time τ_E is defined as:

$$\tau_\mathrm{E} = \frac{W}{P_\mathrm{loss}} \qquad [\mathrm{s}] \tag{1.4}$$

where W is stored energy of the plasma and P_loss loss power.
In stars the gravitational forces are sufficient to confine the plasma. On Earth it is possible by magnetic fields using the Lorentz force acting on the charged particles in the plasma. One concept of magnetic confinement fusion is the *tokamak*.

1.2 Magnetic Confinement in a Tokamak

The tokamak is a toroidal device. The three main sets of magnetic field coils of a tokamak are shown in figure 1.1. The toroidal field coils (blue coils) produce a toroidal magnetic field B_tor. Because these coils are closer together at the inner part, B_tor is increasing towards the tokamak center. This leads to a magnetic drift velocity:

$$\boldsymbol{v}_\mathrm{mag} = \left(\frac{m v_\perp^2}{2q} + \frac{m v_{||}^2}{q} \right) \frac{\boldsymbol{B} \times \nabla B}{B^3} \tag{1.5}$$

where m is particle mass, B magnetic field, q electric charge and $v_\perp$ ($v_{||}$) velocity perpendicular (parallel) to the magnetic field. The term with $v_{||}$ arises from the curvature of the field and using:

$$\nabla B = -\frac{\boldsymbol{R}}{|R|^2} B. \tag{1.6}$$

The term with $v_\perp$ arises from the conserved magnetic moment:

$$\mu = \frac{m v_\perp^2}{2B}. \tag{1.7}$$

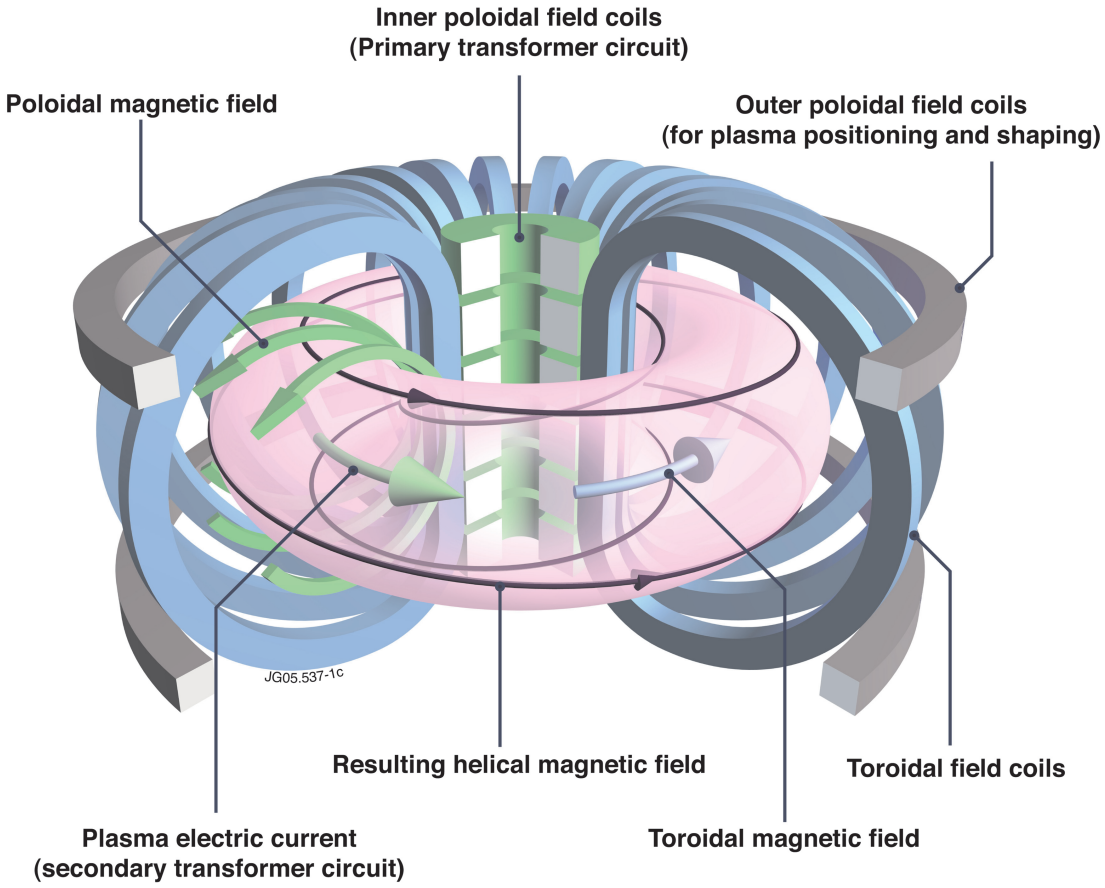

Figure 1.1: Schematic of a tokamak. In grey poloidal field coils, in blue toroidal field coils and green solenoid. Figure taken from [euro-fusion.org, 2011].

The drift direction is dependent on the sign of the electric charge, leading to a vertical separation of electrons and ions and causes an electric field $\boldsymbol{E}$. This electric field leads to an additional drift with velocity:

$$\boldsymbol{v}_{\boldsymbol{E}\times\boldsymbol{B}} = \frac{\boldsymbol{E}\times\boldsymbol{B}}{B^2} \tag{1.8}$$

being independent of electric charge and mass. For a purely toroidal magnetic field this drift is directed radially outwards preventing necessary confinement times.
In order to prevent charge separation a poloidal magnetic field B_{pol} is superimposed, leading to helically wound field lines largely cancelling out the drift by connecting upper and lower part of the plasma. In a tokamak B_{pol} is induced by a toroidal plasma current I_{p}. This plasma current can be induced by a ramp of current in the second set of coils, the central solenoid (green in figure 1.1). The change of current inside the central solenoid induces an electric field (*loop voltage*) inside the plasma vessel in toroidal direction. This leads to a toroidal current as the plasma is an excellent electrical conductor. With a voltage of $U_{\mathrm{loop}} < 10\,\mathrm{V}$ a plasma current of $I_{\mathrm{p}} \approx 1\,\mathrm{MA}$ is sustained in ASDEX Upgrade due to an

effective resistivity of $< 10^{-5}\,\Omega$.
The third set are the poloidal field coils (grey in figure 1.1). They induce a vertical magnetic field, limiting the expansion of the plasma in horizontal direction and are used for position control.
The equilibrium state of a tokamak is described by:

$$\boldsymbol{j} \times \boldsymbol{B} = \nabla p \tag{1.9}$$

with $\boldsymbol{j} \times \boldsymbol{B}$ being the magnetic force density from a current $\boldsymbol{j}$ and magnetic field $\boldsymbol{B}$ and pressure gradient ∇p. This implies that plasma pressure is constant on magnetic flux surfaces and the current flows within these surfaces.
To reach high temperature, required to ignite the fusion process, the plasma is heated. A beneficial aspect of the tokamak is that the induced toroidal current leads to ohmic heating of the plasma. However, due to the reduction of electrical resistivity with temperature, ohmic heating is not sufficient. Additional external heating power can be introduced by e.g. wave heating or neutral particle injection.

L- and H-Mode

In tokamaks it has been found, that above a certain heating power threshold the plasma confinement increases strongly (around a factor of 2). This regime is called H-Mode (high confinement mode) in contrast to L-Mode (low confinement mode) and was first reported at ASDEX [Wagner et al., 1982]. Above a certain heating power a transport barrier forms at the plasma edge [Wagner et al., 1985]. With this barrier a so called *pedestal* forms which has steep temperature and density gradients and increases the global energy confinement. Because of this good confinement H-Mode is the foreseen scenario for future fusion devices such as ITER [ITER Physics Basis Editors et al., 1999] and DEMO [Federici et al., 2014]. The steep pressure gradient together with a high current density leads to an instability that periodically relaxes the pedestal gradients, expelling both particles and energy from the confined region. This magneto hydro dynamic (MHD) instability is called *edge localized mode* (ELM) [Keilhacker et al., 1984].

Divertor

With the before mentioned magnetic field configuration of a tokamak, nested flux surfaces are created in the poloidal plane. The outermost surface that is not in contact with the first wall is called *last closed flux surface*. The configuration is called a *limiter* configuration because the magnetic cage is limited by the first structure that intersects a magnetic flux surface. A poloidal cross-section of ASDEX Upgrade with a limiter configuration is shown in figure 1.2(a). Particles and heat travelling along field lines outside the last closed flux surface will intersect the wall. This induces heat loads and physical sputtering at plasma facing components. Due to the close proximity to the confined plasma, sputtered impurities (wall material, e.g. tungsten) directly penetrate the confined plasma and lead

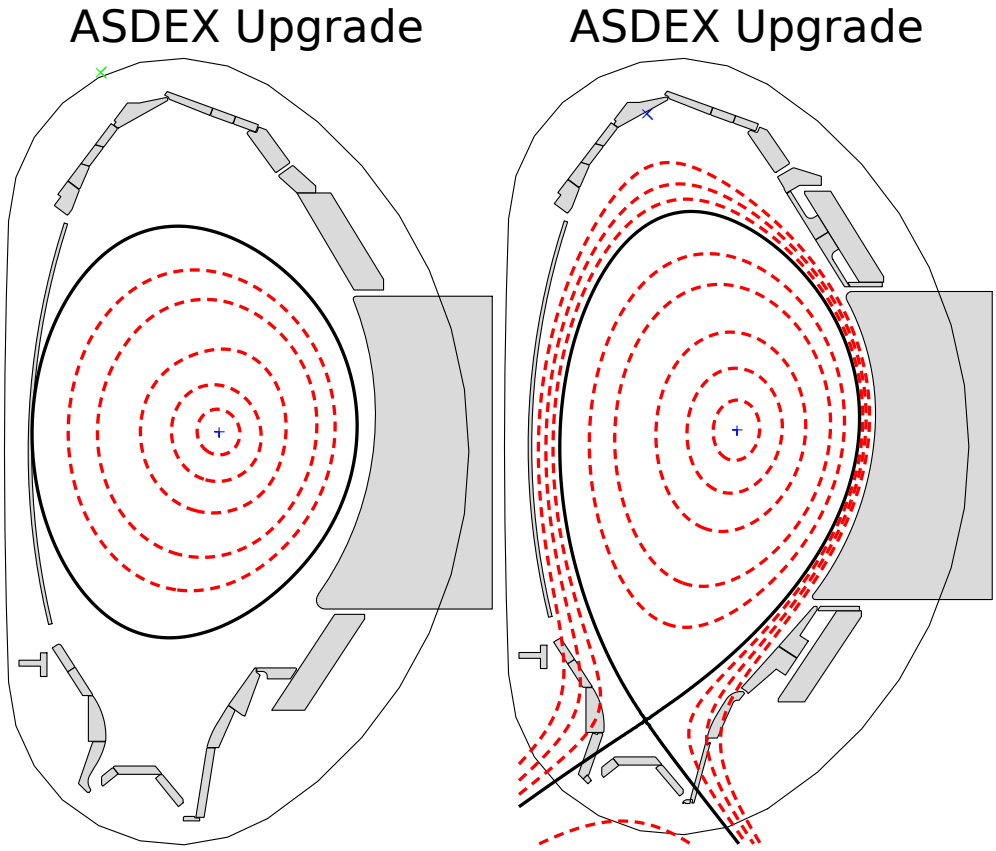

(a) Limiter configuration. (b) Divertor configuration.

Figure 1.2: Poloidal cross-section of ASDEX Upgrade. The black line represents (a) last closed flux surface and b) separatrix as the boundary of the confined region.

to enhanced radiation, dilution and are overall limiting performance.
To separate the confined region and the intersection between field lines and wall, an additional magnetic field is used. Poloidal field coils, being parallel to the toroidal plasma current, are placed above and below the plasma chamber. They induce a poloidal magnetic field reducing the field from the plasma current. This leads to two points where the poloidal flux is zero.
If one (or both) of this null-points, often referred to as *X-point*, is at a flux surface closer to the plasma center than the limiter, a new configuration is created. The flux surface containing the X-point is called *separatrix*. Plasma outside the separatrix follows field lines in the so called *scrape-off layer* and intersects the wall at the *divertor* target. Typical plasmas in ASDEX Upgrade and TCV are not up/down symmetric and only one of the null points is connected to the separatrix (*single null* configuration). For a standard ASDEX Upgrade plasma this is the lower one, as shown in figure 1.2(b).
Due to the increased distance of the divertor target to the confined region compared to the limiter, better performance is achieved (such as H-Mode), making the divertor con-

cept fundamental for future power plants. The divertor has multiple purposes, exhaust of power, pumping exhaust gas including helium ash and retention of impurities created by plasma wall interaction. The divertor can achieve higher neutral pressure compared to a limiter, favouring both pumping as well as power exhaust. The divertor target plates have to withstand high particle and heat loads.

1.2.1 The Challenge of Power Exhaust for Next Step Devices

In a fusion device such as a tokamak, optimal temperature is determined by the cross-section of the fusion reaction. The density n is limited by the so called Greenwald density limit which is an empirical limit found in tokamaks [Greenwald, 2002]. For a given safety factor q and toroidal magnetic field B_{tor}, n decreases with major radius R [Pamela et al., 2009]. Therefore, increasing confinement time is a possibility to increase the product $n \cdot \tau_{\mathrm{E}}$ to fulfil the Lawson criterion, equation (1.3). Energy confinement time increases e.g. with size of the machine and can change with different operational regimes (e.g. H-Mode). For operation in H-Mode energy confinement time is found to scale as [ITER Physics Expert Group on Confinement and Transport et al., 1999]:

$$\tau_{\mathrm{E}} \propto R^2 I_{\mathrm{p}} \tag{1.10}$$

with major radius R and plasma current I_{p}.
With increased machine size, power exhaust is becoming a more and more challenging task. The exhausted power increases strongly with machine size (major radius R). Fusion power by α particles, the dominating heating source in future power plants, increases with R^3 [Zohm, 2010]. Using the toroidal symmetry of a tokamak the area A onto which power is exhausted is expressed as:

$$A = 2\pi R_{\mathrm{div}} f_{\mathrm{tor}} \lambda_{\mathrm{int}}^{\mathrm{tgt}} \tag{1.11}$$

with R_{div} major radius of the divertor, f_{tor} toroidal wetted fraction and $\lambda_{\mathrm{int}}^{\mathrm{tgt}}$ extent of the wetted area along the divertor target, perpendicular to the toroidal direction.
Heat exhaust studies aim at understanding and predicting $\lambda_{\mathrm{int}}^{\mathrm{tgt}}$ in order to estimate the wetted area for a given machine size. For $\lambda_{\mathrm{int}}^{\mathrm{tgt}} \propto R^{\alpha}$ with $\alpha < 2$ heat exhaust becomes more challenging with larger devices.
In addition to steady state heat load, transient thermal loads due to ELMs in the foreseen H-Mode operation occur. In smaller devices like ASDEX Upgrade these loads are acceptable for the material. However, in next step devices like ITER, unmitigated, natural ELMs might limit the lifetime of the divertor significantly [Loarte et al., 2003].
Applying a non-axisymmetric external magnetic perturbation (MP) is one technique that is studied in order to mitigate or suppress large ELMs [Evans et al., 2004, Lang et al., 2013, Loarte et al., 2014]. It is observed that a radial magnetic field can be used to control the plasma edge parameters in such a way, that particularly large ELMs are substituted by a number of smaller ELMs or suppressed. Many of today's tokamak experiments are equipped with magnetic perturbation coils to study the physics and feasibility of ELM

mitigation/suppression with an external magnetic perturbation, e.g. ASDEX Upgrade [Suttrop et al., 2009a], DIII-D [Evans et al., 2004], EAST [Sun et al., 2016], JET [Liang et al., 2007], KSTAR [Jeon et al., 2012], MAST [Kirk et al., 2015] and NSTX [Ahn et al., 2010].
The application of an external magnetic perturbation not only affects ELMs but also steady state heat flux in between ELMs and in L-Mode.

1.3 Scope of this Thesis

Applying an external magnetic perturbation breaks the axisymmetry of a tokamak and leads to a toroidally varying heat flux pattern on the divertor target [Jakubowski et al., 2009, Ahn et al., 2010, Harting et al., 2012, Müller et al., 2013, Thornton et al., 2014]. In this thesis divertor heat flux is investigated in L-Mode conditions as well as H-Mode with the focus on changes in steady state heat flux compared to heat flux without a magnetic perturbation present. An ad hoc model is developed in order to have a quantitative comparison. The key questions addressed in this thesis are:

- How does the application of a magnetic perturbation change scrape-off layer heat transport?
- How does transport in the divertor region change the heat flux pattern on the divertor target in presence of an external magnetic perturbation?
- What are the differences between L-Mode and inter-ELM heat fluxes in presence of an external magnetic perturbation?
- How are ELM heat loads affected by the application of a magnetic perturbation?

A second aspect of this thesis is the scrape-off layer width and its dependence on plasma geometry. This is investigated in TCV, a medium sized tokamak at the Swiss Plasma Center in Lausanne, Switzerland. This tokamak has a unique capability for plasma shaping and is therefore the ideal device to study geometry effects on heat exhaust. The key question addressed in this thesis is:

- How does the plasma triangularity affect the scrape-off layer width?

In chapter 2 relevant aspects of fusion research, focusing on power exhaust, are introduced as well as the two devices on which the experiments were carried out. Chapter 3 introduces the main diagnostics, infrared thermography, used for the experimental studies as well as an ad hoc model describing divertor heat flux in presence of an external magnetic perturbation developed within this thesis. Chapter 4 reports on experimental studies in ASDEX Upgrade in presence of an external magnetic perturbation, chapter 5 on experimental studies in TCV with varying triangularity. Summary and conclusion are presented in chapter 6.

Chapter 2

Selected Aspects of Fusion Research with Emphasis on Power Exhaust

In this chapter relevant aspects of power exhaust, the terminology for this thesis and the two devices on which the experiments were carried out, are introduced.

2.1 Scrape-Off Layer Heat Transport

The main focus of this thesis is on divertor heat flux measurements. This heat flux flows from the plasma core into the scrape-off layer down to the divertor target. The scrape-off layer width is very small due to the stronger parallel than perpendicular transport along magnetic field lines. In this section an overview over scrape-off layer heat transport and the challenges for power exhaust are presented. The heat flux is divided into two main categories, quasi steady state and transient. Quasi steady state heat flux occurs in both L-Mode and in between ELMs in H-Mode. The discussed transient heat fluxes occur only in H-Mode due to ELM crashes. Since the origin, time scales and risks are of different nature they are discussed separately.

2.1.1 Steady State Heat Flux

Due to the axisymmetry of a tokamak, steady state heat flux is discussed as a 2D problem in the scrape-off layer volume and 1D on the divertor target. The influence of introducing a non-axisymmetric magnetic perturbation is discussed in section 2.2. Quasi steady state heat flux is observed in L-Mode as well as in between ELMs (inter-ELM) in H-Mode with only slow variations in heat flux characteristics. Fast modulations caused by turbulence fluctuations are not considered here and assumed to be averaged faster than the typical measurement time scale. In next step fusion devices, where actively cooled components have to be used due to the long pulse duration, steady state peak heat flux q_{max} on the

divertor target is limited to

$$q_{\max}^{\text{limit}} = 5 - 10 \left[\frac{\text{MW}}{\text{m}^2}\right] \tag{2.1}$$

for nowadays components [Loarte et al., 2007, Riccardi et al., 2011, Wenninger et al., 2014].

2.1.1.1 Conductive Heat Transport

In the experimental scrape-off layer conditions used in this thesis, parallel heat flux is dominated by electron conduction. The so called *two point model* is often used as a simple tool to estimate the relation between *upstream* and *downstream*. Upstream is considered to be well above the X-point and often taken as a single point at the outer mid-plane. This is done because the outer mid-plane is the area with the most unfavourable curvature in the poloidal plane and therefore thought to have the most transport generated [Gunn et al., 2007]. Downstream is considered to be the divertor target for a diverted plasma. Typically it refers to the outer divertor target, mainly because this is found to be the more challenging one with higher heat flux compared to the inner [Pitts et al., 2005, Eich et al., 2005].
Parallel heat flux $q_{||}$ is calculated using Spitzer-Härm electron conduction:

$$q_{||} = -\kappa_0 T_\text{e}^{\frac{5}{2}} \frac{\text{d}T_\text{e}}{\text{d}x} \tag{2.2}$$

with x coordinate along field lines, T_e electron temperature and κ_0 the constant for electron conduction [Stangeby, 2000]. In the scrape-off layer of a typical tokamak, e.g. ASDEX Upgrade with an effective charge $Z_\text{eff} \approx 2$, $\kappa_0 \approx 2000 \frac{\text{W}}{\text{m}\cdot\text{eV}^{\frac{7}{2}}}$ [Kallenbach et al., 2001]. Integrating along x leads to a relation between upstream temperature T_u and downstream (target) temperature T_tgt with field line length L_OMP:

$$T_\text{u} = \left(T_\text{tgt}^{\frac{7}{2}} + \frac{7 q_{||} L_\text{OMP}}{2\kappa_0}\right)^{\frac{2}{7}}. \tag{2.3}$$

Neglecting downstream electron temperature ($T_\text{tgt} \ll T_\text{u}$)[1]:

$$T_\text{u} \approx \left(\frac{7 q_{||} L_\text{OMP}}{2\kappa_0}\right)^{\frac{2}{7}} \tag{2.4}$$

$$q_{||} \approx \frac{2}{7} \frac{\kappa_0 T_\text{u}^{\frac{7}{2}}}{L_\text{OMP}}. \tag{2.5}$$

Attached conditions are considered in this derivation, with constant pressure along field lines and absence of dissipation due to volumetric losses, e.g. radiation, charge exchange

[1] As a typical H-Mode (L-Mode) example from ASDEX Upgrade with $T_\text{u} = 100$ (50) eV and $T_\text{tgt} = 20$ eV the relative error is $4 \cdot 10^{-3}$ ($4 \cdot 10^{-2}$) and is therefore in most cases well justified.

processes or recombination.
Using a diffusive ansatz for transport perpendicular to field lines in the scrape-off layer we get exponentially decaying profiles for electron temperature and heat flux:

$$T_\mathrm{e}(s) = T_\mathrm{e,sep} \cdot \exp\left(-\frac{s}{\lambda_{\mathrm{T_e}} \cdot f_\mathrm{x}}\right) \tag{2.6}$$

$$q_{||}(s) = q_{||,0} \cdot \exp\left(-\frac{s}{\lambda_\mathrm{q} \cdot f_\mathrm{x}}\right) \tag{2.7}$$

with $s = 0$ at the separatrix position and $s > 0$ for the scrape-off layer. Values for $s < 0$ are not considered because of closed field lines. The factor f_x is called flux expansion and accounts for a changing poloidal separation between flux surfaces. Inserting these into equation (2.4) and ignoring the different L_OMP along s leads to a ratio between upstream temperature fall-off length $\lambda_{\mathrm{T_e}}$ and power fall-off length λ_q:

$$\frac{\lambda_{\mathrm{T_e}}}{\lambda_\mathrm{q}} = \frac{7}{2}. \tag{2.8}$$

The relation between temperature and power fall-off lengths (equation (2.8)) was shown to be in good agreement for ASDEX Upgrade, comparing H-Mode $\lambda_{\mathrm{T_e}}$ data to a λ_q scaling law [Sun et al., 2015] as well as a direct comparison in L-Mode discharges [Faitsch et al., 2015].

2.1.1.2 Modification due to the Private Flux Region

In the divertor region not only the scrape-off layer is present, but also the private flux region. This is accounted for by rewriting the exponential decay from the previous section to

$$f(s) = \begin{cases} q_0 \cdot \exp\left(-\frac{s}{\lambda_\mathrm{q} \cdot f_\mathrm{x}}\right) & \mathrm{for} s \geq 0 \\ 0 & \mathrm{for} s < 0 \end{cases} \tag{2.9}$$

with $s < 0$ being the private flux region which is not directly filled with heat from the confined region. Since we are interested in divertor target heat fluxes, s will be named the *target location* in the following. In order to account for different target geometries and different magnetic field configurations, the flux expansion f_x between target and outer mid-plane is introduced:

$$f_\mathrm{x} = \frac{B_\mathrm{tor}^\mathrm{tgt}}{B_\mathrm{tor}^\mathrm{OMP}} \frac{B_\mathrm{pol}^\mathrm{OMP}}{B_\mathrm{pol}^\mathrm{tgt}} \frac{1}{\sin(\alpha)} \tag{2.10}$$

with B_tor and B_pol toroidal and poloidal magnetic field, respectively and α the poloidal inclination of the divertor target w.r.t. the poloidal projection of field lines. The flux expansion typically is in the order of 5-10, increasing the extent of the heat flux profile in

real space. The flux expansion relates the physical width of the scrape-off layer between outer mid-plane and target.
A shape independent heat flux width is defined as integral power fall-off length λ_{int} to assess the peak heat flux q_{max} [Loarte et al., 1999]:

$$q_{\text{max}} = \frac{P}{2\pi R_{\text{div}} \lambda_{\text{int}} f_{\text{x}}} \tag{2.11}$$

$$\lambda_{\text{int}} \cdot f_{\text{x}} = \frac{\int q(s)\mathrm{d}s}{q_{\text{max}}} \tag{2.12}$$

with P being power impinging on the divertor with major radius R_{div}. Here, the target value is expressed explicitly taking the flux expansion into account ($\lambda_{\text{int}}^{\text{tgt}} = \lambda_{\text{int}} \cdot f_{\text{x}}$).
Taking an exponentially decaying profile as an example heat flux (equation (2.9)) and integrating from $s = 0$ to ∞[2]:

$$\int_0^\infty q(s)\mathrm{d}s = q_0 \cdot \lambda_{\text{q}} \cdot f_{\text{x}} \tag{2.13}$$

and the given definition, λ_{int} is equivalent to λ_q[3].
Additionally, heat is transported in the divertor volume perpendicular to the magnetic field. Assuming transport to be diffusive, with diffusivity parallel $\chi_{||}$ and perpendicular $\chi_{\perp}$ to the magnetic field, we introduce S as the *divertor broadening*:

$$S \cdot f_{\text{x}} = L_{\text{x}} \sqrt{\frac{\chi_{\perp}}{\chi_{||}}} \tag{2.14}$$

with L_{x} being the effective field line length in the divertor region. In 1D this diffusion leads to a Gaussian:

$$g(s) = \frac{1}{S \cdot f_{\text{x}} \sqrt{\pi}} \cdot \exp\left(- \left(\frac{s}{S \cdot f_{\text{x}}} \right)^2 \right) \tag{2.15}$$

with S being related to the standard deviation σ:

$$S \cdot f_{\text{x}} = \sqrt{2}\sigma. \tag{2.16}$$

This definition of the divertor broadening S does not consider volumetric losses due to e.g. radiation, charge exchange or recombination. It characterizes the redistribution of heat due to diffusion without dissipation. The assumption of negligible volumetric losses is justified in low density discharges that are considered in this thesis.
The steady state heat flux profile at the divertor target in attached conditions is described

[2]The negative part ($-\infty$ to 0) is zero and does not contribute.
[3]For the considered one-sided exponential decay, $q_0 = q_{\text{max}}$.

by a convolution between a one-sided decaying exponential, $f(s)$, in the scrape-off layer and a Gaussian, $g(s)$ [Eich et al., 2011]:

$$q(s) = \frac{q_0}{2} \exp\left(\left(\frac{S}{2\lambda_\mathrm{q}}\right)^2 - \frac{s}{\lambda_\mathrm{q} \cdot f_\mathrm{x}}\right) \cdot \operatorname{erfc}\left(\frac{S}{2\lambda_\mathrm{q}} - \frac{s}{S \cdot f_\mathrm{x}}\right) \qquad \left[\frac{\mathrm{MW}}{\mathrm{m}^2}\right] \tag{2.17}$$

with s target location, S divertor broadening, λ_q power fall-off length, f_x flux expansion. For a profile described by equation (2.17) a good approximation for the target extent λ_int is given by [Makowski et al., 2012]:

$$\lambda_\mathrm{int} \approx \lambda_\mathrm{q} + 1.64 \cdot S \tag{2.18}$$

with an accuracy better than 4 % and is often used as a simple approximation between the physics quantities, power fall-off length λ_q and divertor broadening S, and the important quantity for engineering, integral power fall-off length λ_int. Due to the definition of λ_int it is linked to the peak heat load onto the divertor target and is important for the design of plasma facing components in terms of heat removal. The peak heat load, using equation (2.18), is expressed as:

$$q_\mathrm{max} = q_0 \frac{\lambda_\mathrm{q}}{\lambda_\mathrm{q} + 1.64 \cdot S} \tag{2.19}$$

which shows that the divertor broadening S is an efficient way to lower the peak heat load. This effect is shown in figure 2.1. A heat flux profile at the target for different values for

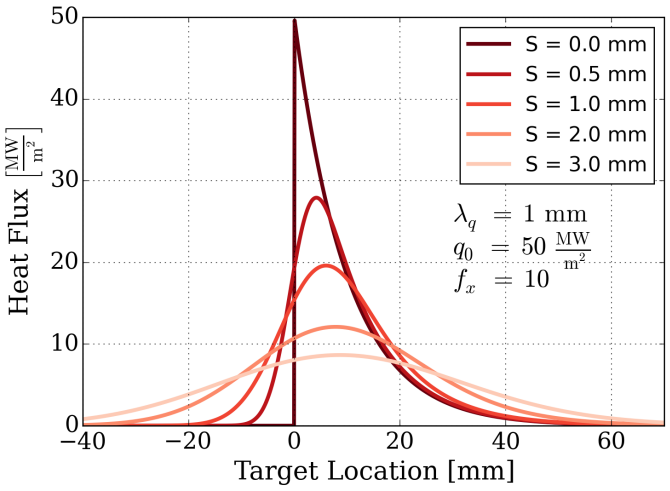

Figure 2.1: Example heat flux onto the divertor target for different values for the divertor broadening S.

the divertor broadening S is shown with $\lambda_\mathrm{q} = 1\,\mathrm{mm}$ and $q_0 = 50\,\frac{\mathrm{MW}}{\mathrm{m}^2}$. With increasing S the profile broadens and the peak heat flux is reduced, with a peak smaller than $10\,\frac{\mathrm{MW}}{\mathrm{m}^2}$ for $S > 3\,\mathrm{mm}$. A sufficiently large S compared to λ_q dominates the overall width of the profile.

2.1.1.3 Scaling Laws

In recent years multiple attempts have been made in order to scale both, λ_q and S. Scaling laws that are used to compare measured data in this thesis are presented in this section.

Power Fall-Off Length Available scaling laws for λ_q measured at the outer divertor target in H-Mode based on a multi machine database show that the poloidal magnetic field at the outer mid-plane B_{pol}^{OMP} is the main quantity determining λ_q without dependence on the machine size [Eich et al., 2013].

$$\lambda_q^{H-Mode,Multi}[mm] = 0.63 \cdot B_{pol}^{OMP}[T]^{-1.19} \tag{2.20}$$

No multi machine scaling for L-Mode exists up to now. However, a scaling law for JET and ASDEX Upgrade was presented [Scarabosio et al., 2013]:

$$\lambda_q^{L-Mode,Scarabosio}[mm] = 1.44 \cdot B_{tor}[T]^{-0.80} \cdot q_{95}^{1.14} \cdot P_{SOL}[MW]^{0.22} \cdot R[m]^{-0.03} \tag{2.21}$$

with B_{tor} toroidal magnetic field, q_{95} edge safety factor, P_{SOL} power crossing the separatrix into the scrape-off layer and R major radius. For JET and ASDEX Upgrade λ_q in L-Mode is about twice that of an H-Mode scaling [Scarabosio et al., 2013, Faitsch et al., 2015, Sieglin et al., 2016b] presented by [Eich et al., 2011]:

$$\lambda_q^{H-Mode,Eich}[mm] = 0.73 \cdot B_{tor}[T]^{-0.78} \cdot q_{cyl}^{1.2} \cdot P_{SOL}[MW]^{0.1} \cdot R[m]^{0.02} \tag{2.22}$$

$$\lambda_q^{L-Mode,Eich} = 2 \cdot \lambda_q^{H-Mode,Eich} \tag{2.23}$$

with B_{tor} toroidal magnetic field, q_{cyl} cylindrical safety factor (see appendix D), P_{SOL} power crossing the separatrix into the scrape-off layer and R major radius. A more recent study at ASDEX Upgrade by [Sieglin et al., 2016b] showed that λ_q in L-Mode is dependent not only on B_{pol} but also on stored energy W_{MHD}, edge electron density $n_{e,edge}$ and main ion mass A (in atomic units u):

$$\lambda_q^{L-Mode,Sieglin}[mm] = 0.15 \cdot B_{pol}[T]^{-0.66} \cdot A[u]^{-0.15} \cdot \left(\frac{W_{MHD}[MJ]}{n_{e,edge}[10^{19}m^{-3}]}\right)^{-0.93}. \tag{2.24}$$

A heuristic drift-based model by [Goldston, 2012] is presented in appendix A and leads to:

$$\lambda_q^{H-Mode,Goldston} = \begin{cases} \frac{4a}{ZeB_{pol}R}\left(\frac{Am_pT_{sep}}{(1+Z)}\right)^{\frac{1}{2}} & \text{ion drift} \\ \frac{4a}{eB_{pol}R}\left(\frac{Am_pT_{sep}}{(1+Z)}\right)^{\frac{1}{2}} & \text{electron drift} \end{cases} \tag{2.25}$$

with A and Z being average ion mass and charge, respectively, T_{sep} separatrix temperature, a and R minor and major plasma radius, B_{pol} poloidal magnetic field and m_p proton mass. This heuristic model is in line with the empirical scaling law (equation (2.22)) in parametric dependencies as well as in absolute size [Eich et al., 2011].
All discussed scaling laws have in common, that λ_q does not or only weekly depend on the machine size (R). Reviewing section 1.2.1 with fusion power increasing with R^3 and the presented scaling laws for λ_q with R^0 shows the importance of heat exhaust investigations.

Divertor Broadening Although the divertor broadening S may be dominating the heat flux profile width in future devices, no scaling law is available combining multiple machines. However, it was shown in modelling as well as experimental work, that the target electron temperature is an important quantity to estimate S [Scarabosio et al., 2015, Sieglin et al., 2016b]. For ASDEX Upgrade with the present divertor Div III [Herrmann et al., 2013] two scaling laws, using different attempts, are described here. Using global discharge parameter that can be predefined for an experiment [Sieglin et al., 2013]:

$$S[\mathrm{mm}] = 0.09 \cdot n_{\mathrm{e,edge}}[10^{19}\mathrm{m}^{-3}]^{1.02} \cdot B_{\mathrm{pol}}[\mathrm{T}]^{-1.01} \tag{2.26}$$

with $n_{\mathrm{e,edge}}$ edge electron density and B_{pol} poloidal magnetic field.
A second scaling uses local divertor quantities [Sieglin et al., 2016b]:

$$S[\mathrm{mm}] = 1.42 \cdot \frac{r_{\mathrm{g}}[\mathrm{mm}]}{f_{\mathrm{x}}} + 2.11 \cdot T_{\mathrm{e,tgt}}[\mathrm{eV}]^{-1.28} \cdot n_{\mathrm{e,tgt}}[10^{19}\mathrm{m}^{-3}]^{0.66} \cdot A[\mathrm{u}]^{-0.84} \cdot B_{\mathrm{pol}}[\mathrm{T}]^{-1.33} \tag{2.27}$$

$$r_{\mathrm{g}} = \frac{\sqrt{2mT}}{eZB} \tag{2.28}$$

with $T_{\mathrm{e,tgt}}$ and $n_{\mathrm{e,tgt}}$ target electron temperature and density, A main ion mass, B_{pol} poloidal magnetic field and r_{g} gyro radius of the main ion species with m and Z mass and charge of the main ion species and e elementary charge, B total magnetic field and assuming equal ion and electron temperature at the target for the scaling $T = T_{\mathrm{e,tgt}}$.
This scaling is in line with parallel electron conduction and a temperature and density independent perpendicular diffusivity as often used in codes, e.g. SOLPS [Scarabosio et al., 2015].
Multi machine scaling laws for S may need detailed information about the temperature distribution in the complete divertor region [Nille et al., 2017], experimentally difficult to assess.

2.1.2 Transient Heat Flux due to ELMs in H-Mode

H-Mode discharges, as foreseen for a reactor, are usually accompanied by edge localized modes (ELMs). ELMs are a magneto hydro dynamic (MHD) instability caused by the pressure gradient together with the current density at the plasma edge in the so called *pedestal* region. ELMs periodically relax the pedestal gradients and expel particles and energy from the confined region into the scrape-off layer. Different types of ELMs are identified; in this thesis only ELMs defined as type-I (see [Zohm, 1996]) are considered.
Type-I ELMy H-Mode is a very attractive operational regime in e.g. ITER due to its good confinement properties and stationary density. Additionally, ELMs help to control the impurity content in the plasma by flushing out impurities [Kallenbach et al., 2005, Dux et al., 2009, Matthews, 2013].
ELMs are a non-axisymmetric phenomenon that lead to non-axisymmetric divertor heat flux profiles [Eich et al., 2003b]. This non-axisymmetry is explained to be due to *filaments*

being expelled upstream at localized toroidal positions and transported field line aligned to the divertor target [Eich et al., 2005]. Divertor heat flux due to ELMs might limit the lifetime of the divertor target in next step devices [Loarte et al., 2003]. The power that is exhausted by type-I ELMs P_{ELM} has been reported to be [Suttrop, 2000, Herrmann, 2002]:

$$P_{\mathrm{ELM}} = \Delta W_{\mathrm{ELM}} \cdot f_{\mathrm{ELM}} \approx 0.2 - 0.3 P_{\mathrm{heat}} \tag{2.29}$$

with ΔW_{ELM} being energy of a single type-I ELM, f_{ELM} ELM frequency[4] and P_{heat} total heating power[5]. In order to mitigate the energy of single ELMs, techniques are investigated increasing the ELM frequency or completely suppressing ELMs [Leonard, 2014]. One of these techniques is the application of an external magnetic perturbation which is discussed in section 2.2.2.

In contrast to steady state heat flux limits, the transient material limits are mainly determined by the surface temperature increase due to the short time scale (about one ms) of the individual events:

$$\Delta T \propto \frac{\Delta W_{\mathrm{ELM}}}{A_{\mathrm{ELM}}} \frac{1}{\sqrt{\tau_{\mathrm{ELM}}}} \tag{2.30}$$

with A_{ELM} ELM wetted divertor area and τ_{ELM} ELM energy deposition time. τ_{ELM} is not varying largely when extrapolating to e.g. ITER since it is thought to be due to the ion transport time [Eich et al., 2003a]:

$$\tau_{\mathrm{ELM}} \propto \frac{L_{\mathrm{OMP}}}{c_{\mathrm{s}}} \propto \frac{R}{\sqrt{T_{\mathrm{e}}}} \tag{2.31}$$

with L_{OMP} field line length and c_{s} ion sound speed with T_{e} electron temperature at the pedestal. For material testing for ITER τ_{ELM} is taken to be 500 µs (FWHM) [Klimov et al., 2009]. The material limit is typically expressed as an *energy fluence* limit (with unit $\mathrm{J/m^2}$) with $\sqrt{\tau_{\mathrm{ELM}}} \approx$ const.. Recent works report on a material limit of $0.15 - 0.5\ \frac{\mathrm{MJ}}{\mathrm{m^2}}$ [Klimov et al., 2009, Loewenhoff et al., 2015, Gunn et al., 2016]. In order to infer the energy fluence from ELM energy ΔW_{ELM} the area on which this energy is deposited on has to be known. A recent scaling from ASDEX Upgrade, JET and MAST for the energy fluence measured at the divertor target has been reported [Eich et al., 2017]:

$$\epsilon_{||} \left[\frac{\mathrm{MJ}}{\mathrm{m^2}}\right] = 0.28 \cdot n_{\mathrm{e,ped}}[10^{20}\mathrm{m}^{-3}]^{0.75} \cdot T_{\mathrm{e,ped}}[\mathrm{keV}]^{0.98} \cdot \Delta W_{\mathrm{ELM}}[\%]^{0.52} \cdot R[\mathrm{m}]^{1.0} \tag{2.32}$$

with $\epsilon_{||}$ being parallel energy fluence[6], $n_{\mathrm{e,ped}}$ and $T_{\mathrm{e,ped}}$ pedestal top density and temperature, respectively and R major radius. Energy balance considerations lead to a model

[4] ELMs are a quasi-periodic phenomenon, thus, no strict frequency exists. In the tokamak community the repetition rate of ELMs is named ELM frequency.

[5] This relation holds as long as the heating power is sufficiently high compared to the power needed to sustain the H-Mode.

[6] The material limit is a perpendicular energy to the surface, due to different geometries of the targets this multi machine regression uses the energy fluence parallel to field lines.

[Eich et al., 2017]:

$$\epsilon_{||}\left[\frac{\mathrm{MJ}}{\mathrm{m}^2}\right] = 6\cdot 10^{-6}\cdot\pi\cdot a[\mathrm{m}]\cdot\hat{\kappa}\cdot p_{\mathrm{e,ped}}[\mathrm{Pa}]\cdot\frac{B_{\mathrm{tor}}^{\mathrm{OMP}}[\mathrm{T}]}{B_{\mathrm{pol}}^{\mathrm{OMP}}[\mathrm{T}]} \tag{2.33}$$

with a minor radius, $\hat{\kappa}$ effective elongation (See appendix D), $p_{\mathrm{e,ped}}$ pedestal top electron pressure and $B_{\mathrm{tor}}^{\mathrm{OMP}}$, $B_{\mathrm{pol}}^{\mathrm{OMP}}$ toroidal and poloidal magnetic field at the outer mid-plane, respectively.

2.2 External Magnetic Perturbation

Applying a non-axisymmetric external magnetic perturbation (MP) is one technique that is studied in order to mitigate or suppress large ELMs (see section 2.1.2) [Lang et al., 2013, Loarte et al., 2014]. Many of today's tokamak experiments are equipped with magnetic coils to study the physics and feasibility of ELM mitigation/suppression with an external magnetic perturbation, e.g. ASDEX Upgrade [Suttrop et al., 2009a], DIII-D [Evans et al., 2004], EAST [Sun et al., 2016], JET [Liang et al., 2007], KSTAR [Jeon et al., 2012], MAST [Kirk et al., 2015] and NSTX [Ahn et al., 2010].
In this thesis the effect of an external magnetic perturbation on power exhaust is investigated in ASDEX Upgrade. The ASDEX Upgrade magnetic perturbation coils are shown in figure 2.2. ASDEX Upgrade is equipped with two rows of eight coils each, one row above

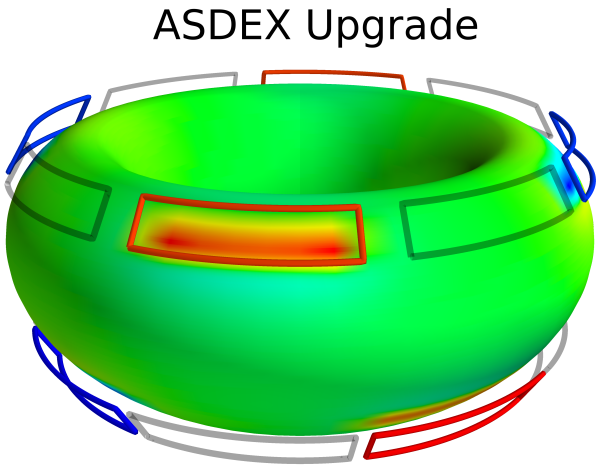

Figure 2.2: ASDEX Upgrade magnetic perturbation coils. Shown is an $n=2$ perturbation with a *differential phase* $\Delta\phi = -\frac{\pi}{2}$ between upper and lower row for #32217 (adapted from [Willensdorfer et al., 2016]).

(upper) and one below (lower) the outer mid-plane. The color indicates different current direction inside the coils, inducing a radial magnetic field. The power supply has recently

been upgraded to allow individual supply of each coil [Teschke et al., 2015, Teschke et al., 2017]. This allows configurations with toroidal mode number $n = 1,2,3,4$ and a selectable *differential phase* $\Delta\phi$ between the two rows:

$$\Delta\phi = \phi_{\text{up}} - \phi_{low} \tag{2.34}$$

with ϕ being phase of the cosine wave function described by the eight coils:

$$I = I_{\text{coil}} \cos\left(\frac{2\pi t}{f_{\text{MP}}} + \phi_{\text{coil}} \cdot n \pm \frac{1}{2}\Delta\phi + \phi_0\right) \tag{2.35}$$

with I_{coil} being restricted by force limits to be at maximum 1.3 kA[7]. Each coil consists of five turns to increase the effective current that induces the magnetic perturbation field to $1.3 \cdot 5 = 6.5\,\text{kAt}$[8].
Figure 2.3 sketches two configurations that are in the following termed *resonant* (a) and *non-resonant* (b), respectively. Shown are field lines at the plasma edge and a magnetic

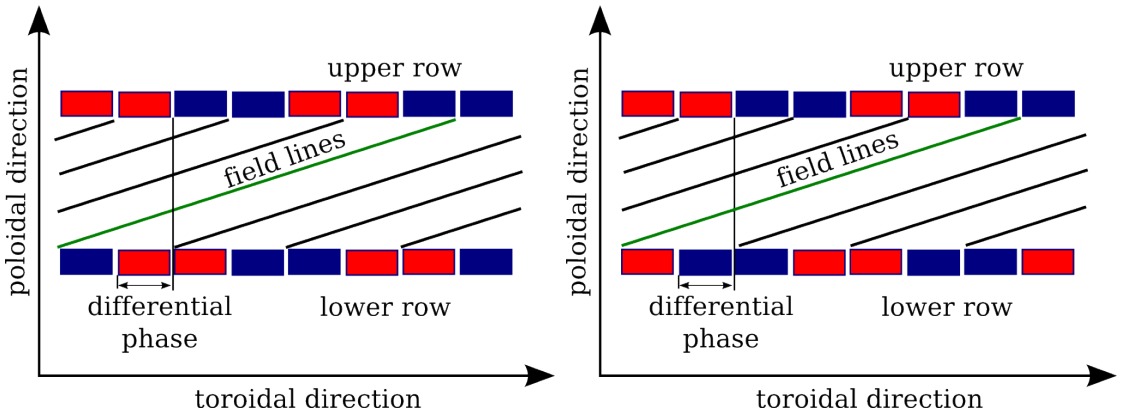

(a) *resonant* (b) *non-resonant*

Figure 2.3: Sketch of two configurations of the external magnetic perturbation field.

perturbation with $n = 2$. When field lines pass by the same phase of the upper and lower row of coils, a configuration is termed *resonant*. In contrast, if a field line connects phases opposite for the upper and lower rows the configuration is termed *non-resonant* [Suttrop et al., 2011].
The *differential phase* of figure 2.3(a) is the same as in figure 2.2 with $\Delta\phi = -\frac{\pi}{2}$. Note here, that the phase is defined as in equation (2.35) and thus dependent on the toroidal mode number. The power supply allows rigid rotations of the magnetic perturbation field. A rigid rotation is used to probe plasma quantities for all toroidal phases at a toroidally fixed measurement position with stationary global conditions and a toroidally

[7]The limit is reduced to 1 kA when operating at higher toroidal field.
[8]This current induces a radial magnetic field of the order of $B_{\text{R}} \sim 10^{-3} B_{\text{tor}}$ at the plasma surface close to the coils.

symmetric equilibrium without magnetic perturbation. Due to the definition (equation (2.35)), the rotation frequency f_{MP} is provided in terms of coil current and not rotation of the perturbation field. The perturbation field rotates $2\pi/n$ in toroidal direction in time $1/f_{\mathrm{MP}}$.
As an example, for a rotation frequency $f_{\mathrm{MP}} = 1\,\mathrm{Hz}$ and a toroidal mode number $n = 2$, the magnetic perturbation field rotates 1π in toroidal direction in 1 s, containing full toroidal information due to the $n = 2$ symmetry.
Most of previous studies on the impact of an external magnetic perturbation focus on changes of global plasma parameters, e.g. density ('density pump-out'), or the increase in ELM frequency [Kirk et al., 2015, Thornton et al., 2015, Sun et al., 2016].
Applying an external magnetic perturbation breaks the axisymmetry of a tokamak and leads to a 2D heat flux pattern on the divertor target [Müller et al., 2013, Jakubowski et al., 2009, Harting et al., 2012, Ahn et al., 2010, Thornton et al., 2014]. It is reported that for ITER it might be necessary to rotate the magnetic perturbation in order to prevent local over-heating due to the toroidally asymmetric heat load [Loarte et al., 2014].

2.2.1 Reported Changes of L-Mode and Inter-ELM Power Load

The change of the heat flux profile at the divertor target with the application of an external magnetic perturbation is shown in figure 2.4. The profile without magnetic perturbation

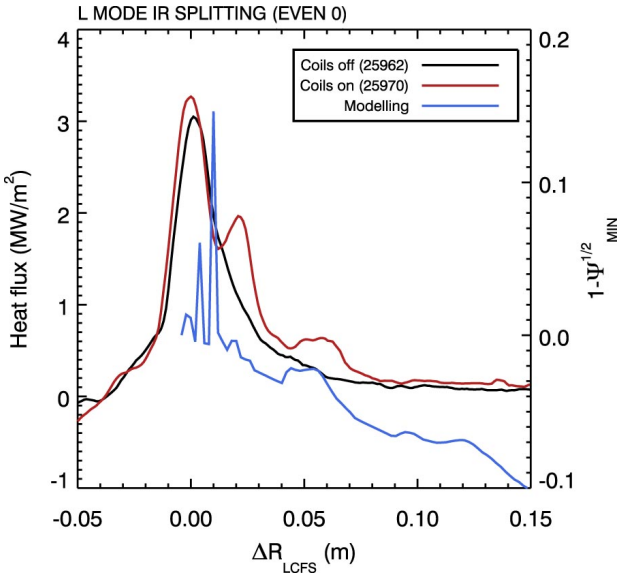

Figure 2.4: Divertor target heat flux profile without (black) and with (red) external magnetic perturbation. Figure taken from [Thornton et al., 2014].

is described by the 1D diffusive model (equation (2.17) on page 13). The profile with magnetic perturbation, however, is not described by this model. The modelling in the figure refers to vacuum field line tracing [Thornton et al., 2014]. Due to the non-axisymmetry

introduced by the magnetic perturbation field a 1D description is not sufficient. The characteristic with multiple distinguishable peaks/local maxima is referred to as lobe structure, e.g. [Kirk et al., 2015, Ahn et al., 2010], or strike line splitting, e.g. [Jakubowski et al., 2009, Harting et al., 2012] as a consequence of the non-axisymmetry. This lobe structure leads to locally increased heat flux compared to the axisymmetric heat flux profile without magnetic perturbation.
In order to characterize the divertor heat flux profile in presence of a magnetic perturbation additional information is needed. In this thesis the profile is divided into toroidally averaged heat flux $\langle q(s)\rangle_\phi$ and toroidal variation $q'(s,\phi)$:

$$\langle q(s)\rangle_\phi = \frac{n}{2\pi}\int_0^{2\pi/n} q(s,\phi)d\phi \tag{2.36}$$

$$q'(s,\phi) = \frac{q(s,\phi)}{\langle q(s)\rangle_\phi} \tag{2.37}$$

$$\Gamma(s) = \max_\phi\left(q'(s,\phi)\right) \tag{2.38}$$

$$\sigma = \Gamma(s=\lambda_\mathrm{q}) \tag{2.39}$$

with $\Gamma(s)$ being named *toroidal maximum* and σ being named *toroidal peaking*. This allows to characterize the profile with only one additional parameter compared to the axisymmetric profile if $\langle q(s)\rangle_\phi$ with magnetic perturbation is described by the 1D diffusive model (equation (2.17)).
For an axisymmetric heat flux profile at the divertor target, $q'(s,\phi), \Gamma(s)$ and σ are unity.

2.2.2 Reported Changes of ELM Induced Power Load

The main focus of studies using an external magnetic perturbation is the effect on ELMs. A commonly used measure of success in ELM mitigation is the increase of ELM frequency. This is motivated by using equation (2.29) (shown on page 16) and assuming a constant wetted area. An increase of ELM frequency in presence of an external magnetic perturbation at ASDEX Upgrade has been reported in e.g. [Suttrop et al., 2011, Kirk et al., 2015, Suttrop et al., 2017].
However, a recent study using measurements of the ELM energy fluence in ASDEX Upgrade reported that type-I ELMs in presence of an external magnetic perturbation are described by the same scaling as ELMs without magnetic perturbation [Sieglin et al., 2017]. The measured ELM energy fluence depending on the model prediction (equation (2.33) on page 17) is shown in figure 2.5. ELMs are non-axisymmetric even without external magnetic perturbation. However, it was shown that the phase of this quasi-mode structure is stochastic leading to smooth averaged profiles [Eich et al., 2005]. The filaments in presence of external magnetic perturbation may *lock* to the external magnetic perturbation field [Jakubowski et al., 2009]. This can lead to localized erosion of the divertor target material.

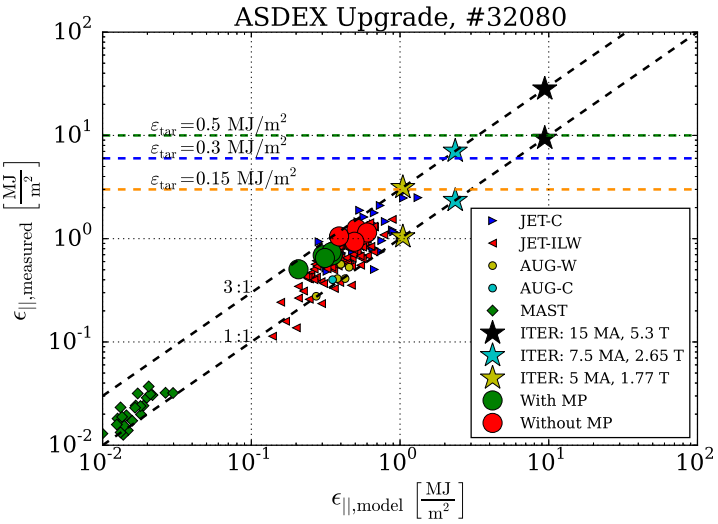

Figure 2.5: Model prediction (equation (2.33)) versus measured ELM peak energy fluence. Database from [Eich et al., 2017], figure adapted from [Sieglin et al., 2017].

Applying an external magnetic perturbation to an ELMy H-Mode can also lead to full ELM suppression [Evans et al., 2004]. ELM suppression was recently established at ASDEX Upgrade [Suttrop et al., 2017].

2.3 Tokamak Experiments

The experiments conducted for this thesis were carried out at two (medium sized) tokamaks, ASDEX Upgrade with a major radius of $R_{\mathrm{AUG}} = 1.65\,\mathrm{m}$ and TCV with a major radius of $R_{\mathrm{TCV}} = 0.89\,\mathrm{m}$. The main features of these machines, relevant for this thesis, are discussed in this section.

2.3.1 ASDEX Upgrade

The tokamak ASDEX Upgrade (**A**xially **S**ymmetric **D**ivertor **EX**periment) is in operation since 1991 at the Max Planck Institute for Plasma Physics in Garching and is currently the largest tokamak fusion experiment in Germany.
The main technical parameters of ASDEX Upgrade are shown in table 2.1 [Streibl et al., 2003]. ASDEX Upgrade has a reactor like geometry similar to future fusion devices (e.g. ITER). Additionally, the installed heating power compared to the machine size is in the range of future machines making ASDEX Upgrade a leading device for heat exhaust studies.
ASDEX Upgrade was the first tokamak to demonstrate operation with all tungsten plasma facing components [Neu et al., 2007]. An inner wall with tungsten plasma facing components is foreseen for future power plants to minimize tritium retention [Roth et al.,

Table 2.1: Technical parameters of ASDEX Upgrade.

major radius	1.65	[m]
minor radius	0.5	[m]
plasma volume	14	[m^3]
installed heating power	30	[MW]
max toroidal B-field	3.9	[T]
max plasma current	1.6	[MA]
max pulse duration	10	[s]

2009, Brezinsek et al., 2013].
A poloidal cross-section of ASDEX Upgrade is shown in figure 2.6(a) for a typical plasma shape and lower single null discharge used in this thesis. Shown is the separatrix (blue), separating the confined region (red) and the scrape-off layer (green). The null point in poloidal flux (X-point) is marked, separating the confined region and the divertor region that contains both scrape-off layer as well as the private flux region (yellow) where flux surfaces are not neighbouring the confined plasma. Due to the relevance for this thesis the *passive stabilizing loop* (PSL) with the magnetic perturbation coils mounted on (red lines) is indicated with the arrows on the right hand side.

2.3.2 Tokamak à Configuration Variable

The ***T**okamak à **C**onfiguration **V**ariable* (TCV) [Hofmann et al., 1994, Coda et al., 2017] started operation in 1992 at the Swiss Plasma Center in Lausanne, Switzerland. The main technical parameters of TCV are shown in table 2.2. It is a tokamak designed to examine

Table 2.2: Technical parameters of TCV.

major radius	0.89	[m]
minor radius	0.25	[m]
plasma chamber	8	[m^3]
installed heating power	5.5	[MW]
max toroidal B-field	1.54	[T]
max plasma current	1.2	[MA]
max pulse duration	4	[s]

a variety of plasma shapes. This is possible due to 16 independently powered poloidal field coils and an open vessel geometry, see figure 2.6(b). TCV is well suited to investigate effects of shaping the confined region, e.g. plasma triangularity δ, as done in this thesis, and further novel alternative divertor configurations. TCV is equipped with carbon plasma

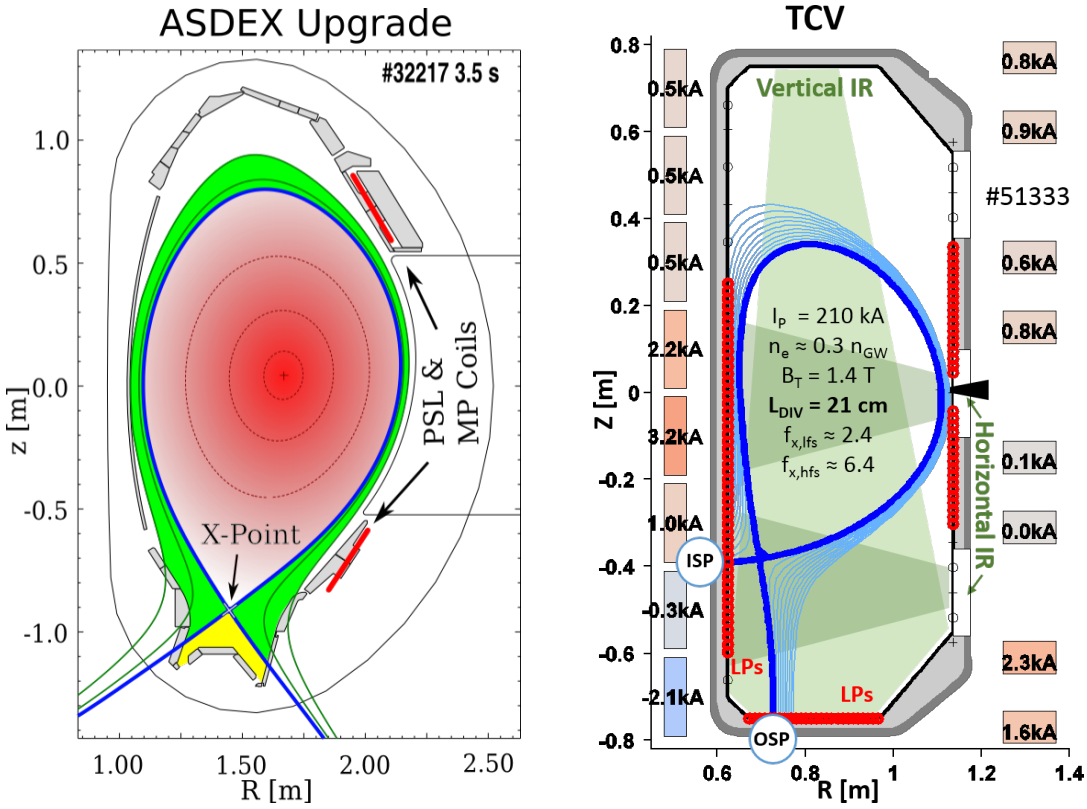

(a) ASDEX Upgrade. The red area the confined plasma region, blue area the scrape-off layer, yellow area the private flux region. Additionally the X-point is marked as well as the PSL (passive stabilizing loop) where the magnetic perturbation coils are mounted on (red lines).

(b) TCV. The 16 independently powered poloidal field coils are shown on the left and right hand side of the vessel. Figure adapted from [Maurizio et al., 2017].

Figure 2.6: Poloidal cross-section of both ASDEX Upgrade and TCV. The blue lines represent the separatrix.

facing components.

Chapter 3

Experimental Methods

3.1 Infrared Thermography

The essential diagnostics for this thesis is infrared (IR) thermography. IR thermography is used to measure surface temperature of objects without being in direct contact. The method used on ASDEX Upgrade and TCV is based on the spectral composition of electro-magnetic waves being emitted from the surface for a given temperature. For an idealized black body, an object absorbing electro-magnetic radiation at all wavelengths, the spectral radiance M is described by Planck's law [Planck, 1900a, Planck, 1900b].

$$M_{\lambda}^{\mathrm{bb}}(\lambda, T)\mathrm{d}A\mathrm{d}\lambda = \frac{2\pi hc^2}{\lambda^5}\frac{1}{e^{\frac{hc}{\lambda k_{\mathrm{b}} T}} - 1}\mathrm{d}A\mathrm{d}\lambda \qquad \left[\mathrm{Wm}^{-3}\right] \tag{3.1}$$

It describes power emitted from area $\mathrm{d}A$ in the wavelength interval $\mathrm{d}\lambda$ per unit solid angle for a black body (bb) at absolute temperature T. The constants are Boltzmann constant k_{B}, Planck constant h and speed of light c. The divertor material that is observed in the experiment is not a black body. A correction term has to be introduced, called the emissivity ϵ. This characterizes the ability of the material to absorb and emit photons at a specific wavelength compared to a black body. In general this is dependent on temperature and wavelength.

$$\epsilon = \epsilon\left(\lambda, T\right) \tag{3.2}$$

The emissivity is between $0 \leq \epsilon \leq 1$, with $\epsilon = 1$ being a perfect black body. The ASDEX Upgrade divertor target consists of tungsten tiles, the TCV divertor target of carbon tiles. The IR systems that are used at the experiments count photons. Thus, it is useful to rewrite Planck's law for the photon flux Γ using equation (3.1), emissivity ϵ and photon energy $E_{\gamma} = \frac{hc}{\lambda}$.

$$\Gamma\left(\lambda, T\right)\mathrm{d}A\mathrm{d}\lambda = \epsilon\left(\lambda, T\right)\frac{2\pi c}{\lambda^4}\frac{1}{\exp\left(\frac{hc}{\lambda k_{\mathrm{B}} T}\right) - 1}\mathrm{d}A\mathrm{d}\lambda \left[\mathrm{s}^{-1}\mathrm{m}^{-3}\right] \tag{3.3}$$

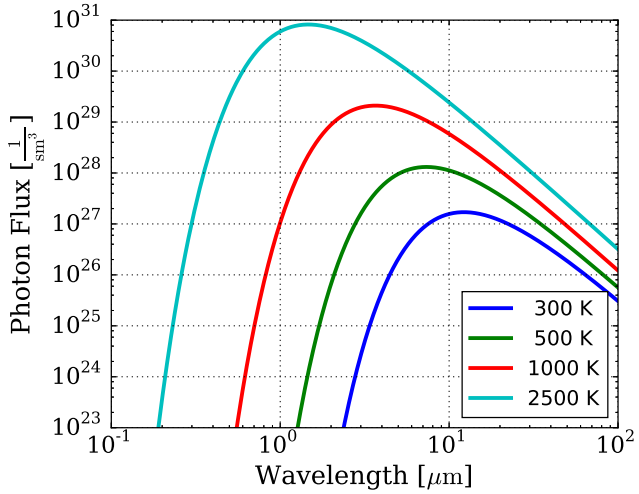

Figure 3.1: Photon flux of a black body (equation (3.3)) depending on wavelength at different temperatures.

The photon flux emitted from a black body depending on the wavelength for different temperature is shown in figure 3.1. The expected range of divertor tile temperature is between room temperature and 2500 K for ASDEX Upgrade [Herrmann et al., 2011]. The dynamic range of the ASDEX Upgrade IR system is about 8 orders of magnitude[1]. At wavelengths in the visible to near infrared spectrum below 1 µm it is not possible to detect temperatures in the range of room temperature, the surface temperature at the beginning of the discharge. At wavelengths in the far infrared spectrum above 10 µm the dynamic range is not utilized, with the photon flux not significantly changing with temperature. This decreases the signal to noise ratio in the measured temperature. An additional aspect is that sapphire vacuum windows can be used if the wavelength is below 5 µm.
The photon flux depending on temperature for different wavelengths in the infrared range is shown in figure 3.2. At short wavelength (1 µm) the photon flux is low at low temperature. However, photon flux strongly increases at high temperature making this wavelength ideal for measurements for machine protection. For systems that are supposed to detect areas that are overheating it is useful to have a comparator like behaviour. The protection system of ASDEX Upgrade uses cameras in this wavelength range, e.g. the video real time control [Herrmann et al., 2011].
At long wavelength (10 µm) the increase of photon flux at low temperature is larger compared to a mid wavelength system (5 µm). This trend reverses at higher temperature with the mid wavelength exhibiting a stronger increase of photon flux with temperature increase. For the typical range of temperature during ASDEX Upgrade discharges a system at about 5 µm is best suited. The settings of the IR camera systems used in this thesis at ASDEX

[1]The ASDEX Upgrade system has a 15 bit ADC and the integration time can be varied between 4 to 4000 µs.

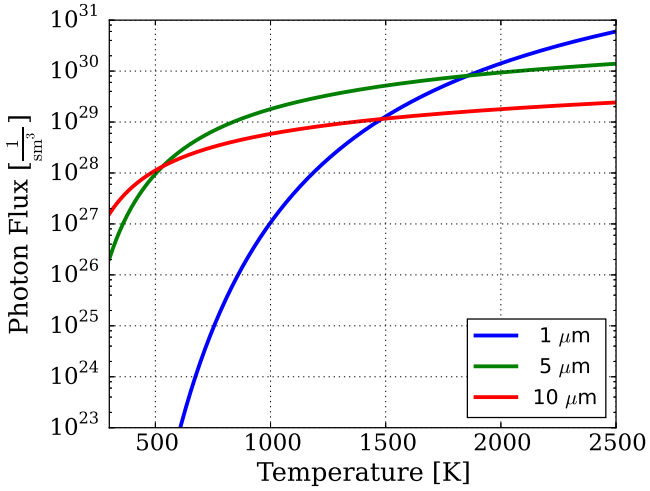

Figure 3.2: Photon flux of a black body (equation (3.3)) depending on temperature at different wavelengths.

Upgrade and TCV are discussed in section 3.1.2.

3.1.1 Heat Flux Evaluation Code THEODOR

Measurements with an IR system provide the temperature evolution of the surface that is observed. In order to reconstruct the heat flux that is causing this temperature evolution the heat diffusion equation is solved:

$$\rho c_\mathrm{p} \frac{\partial T}{\partial t} = \nabla \kappa \nabla T \tag{3.4}$$

with c_p specific heat capacity, T temperature distribution, t time and κ heat conductivity. In experiments, typically a toroidally symmetric heat load is assumed for the evaluation. In principle, in this thesis toroidally asymmetric heat loads due to an external magnetic perturbation are investigated. However, the assumption of uniform heat load in toroidal direction within the evaluation domain is still valid due to the comparable large toroidal extent compared to the variation along the target location. Thus, a 1D profile along the divertor target location, perpendicular to the toroidal direction, is sufficient to characterize the total heat load. The heat flux is evaluated with a code called THEODOR (**TH**ermal **E**nergy **O**nto **D**ivert**OR**), pioneered by Herrmann and Günther [Herrmann et al., 1995] and further refined by Sieglin [Sieglin, 2014, Sieglin et al., 2015]. The input data for the code is the temperature evolution $T(s,t)$ along the divertor target location s in time t. The output data is heat flux density $q(s,t)$ perpendicular to the surface.
In order to solve the non-linear differential heat diffusion equation (equation (3.4)), a

substitution is performed using the heat potential u for temperature T:

$$u(T) = \int_0^T \kappa\left(T'\right) \mathrm{d}T' \tag{3.5}$$

leading to:

$$\frac{\partial u}{\partial t} = \frac{\kappa}{\rho c_\mathrm{p}} \Delta u \tag{3.6}$$

which is a linear differential equation. This equation is solved numerically for 2D coordinates, one dimension along the target location and one into the depth of the tile [Sieglin et al., 2015, Nille et al., 2017]. From the temperature distribution inside the tile heat flux q onto the surface is evaluated:

$$q = \kappa(T) \nabla T|_\mathrm{surf} = \nabla u|_\mathrm{surf} \tag{3.7}$$

with the gradient being calculated into the tile, perpendicular to the surface.

3.1.2 Systems at ASDEX Upgrade and TCV

The technical features of the IR systems at ASDEX Upgrade and TCV are presented in this section. The system description for ASDEX Upgrade is found in [Sieglin et al., 2015] and for TCV in [Maurizio et al., 2017]. The settings used in this thesis at ASDEX Upgrade are shown in table 3.1. A poloidal cross-section and the IR view onto the outer divertor

Table 3.1: ASDEX Upgrade IR system.

		L-Mode	H-Mode
frame rate	[Hz]	800	2100
spectral range	[µm]	4.7 ± 0.15	
spacial resolution	$[\frac{\mathrm{mm}}{\mathrm{px}}]$	0.6	
ADC resolution	[bit]	15	14

target of ASDEX Upgrade is shown in figure 3.3. The chequerboard structure on the tile containing the position that is used for the evaluation (marked with a red line) is used for a movement correction of the measured frames that is needed due to vibrations in the optical path. The ASDEX Upgrade IR system is observing a toroidal location at an angle of $\phi_{IR} = 213°$ in the ASDEX Upgrade coordinate system. The toroidal angle is defined for convenience as it will be used for the data interpretation in chapter 4.
The settings used in this thesis at TCV are shown in table 3.2. A poloidal cross-section of TCV is shown in figure 3.4 showing the viewing geometry for the two systems together

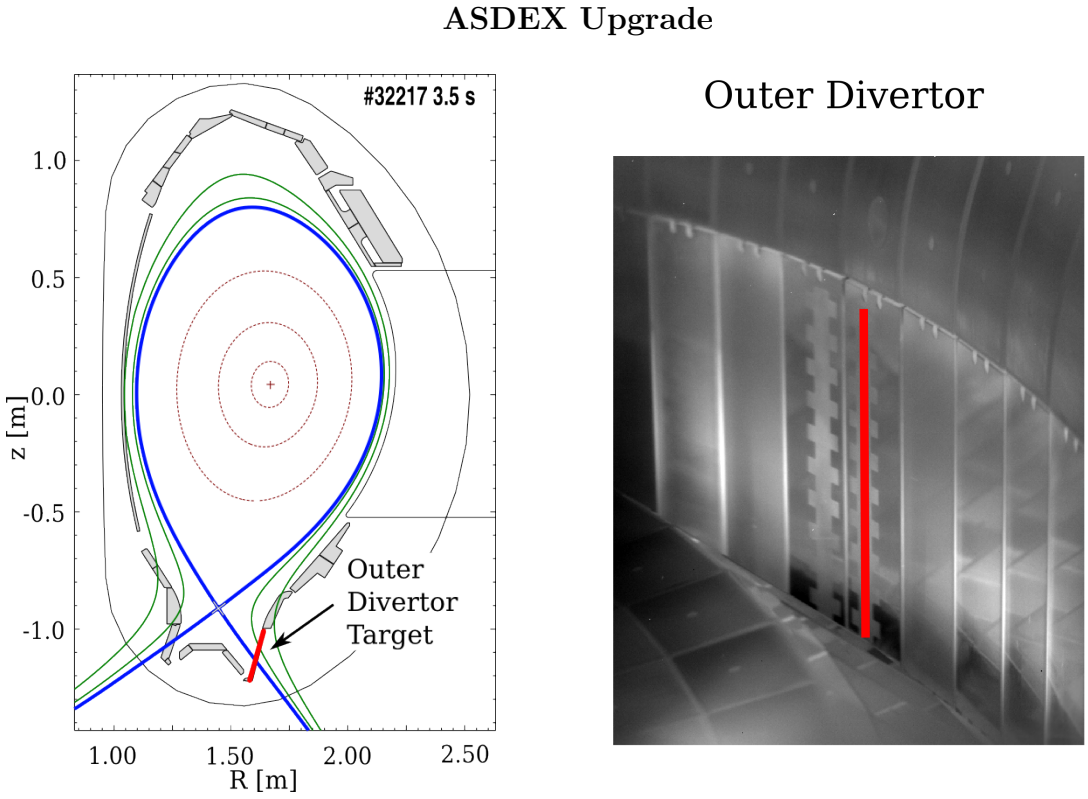

Figure 3.3: Poloidal cross-section of ASDEX Upgrade together with the IR full frame view onto the outer divertor target. The red line indicates where the 1D profile for the heat flux calculation is extracted. Figure adapted from [Sieglin et al., 2016b].

with a 2D image of both targets and an exemplary line for the data evaluation. The horizontal camera observes the inner column of the vessel, on which the inner strike line intersects for a typical plasma geometry as investigated in this thesis. The vertical camera observes the floor of the vessel, on which the outer strike line intersects the vessel.
The systems at ASDEX Upgrade and TCV can be operated in a sub windowed mode. This allows to increase the frame rate.

Table 3.2: TCV IR system with L-Mode settings.

		outer	inner
frame rate	[Hz]	400	200
spectral range	[µm]	4.5 - 5.1	3.7 - 4.8
spacial resolution	$[\frac{\text{mm}}{\text{px}}]$	2.5	1.6 (0.8)
ADC resolution	[bit]	14	14

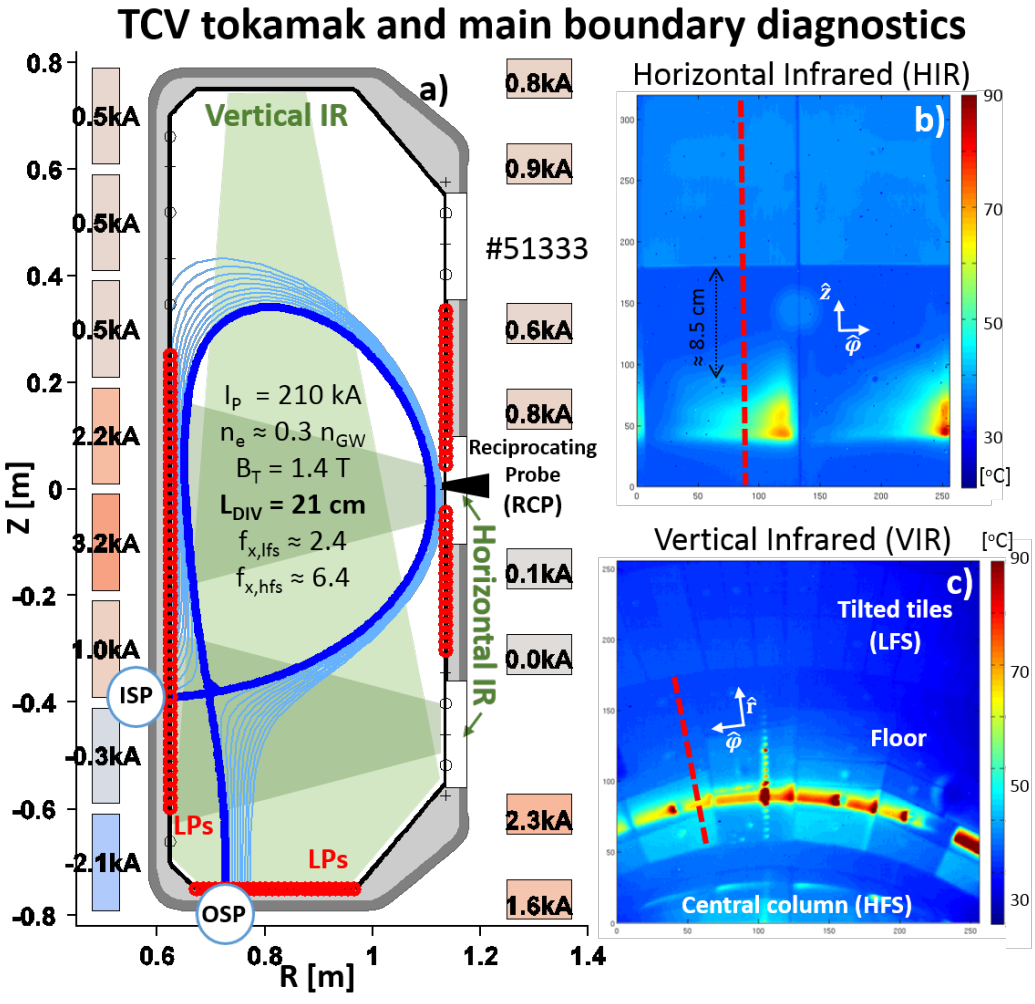

Figure 3.4: Poloidal cross-section of TCV together with the IR full frame view onto both divertor targets. The red lines indicate where the 1D profiles for the heat flux calculation are extracted. Figure adapted from [Maurizio et al., 2017].

3.2 Simplified Heat Flux Model Using Field Line Tracing and the Two Point Model

To interpret experimental results an ad hoc model was developed within this thesis and published in [Faitsch et al., 2017c]. With this model the influence of the magnetic perturbation configuration and transport in the divertor volume on the divertor heat flux pattern is studied.
The intention of this model is to predict the heat flux pattern in order to (a) gain insight on the generic heat transport properties and (b) compare to measured heat flux profiles. This allows to aim for as few as possible (free) input parameters as well as the possibility to change single parameters and study the direct influence they have on the heat flux distribution. The model is not solving transport equations (parallel versus perpendicular heat transport) as e.g. EMC3-Eirene [Feng et al., 1997], but uses scrape-off layer fall-off lengths as input.
Due to the semi-empirical approach used in this model one has to be cautious in extrapolating the results to other machines, especially to larger devices like ITER, as the input parameters such as the fall-off length may vary from current extrapolations.

3.2.1 Magnetic Field Configuration

The model uses the vacuum field approximation and a field line tracer. This method was pioneered in Tore Supra and Textor [Nguyen et al., 1997, Finken et al., 1998] and found good agreement between model prediction and heat flux data [Schmitz et al., 2008]. Similar approaches are discussed in [Strumberger, 1996, Eich et al., 2000, Cahyna et al., 2014]. The utilized field line tracer is a 5th order Runge-Kutta code, named GOURDON [Gourdon et al., 1971, Strumberger, 1996, Strumberger, 2000]. To start with, the axisymmetric poloidal flux matrix Ψ_p is calculated with CLISTE [McCarthy et al., 1999, Schneider et al., 2000]. The currents inside the magnetic perturbation coils and the currents in the conductive passive stabilizing loop (PSL) are then taken into account. The PSL acts as a low pass filter for plasma oscillations in order to improve the control of the plasma discharge [Gruber et al., 1993]. At a rotation frequency at 1 Hz the magnetic perturbation due to the magnetic perturbation coil currents is reduced by 25% according to FEM calculations [Suttrop et al., 2009b]. The field line tracer calculates the magnetic field induced by the magnetic perturbation coils, $\boldsymbol{B}^{\mathbf{MP}}$, by solving Biot-Savart's law and superimposing to the axisymmetric magnetic field:

$$\boldsymbol{B}_{\mathbf{tot}} = \boldsymbol{B}_{\mathbf{tor}} + \boldsymbol{B}^{\mathbf{axi}}_{\mathbf{pol}} + \boldsymbol{B}^{\mathbf{MP}} \tag{3.8}$$

with the toroidal field component being only dependent on major radius R:

$$\boldsymbol{B}_{\mathbf{tor}} = B^{\mathrm{axis}}_{\mathrm{tor}} \frac{R_{\mathrm{axis}}}{R} \hat{\boldsymbol{\phi}} \tag{3.9}$$

with $\hat{\boldsymbol{\phi}}$ being the unit vector in toroidal direction. Poloidal magnetic field B_{pol} is calculated from poloidal flux Ψ_p.

$$\boldsymbol{B}_{\mathbf{pol}}^{\mathbf{axi}} = \frac{\nabla \Psi_p}{R} \tag{3.10}$$

Plasma response to the magnetic perturbation field is not considered, similar to the previously mentioned work from Tore Supra and Textor. It was shown, however, that it might play an important role for ELM mitigation/suppression presumably due to changes of the pedestal profiles [Snyder et al., 2011, Moyer et al., 2017]. Plasma response depends on normalized plasma pressure [Piovesan et al., 2017, Igochine et al., 2017]. With low normalized pressure, which all discussed discharges in this thesis have, the vacuum approximation is valid, see e.g. figure 1 of [Piovesan et al., 2017].
Plasma response can either shield or amplify the external magnetic perturbation. Shielding might lead to a reduction, amplification to an increase of the variation in heat flux.
In order to calculate the plasma response two approaches are reported, (a) ad hoc screening currents on resonant flux surfaces [Cahyna et al., 2014, Brida et al., 2017], or (b) plasma profiles such as pressure, current density and toroidal rotation, used for codes like VMEC [Hirshman and Whitson, 1983, Strumberger et al., 2014], MARS-F [Liu et al., 2000, Liu et al., 2016] or JOREK [Huysmans and Czarny, 2007, Orain et al., 2013].
Treating this plasma response is outside of the scope of this thesis. However, the presented model can be linked to the magnetic field calculated by codes like the afore mentioned. The modelled heat flux is compared to measurements, thus, the limitations of using the vacuum field approximation are studied.

3.2.2 Field Line Tracing

Field lines are traced starting at the outer divertor target and either intersect a plasma facing component, e.g. inner divertor, or enter the confined region, here defined by the separatrix of the unperturbed field, where the calculation is terminated at a maximum connection length of 2 km. For illustration of the method, a poloidal projection of field lines starting at the outer divertor target is shown in figure 3.5(a) with field lines in the scrape-off layer and the private flux region.
A typical field line in the scrape-off layer is shown in a 3D plot in figure 3.5(b). The field line tracing starts at the outer divertor target and is terminated at the inner divertor target.

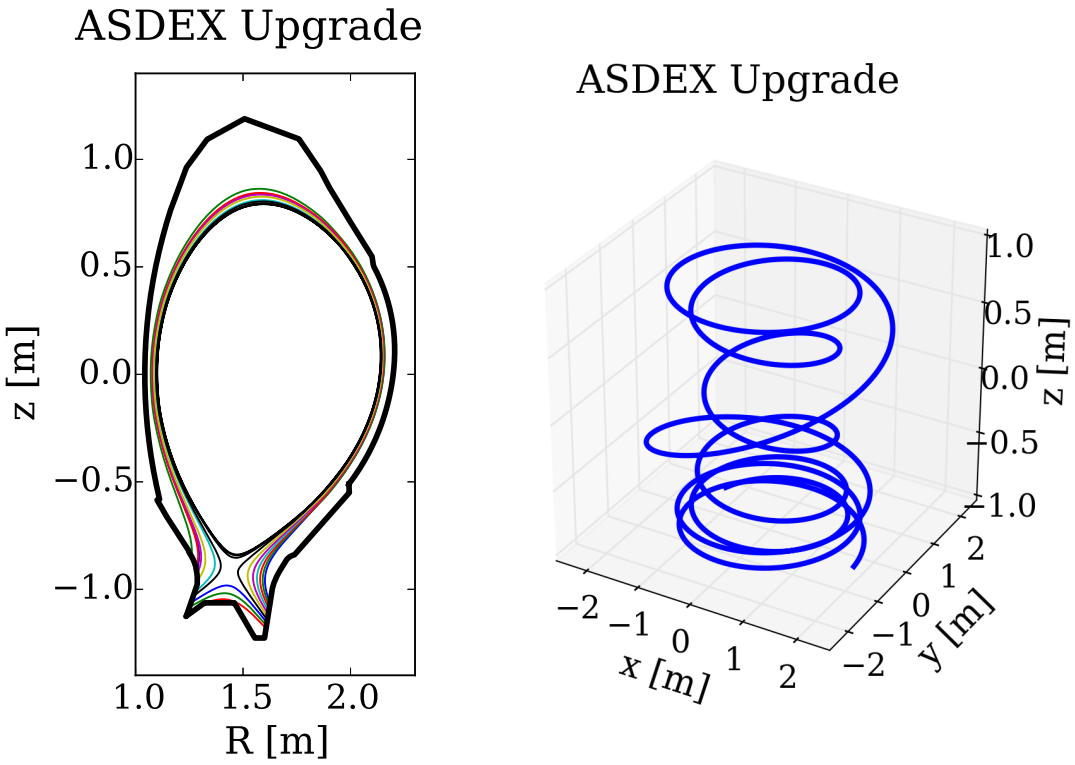

(a) Poloidal projection of field lines in the scrape-off layer and private flux region.

(b) 3D representation of a single field line in the scrape-off layer.

Figure 3.5: Tracing of field lines starting at the outer divertor target and terminated at the inner divertor target.

Input from field line tracing for the presented model are:

- Connection length at the outer mid-plane.
  The radial and toroidal intersection points at the outer mid-plane are marked together with the connection length. A field line may intersect the outer mid-plane multiple times if a magnetic perturbation is present.

- Mapping of 2D target location to 2D outer mid-plane location: $(s,\, \phi_{\mathrm{tgt}}) \rightarrow (R_{\mathrm{OMP}},\, \phi_{\mathrm{OMP}})$.
  The field line tracing is starting at random positions at the outer divertor target and the first intersection point at the outer mid-plane is taken for the mapping.

In the following a comparison between an axisymmetric magnetic field configuration and a superimposed magnetic perturbation is discussed. The magnetic field is taken from the ASDEX Upgrade discharge # 32217 at 3.5 s. The external magnetic perturbation is *resonant* (see section 2.2).

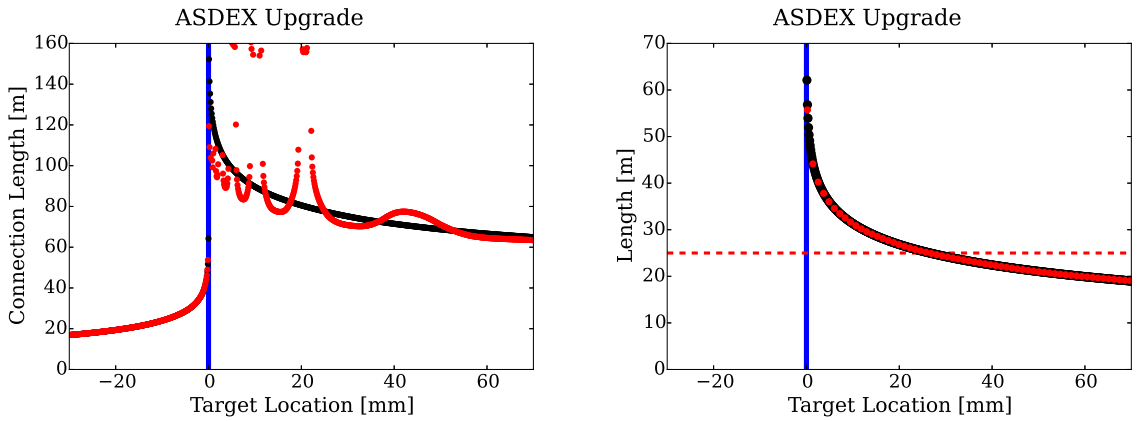

(a) Connection length.

(b) Length to outer mid-plane L_{OMP}.

Figure 3.6: Length of field lines starting at the outer divertor target without (black) and with (red) magnetic perturbation.

The connection length for both magnetic field configurations is shown in figure 3.6(a). The blue line represents the strike line position[2]. It is seen that for an axisymmetric magnetic field the connection length monotonically increases towards the strike line position where the length diverges. With magnetic perturbation additional locations with increased connection length appear in the scrape-off layer.
The field line length L_{OMP} from outer divertor target to the outer mid-plane is shown in figure 3.6(b) for both magnetic field configurations. This length is used in the two point model (see section 2.1.1.1). L_{OMP} increases towards the strike line where it diverges. No connection between the private flux region (negative target location) and the outer mid-plane exists. The additional magnetic perturbation is not changing L_{OMP} significantly. The red dotted line at $L_{\mathrm{OMP}} = 25\,\mathrm{m}$ represents the length that is used for the heat flux calculations in section 3.2.3.
Although L_{OMP} does not change significantly, the radial position where the field lines intersect the outer mid-plane varies when applying an external magnetic perturbation. This is shown in figure 3.7 for an axisymmetric magnetic field (black) and with superimposed magnetic perturbation (red). For an axisymmetric magnetic field the major radius R at the outer mid-plane increases monotonically with the target location. Further, in the case of the present ASDEX Upgrade divertor, this can be approximated by a linear increase close to the strike line position. This implies, that the flux expansion is not varying significantly along the target location, making the approximation with a scalar reasonable. With additional magnetic perturbation the monotonic behaviour breaks due to the superimposed non-axisymmetric radial field component.

[2]For a axisymmetric magnetic field this is well defined with the separatrix, for simplicity the same position is shown for the magnetic field including an external magnetic perturbation.

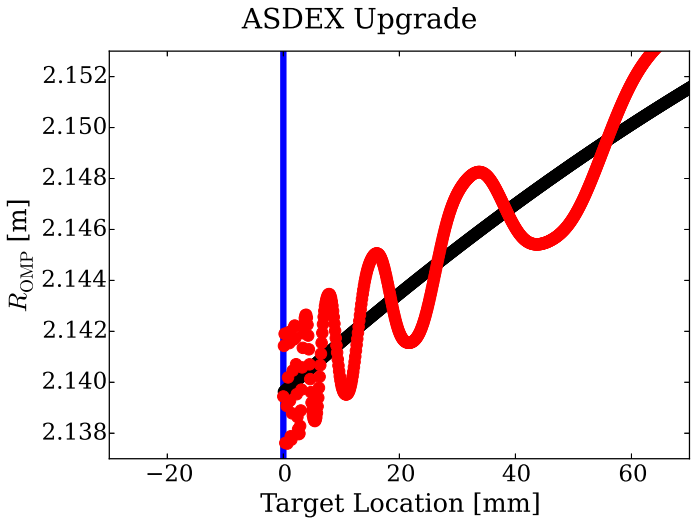

Figure 3.7: Major radius at the outer mid-plane R_{OMP} depending on the target location without (black) and with (red) magnetic perturbation.

So far field lines are compared for two magnetic field configurations, with and without an external magnetic perturbation, but always starting at the same toroidal angle at the target. Due to the helicity of the tokamak magnetic field, a longer L_{OMP} implies a longer path in toroidal direction since the poloidal direction is not changing significantly from the outer target to the outer mid-plane.
Tracing field lines from the outer mid-plane to the outer divertor target, starting at a fixed toroidal angle and increasing major radius, is shown in figure 3.8 for an axisymmetric magnetic field (black dots) and with superimposed magnetic perturbation (red diamonds). The slope of the target location depending on the toroidal angle increases with increasing target location. At the strike line position field lines diverge in length and all toroidal angles at the target are reached at the same target location s.
With an axisymmetric magnetic field no variation in toroidal direction is present, however, with applied magnetic perturbation this symmetry is broken. An often used proxy for the position where heat flux impinges on the divertor target is a 2D figure of the connection length at the divertor target along the target location and the toroidal angle. Such a representation is shown in figure 3.9. Due to the symmetry of the $n=2$ magnetic perturbation, the shown toroidal angle is reduced to $[0,\pi)$. The position at the divertor where the connection length is long is a consequence of the phase of the magnetic perturbation and the target position at which field lines from a fixed toroidal angle at the outer mid-plane intersect, shown in figure 3.8. This position is not significantly changed by the magnetic perturbation. However, the magnetic perturbation leads to field lines being significantly longer compared to the axisymmetric magnetic case at distinguished positions. For a given toroidal angle the connection length is shown in figure 3.6(b).

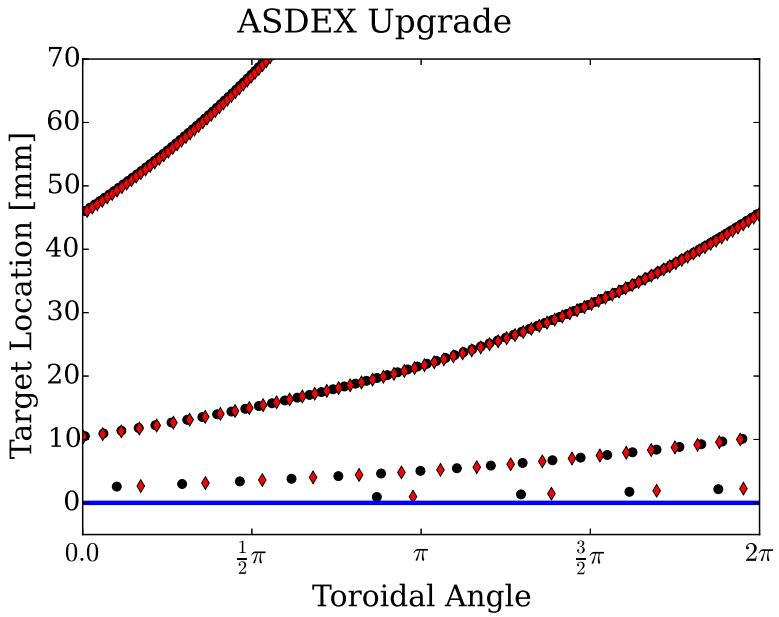

Figure 3.8: Target position of a set of field lines started at the outer mid-plane at fixed toroidal angle with $2.140\,\mathrm{m} < R_{\mathrm{OMP}} < 2.147\,\mathrm{m}$, without (black dots) and with (red diamonds) a magnetic perturbation.

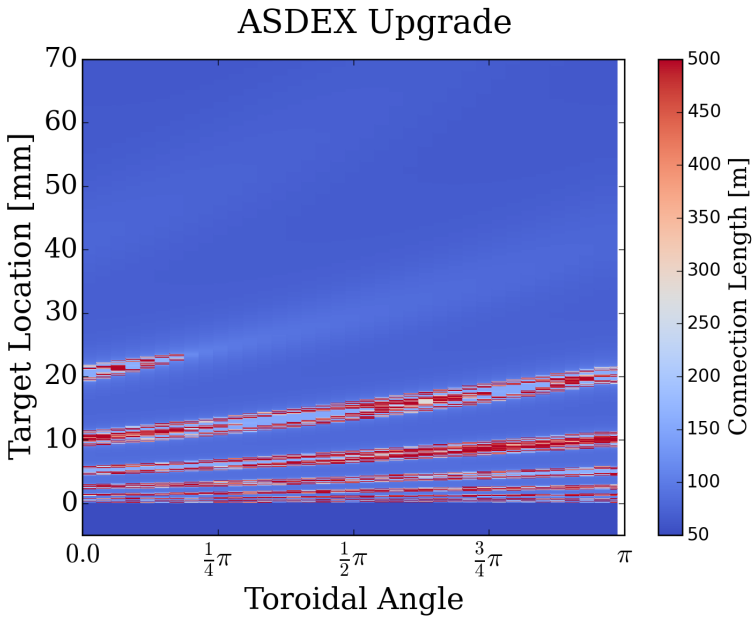

Figure 3.9: Connection length mapped at the outer divertor target along the target location and the toroidal angle for a magnetic field with superimposed $n = 2$ magnetic perturbation.

3.2.3 Approximations and Assumptions

The model used here is constrained to reproduce the 1D diffusive model (section 2.1.1.2 equation (2.17)) in the limit of an axisymmetric configuration. From field line tracing a connection between outer mid-plane and target location is estimated. In order to calculate heat flux, target and outer mid-plane values for T_e, additionally to the geometry (L_OMP), have to be known. Heat flux is calculated using the two point model (section 2.1.1.1).

Electron temperature has an exponential decay in the scrape-off layer.
The electron temperature fall-off length λ_{T_e} is calculated using the two point model (equation (2.8)) and the power-fall-off length λ_q. The fall-off lengths are calculated in real space. Due to the short lengths for typical λ_{T_e}, flux surfaces can be approximated to be equally spaced and electron temperature T_e is treated as a flux quantity $T_\mathrm{e}(\rho_\mathrm{pol})$.

Parallel heat flux $q_{||}$ is constant along field lines.
The perpendicular information is covered with the upstream temperature distribution. In order to be consistent with the 1D diffusive model, cross-field transport in the divertor region is simplified by convolving the target profile, resulting from the two point model, with a Gaussian for each toroidal target position.

Constant L_OMP is used for the calculation.
Small variations of the length of the order of 1.2 (20%) leads to a heat flux variation of $1.2^{\frac{2}{7}} \approx 1.05$ (5%). The L_OMP is shown in figure 3.6(b) with small variations of the length except close to the strike line. In order to have both, an exponential temperature and heat flux decay at the outer mid-plane for an axisymmetric configuration, the field line length between outer mid-plane and outer divertor target is approximated to be constant.

Target electron temperature is neglected ($T_\mathrm{e,tgt} = 0\,\mathrm{eV}$).
Using the same approximation as in the derivation for equation (2.4) in section 2.1.1.1.

Spitzer-Härm electron conductivity with $\kappa_0 = 2000\,\frac{\mathrm{W}}{\mathrm{m}\,\cdot\,(\mathrm{eV})^{\frac{7}{2}}}$ is assumed.
This value is chosen as a typical ASDEX Upgrade scrape-off layer parameter for an effective charge $z_\mathrm{eff} = 2$ [Kallenbach et al., 2001].

Perpendicular heat flux is calculated using local field line angle α.
Heat flux perpendicular to the divertor target surface is calculated using:

$$q_\perp = \sin(\alpha) \cdot q_{||} \tag{3.11}$$

with $\sin(\alpha) \approx \frac{1}{20}$ for ASDEX Upgrade and the present divertor configuration Div III [Herrmann et al., 2013].
A toroidal inclination of the divertor target tiles is needed to prevent leading edges which is not taken into account for the calculation of the angle. A second minor change in the field line angle is the flat tile surface, not following the toroidal direction of the vessel. Both effects together lead to a variation of the heat flux amplitude

in toroidal direction of about 20 % and an additional, but less pronounced, difference in direction of the target location. The angle is calculated with the magnetic perturbation present.

Magnetic perturbation corrugates separatrix.

The perturbed separatrix surface is projected to the outer mid-plane (OMP, z = 0) as a corrugated line and is represented by:

$$R_{\mathrm{sep}}(\phi) = A_0 \cdot \sin(n \cdot \phi + B_0) + A_1 \cdot \sin(2n \cdot \phi + B_1) + R_{\mathrm{sep,axi}}. \tag{3.12}$$

The major radius of the axisymmetric separatrix at the outer mid-plane is used as average value ($\langle R_{\mathrm{sep}}(\phi)\rangle_\phi = R_{\mathrm{sep,axi}}$) and a toroidal ($\phi$) sinusoidal component ($\phi \epsilon [0, 2\pi)$) is introduced. The axisymmetric separatrix major radius is calculated using field line tracing with an axisymmetric magnetic field, the amplitude of the sinusoidal components (A_0 and A_1) is calculated using field line tracing with magnetic perturbation present. The periodicity of the sinusoidal is given by the dominant mode number n of the applied magnetic perturbation. The amplitude of the deformation is fitted using an arbitrary but fixed connection length approaching the separatrix in the unperturbed case. In the presented results this was fixed to a range between 120-125 m (compare to figure figure 3.6). This separatrix is used to define the poloidal flux coordinate $\rho_{\mathrm{pol}}(R, \phi)$ as a 2D quantity at the outer mid-plane for the calculation of the electron temperature.

The input parameters that are needed in order to calculate heat flux profiles with this model are:

- Magnetic field and geometry.
- Field lines: connecting divertor target and outer mid-plane.
- $T_{\mathrm{e,sep}}$: separatrix electron temperature at the outer mid-plane.
- λ_{q}: power fall-off length.
- S: divertor broadening.

Chapter 4

Divertor Power Load in Presence of a Magnetic Perturbation in ASDEX Upgrade

In this chapter experiments at ASDEX Upgrade in presence of a magnetic perturbation are discussed, focusing on outer divertor target heat flux. The application of an external magnetic perturbation is studied as a tool to mitigate or suppress large ELMs which, if unmitigated, might limit the lifetime of the divertor target (see section 2.2). In this chapter experimental and modelled heat flux profiles are presented and compared. The chapter is divided into L- and H-Mode results. The L-Mode studies focus on the characterization of the steady state heat flux in presence of an external magnetic perturbation, partially presented in [Faitsch et al., 2017b, Faitsch et al., 2017c]. Section 4.5 presents both heat flux associated with ELMs as well as inter-ELM, steady state, heat flux in H-Mode. Experimental steady state heat flux profiles are compared to modelling results using the model described in section 3.2.

The main objective is the characterization of changes in the divertor heat flux depending on magnetic perturbation field properties and plasma density in L-Mode. The majority of discharges utilize an external magnetic perturbation with a toroidal mode number $n = 2$. The investigated magnetic perturbation properties are the *differential phase* (section 4.2.1), the amplitude of the magnetic perturbation (section 4.2.2) and the fundamental toroidal mode number (section 4.2.3). Density variations are used to investigate the effect of variations in the scrape-off layer and divertor transport (section 4.3). Both transport qualifiers, λ_q for the scrape-off layer and S for the divertor transport, have been shown to increase with increasing density in ASDEX Upgrade L-Mode (see section 2.1.1.3). A third aspect is the effect of field penetration on divertor heat flux (section 4.4).

4.1 Investigated Plasma Scenario in L-Mode

Global plasma parameters for the reference shot # 32212 are shown in figure 4.2. The same parameters are used for the study of the *differential phase* in section 4.2. In section 4.3 discharges with higher stationary densities are discussed. The density is measured with the core and edge channel of the DCN interferometer at ASDEX Upgrade [Mlynek et al., 2010].
The scenario has a toroidal magnetic field of -2.5 T and a plasma current of 0.8 MA. About 370 kW of external ECRH power [Leuterer et al., 2001] is applied for core heating. This is chosen to maximize the temperature increase at the divertor target, increasing the IR signal quality but keeping the core heating below the H-Mode power threshold.
Plasma shape is fully evolved at around 2.0 s. In the reference discharge a constant magnetic perturbation was applied between 4.5 s and 5.0 s. The application of the magnetic perturbation does not change global plasma parameters significantly here. This allows to study the effect of the magnetic perturbation on the target heat flux pattern with otherwise constant parameters.
The discharges performed with a rigid rotation of the external magnetic perturbation field have a reference phase without magnetic perturbation in the beginning before 2.5 s. This is done to ensure the similarity of discharges as well as providing a comparison with axisymmetric target profiles. The magnetic perturbation field is rotated with a frequency at 1 Hz. This results in about 3 rotations throughout every discharge, ensuring the reproducibility of the measurement.
Heat flux onto the outer divertor target for discharge # 32217 (*resonant* configuration) is shown in figure 4.1. The heat flux profile obtained in the phase without magnetic pertur-

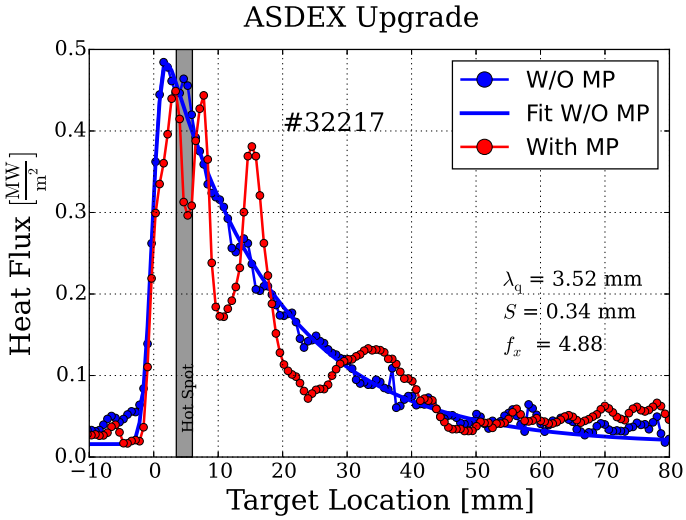

Figure 4.1: 1D heat flux profile for discharge # 32217 with (red) and without (blue) magnetic perturbation. A hot spot is present in the grey area.

bation is shown in blue together with a fit using the 1D diffusive model (section 2.1.1.2).

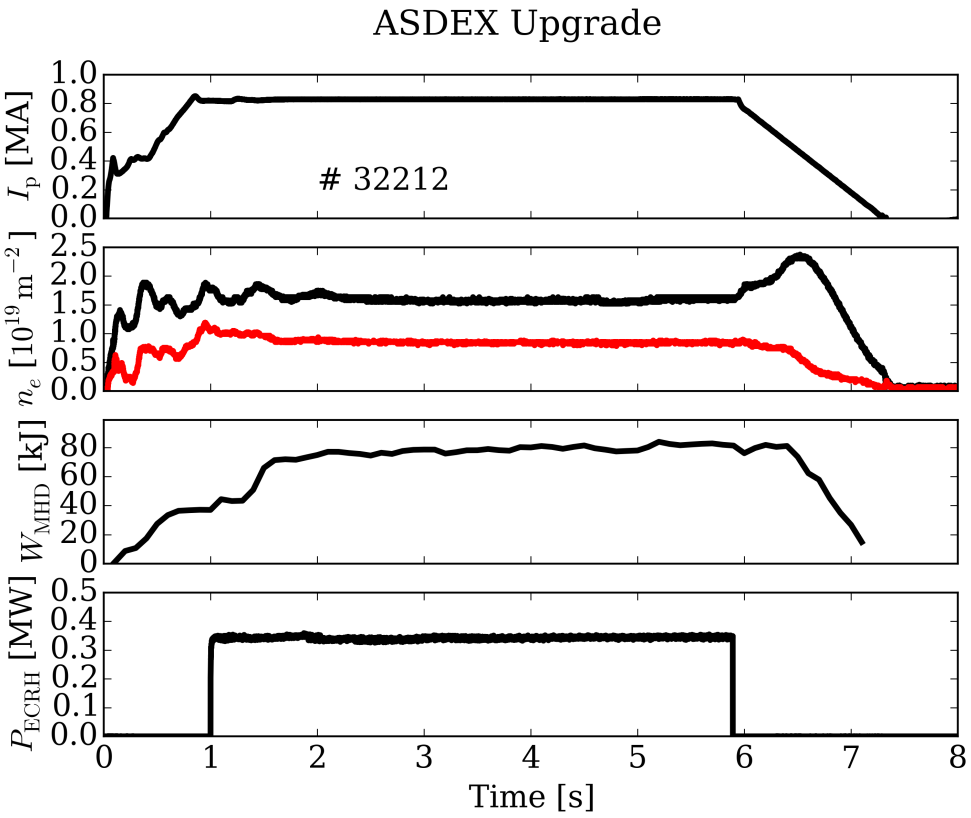

Figure 4.2: Time traces of global plasma parameters for the reference shot # 32212 without external magnetic perturbation until 4.5 s and a steady magnetic perturbation phase until 5.0 s. The top panel shows plasma current that is kept at 0.8 MA. The second panel shows core and edge line integrated density in black and red, respectively. The third panel shows the stored energy in the plasma. The bottom panel shows the external heating.

The red curve shows the heat flux profile for the phase with magnetic perturbation. The profile in presence of a magnetic perturbation is characterized by multiple distinguishable peaks as described in section 2.2.1 for which the 1D diffusive model cannot be applied. A hot spot is present, marked in the figure with a grey area. This hot spot exhibits a larger temperature increase. This leads to an overestimation of heat flux at the position of the hot spot. The area is thus excluded from further discussions.

4.2 Influence of the Magnetic Perturbation Configuration on the Heat Flux Pattern

In this section heat flux measurements with variations in the applied magnetic perturbation are presented. A scan of the *differential phase* between upper and lower row of the magnetic perturbation coils is discussed. Additionally, the influence of the perturbation strength, altered with a change in the magnetic perturbation coil current amplitude and the influence of the fundamental toroidal mode number on the heat flux variation are investigated.
The heat flux profiles obtained from the model (see section 3.2) are compared to the experimental heat flux measurements. The following numerical values are used for all calculations here unless stated otherwise:

- $L_{\mathrm{OMP}} = 25\,\mathrm{m}$.
- $\lambda_{\mathrm{q}} = 3.5\,\mathrm{mm}$, $S = 0.3\,\mathrm{mm}$ (deduced from measurement from #32217 @ 2.3 s (see figure 4.1, i.e. without magnetic perturbation).
- $T_{\mathrm{e,sep}} = 43, 42, 45\,\mathrm{eV}$ for the axisymmetric, *resonant*, *non-resonant* case, respectively. The separatrix temperature is set to match the peak heat flux from the IR measurement. This leads to values consistent with the input power for L-Mode in ASDEX Upgrade.

The plasma boundary displacement of the discussed discharges is calculated and compared to two models in [Kirschner, 2017]. This revealed an overall good agreement between the measured displacement and VMEC calculations and are in agreement with vacuum field calculations for the discharges discussed in the *differential phase* scan.
The scrape-off layer plasma was modelled using EMC3-Eirene [Feng et al., 1997] for the presented discharge #32217 showing agreement with results obtained using the vacuum field approximation as well as using an ad hoc screening model [Brida et al., 2017].
The *resonant* and *non-resonant* discharges were modelled using JOREK [Orain et al., 2016] showing a consistent trend, a reduced divertor heat flux variation in the *non-resonant* configuration compared to the *resonant* configuration, with the observed heat flux variation in the experiment as discussed in this section.

4.2.1 Influence of the Differential Phase on the Heat Flux Pattern

The *differential phase* is used to change the poloidal spectrum of the applied magnetic perturbation field (see section 2.2). This spectrum has been shown to have significant influence on the discharge behaviour. For example the degree of ELM mitigation and density pump-out [Suttrop et al., 2017] or loss of fast particles [Garcia-Munoz et al., 2013] is varied with the *differential phase*.
The *differential phase* is changed in steps of $\frac{\pi}{2}$ with fixed maximum coil current $I_{\mathrm{coil}} = 1\,\mathrm{kA}$. Additional discharges are performed using only the upper (lower) coils. The *differential phase* of $\Delta\phi = -\frac{\pi}{2}$ is field line aligned at the edge ($q = 5$ surface) and is therefore called the *resonant* configuration (see section 2.2). The *differential phase* with $\Delta\phi = +\frac{\pi}{2}$ is anti-aligned and therefore called *non-resonant* configuration, accordingly. The *resonant* configuration with a reduced amplitude of the magnetic perturbation field $I_{\mathrm{coil,red}} = \frac{1}{\sqrt{2}}\, I_{\mathrm{coil}}$ is performed to investigate the influence of perturbation strength on the 2D structure and changes in transport properties in the scrape-off layer (see section 4.2.2).
The heat flux evolution on the outer divertor target measured with an IR thermography system for various *differential phases* are shown in figure 4.3. As mentioned before the magnetic perturbation is rotated leading to a changing heat flux structure in time for all discharges in phases with the magnetic perturbation switched on. The largest visual influence of the magnetic perturbation on the heat flux profile evolution is observed in the *resonant* configuration, see figure 4.3(a). It is observed that the strike line position, identified as the sharp rise of the heat flux profile along the target location, moves in time when the magnetic perturbation is present. This is due to imperfections of the position control in presence of an $n = 2$ external perturbation, e.g. [Willensdorfer et al., 2016, Kirschner, 2017], possibly enlarged by the presence of internal modes due to plasma response, for example seen in JOREK simulations [Orain et al., 2017]. For further analysis this is taken into account by shifting the heat flux profiles to a fixed strike line position. The *non-resonant* configuration is shown in figure 4.3(b). The deviation between axisymmetric heat flux without magnetic perturbation (between 2.0 and 2.5 s) and with magnetic perturbation is reduced compared to the *resonant* configuration. However, the helical structure is still present. Discharges with current only in the upper or lower coils are shown in figure 4.3(c) and figure 4.3(d), respectively. The visual heat flux perturbation is more pronounced than in the *non-resonant* configuration but less pronounced than in the *resonant* configuration. The phases in between the *resonant* and *non-resonant* configuration are both performed in a single discharge, shown in figure 4.3(e). No difference is observed between a *differential phase* of $\Delta\phi = 0$ from 2.5-4.1 s and a *differential phase*of $\Delta\phi = +\pi$ between 4.4 and 6.0 s. This leads to the conclusion that the vacuum field *resonant* configuration exhibits the largest variation. A phase shift due to plasma response would lead to differences between the two phases in figure 4.3(e). The heat flux profile evolution with the *resonant* configuration and a reduced current in the coils $I_{\mathrm{coil,red}} = \frac{1}{\sqrt{2}}\, I_{\mathrm{coil}}$, is shown in figure 4.3(f).

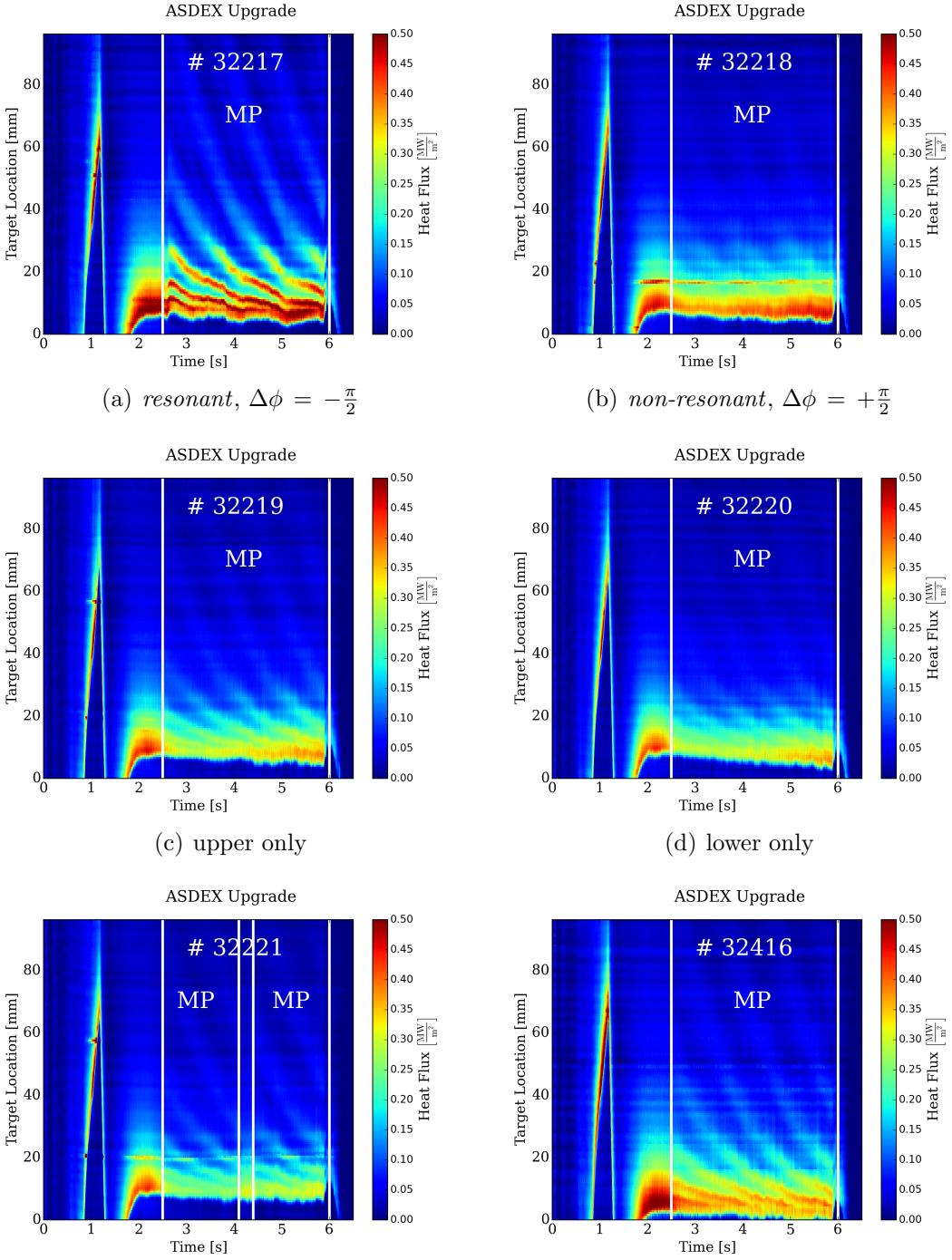

(a) *resonant*, $\Delta\phi = -\frac{\pi}{2}$ (b) *non-resonant*, $\Delta\phi = +\frac{\pi}{2}$

(c) upper only (d) lower only

(e) $\Delta\phi = 0, +\pi$ (f) *resonant*, $\Delta\phi = -\frac{\pi}{2}$ with reduced I_{coil}

Figure 4.3: Experimental heat flux time traces for various *differential phases*. White bars indicate start and end time of the external magnetic perturbation, respectively.

Comparison of the Measured and Modelled Heat Flux Pattern

The 2D structure of the heat flux profile is examined in this section. In order to compare measured with modelled heat flux, time traces from figure 4.3 are related to a toroidal distribution. This is justified by the constant background plasma parameters and the similarity between a toroidal variation and a variation due to the rotated magnetic perturbation field. The rotation of the magnetic perturbation field together with the eight magnetic perturbation coils in toroidal direction leads to a variation of the $n = 2$ Fourier component of the order of 5 % in time and is neglected in the following. A comparison between the heat flux variation in toroidal direction and with rotating magnetic perturbation field is presented in appendix B using synthetic data. The strike line position is corrected as afore mentioned. The hot spot present at a fixed target position is thus not at a fixed position any more. It is observed at the target location $s \geq 10\,\mathrm{mm}$ in figure 4.5.
The 2D structure for the *resonant* configuration is shown in figure 4.4.
Note, the scale in toroidal direction and along the divertor target are a factor of 100 different; the circumference of ASDEX Upgrade is in the order of 10 m ($\pi \hat{=} 5\,\mathrm{m}$) and the (visible) extent along the target location is in the order of 5 cm. The toroidal angle of $\phi = 0$ is set to be heat flux measured at $t = 3\,\mathrm{s}$ at the position of the IR observation. The

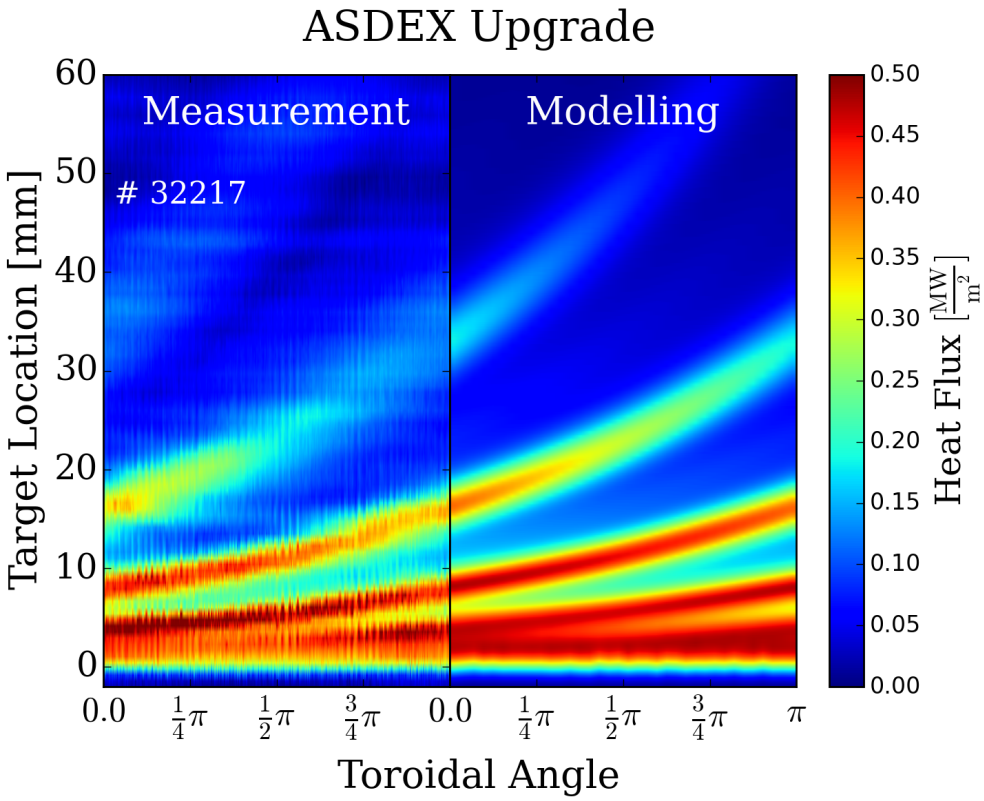

Figure 4.4: 2D heat flux profiles obtained by IR measurements (left) and modelling (right) for # 32217 with a *resonant* external magnetic perturbation.

modelled data is calculated at 3.5 s and shifted to the IR toroidal observation position. The measured and modelled heat flux for the *resonant* magnetic perturbation configuration are in agreement. This is further shown in the toroidal variation in section 4.2.1.
The 2D structure for the *non-resonant* configuration is shown in figure 4.5. The model overestimates the heat flux variation for the *non-resonant* configuration. The measured heat flux variation can be seen in the time trace in figure 4.3(b) being below the heat flux fluctuation level. Although the model predicts less heat flux variation in the *non-resonant* compared to the *resonant* configuration, the predicted variation is above the uncertainty of the measured heat flux from the IR system. The reasons for the overestimation are unknown. A possible explanation might be imperfections in the calculation and definition of the non-axisymmetric separatrix. The influence of the boundary displacement in the model are discussed in appendix C. Further studies, comparing different models, are needed to investigate this discrepancy.

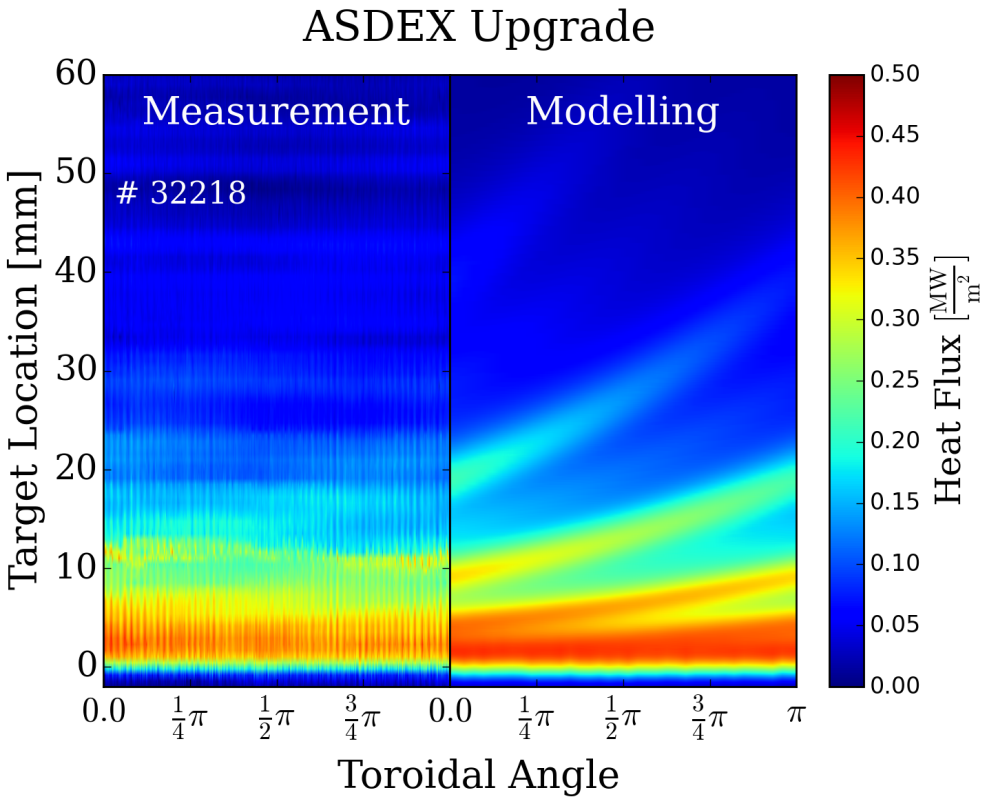

Figure 4.5: 2D heat flux profiles obtained by IR measurements (left) and modelling (right) for # 32218 with a *non-resonant* external magnetic perturbation.

Influence of the Conductive Wall onto the Perturbation Field The ASDEX Upgrade magnetic perturbation coils are mounted on the passive stabilizing loop (PSL, see figure 2.6(a) on page 23). The PSL acts as a low pass filter for plasma oscillations in order to improve the control of the plasma discharge [Gruber et al., 1993]. For a rotation frequency at 1 Hz it is calculated to lead to a phase delay of about $\frac{1}{24}\pi$ (15°) [Suttrop et al., 2009b]. Two discharges with opposite rotation direction, but otherwise the same configuration (*resonant* magnetic perturbation), are performed. Thus, the phase difference between the two discharges should be $\frac{1}{12}\pi$ (30°).
A comparison between both rotation directions is shown in figure 4.6. The dots repre-

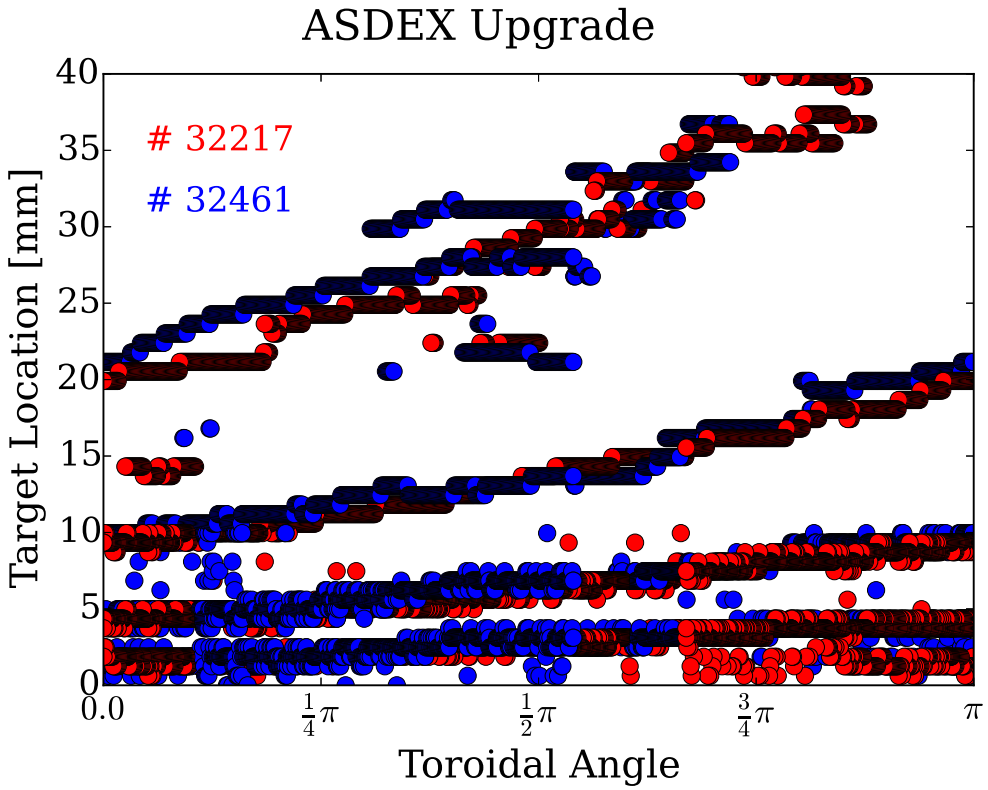

Figure 4.6: Experimental lobe position for both rotation directions without phase shift.

sent the target location of local maxima s_m in direction of the target location s, $q(s_{\mathrm{m}-1}) < q(s_\mathrm{m}) > q(s_{\mathrm{m}+1})$ with m being measured target locations from IR. The location is restricted to positions with a heat flux density $q > 0.1\frac{\mathrm{MW}}{\mathrm{m}^2}$. The agreement obtained without a phase shift between the profile close to the strike line position cannot be improved by adding a phase shift. The distribution close to the strike line is nearly toroidal due to the X-point geometry. The change in the target location along the toroidal direction is less than 5 mm per π up to one λ_q away from the strike line position. A phase shift is not resolvable with the IR system close to the strike line due to the limited spatial resolution of approximately $0.6\,\frac{\mathrm{mm}}{\mathrm{px}}$. Further into the scrape-off layer the change in target location along the toroidal

direction becomes larger. However, the determination of local maxima gets more uncertain with less arriving heat flux. A phase shift in the expected range of $\frac{1}{12}\pi$ is not resolvable with the heat flux data from the utilized IR system and heat flux evaluation.
The low pass filtering due to the PSL not only leads to a phase shift but also to an attenuation of the amplitude. The amplitude is reduced by about 25 % compared to a static field at a frequency at 1 Hz according to [Suttrop et al., 2009b]. This attenuation is accounted for in the calculation of the magnetic field for the modelling.
The positions of local maxima in the modelled heat flux distribution as well as in the experiment for the *resonant* configuration are shown in figure 4.7. The position of local maxima

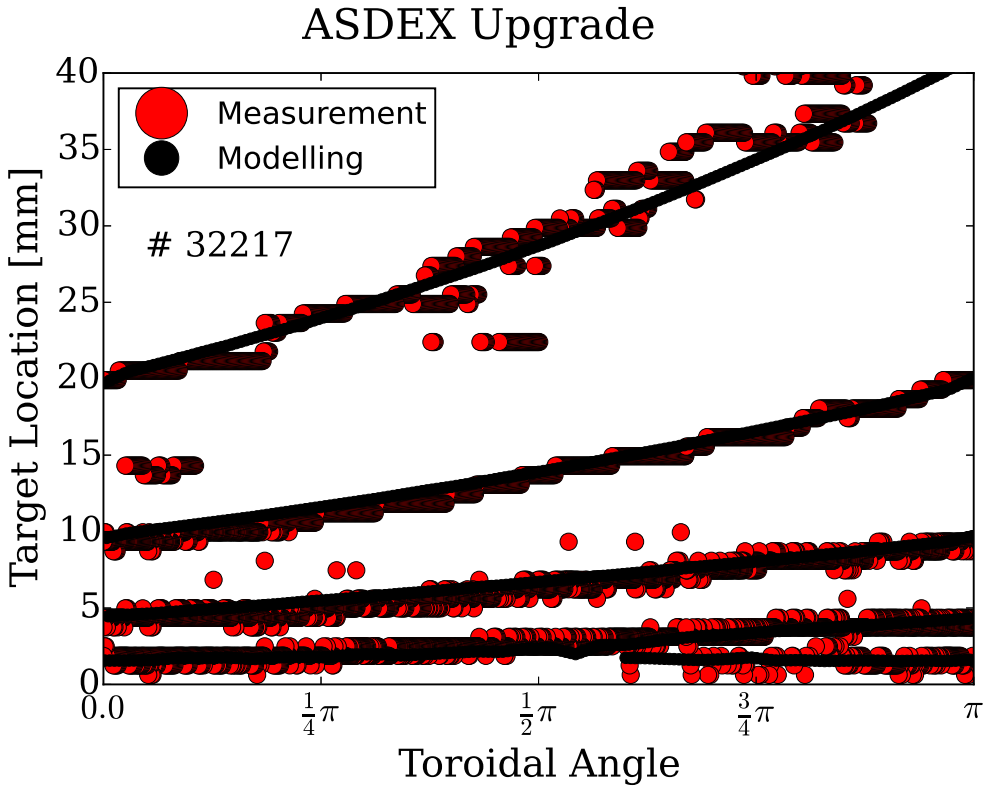

Figure 4.7: Lobe position for modelling (black) and experiment (red dots) for # 32217 with a *resonant* magnetic perturbation.

is in agreement within the measurement uncertainty. However, as already discussed before, phase information in measured data is limited due to the nearly toroidal direction close to the strike line due to the X-point shear.
The local maxima for three different coil configurations from modelling are shown in figure 4.8. It is observed that the relative position of the maxima is independent of the coil current set-up, as discussed in section 3.2.2. The local maxima represent two fixed upstream toroidal positions (magnetic perturbation with a toroidal mode number $n = 2$) at the outer mid-plane. The outer mid-plane toroidal angle is fixed by the absolute phase of

the magnetic perturbation, the position at the target is - after shifting to the same absolute phase - independent of the magnetic perturbation. This holds as long as the perturbation is small as well as no significant non ideal plasma response shifts the absolute phase of the perturbation, e.g. [Liu et al., 2011, Orain et al., 2017].

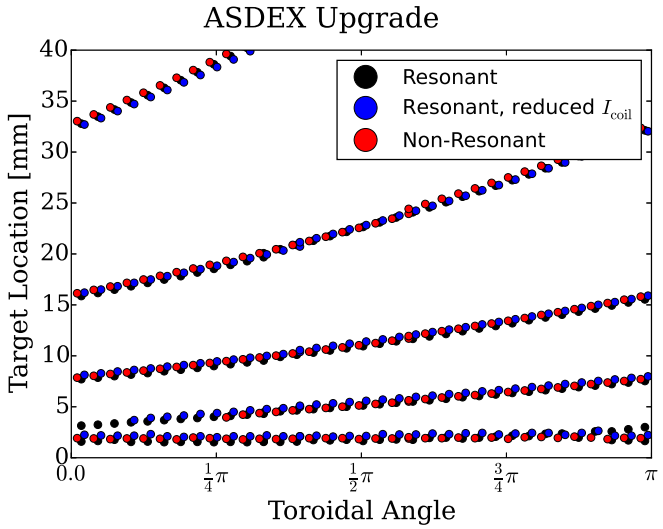

Figure 4.8: Lobe position for the *resonant* configuration with two different coil currents I_{coil} and for the *non-resonant* configuration from modelling.

Toroidally Averaged Heat Flux Profiles

From the 2D heat flux profile a toroidally averaged heat flux is calculated, using the definition in equation (2.36) for $\langle q(s)\rangle_{\phi}$. Experimental and modelled heat flux at four different phases during the rotation of the *resonant* configuration are shown in figure 4.9. The before mentioned hot spot is observed (grey area in figure 4.9(a)) leading to an overestimation of local heat flux at this position but does not affect the analysis and the fitting to the averaged profile. The maximum heat flux in all phases is close to the axisymmetric maximum and the maximum of the averaged profile. This is in agreement with modelled heat flux profiles shown in figure 4.9(b).
In figure 4.10 heat flux profiles for discharges with varying *differential phase* are shown. The heat flux time traces for the discussed discharges are displayed in figure 4.3. A normalization is performed because integrated heat flux in different discharges varies in the order of 10 %. This is within regularly observed L-Mode heat flux variations. The heat flux profiles are normalized with the integrated heat flux for a given profile and to the peak heat flux of the reference profile for # 32217[1].
In figure 4.10(a) heat flux profiles at 2.3 s are shown. This is within the reference phase

[1] A normalization to the peak heat flux for the individual profiles would result in the same figure due to the similarity of the profiles.

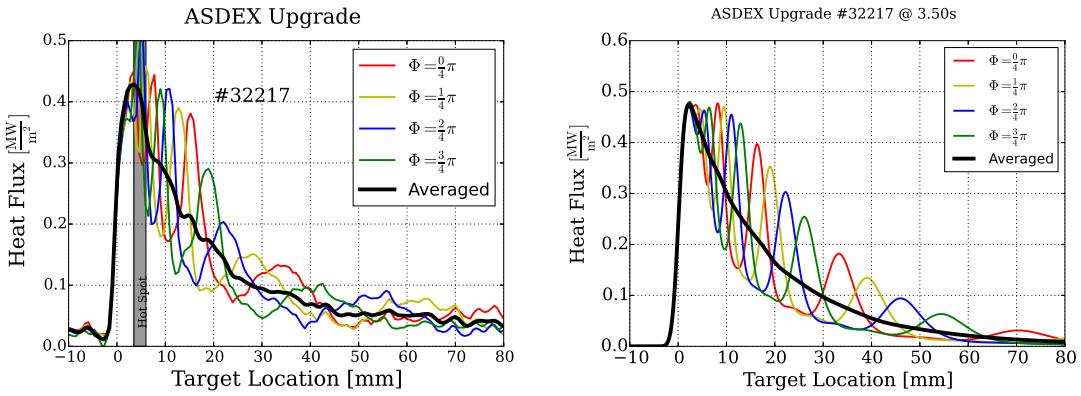

(a) Measurement.

(b) Modelling.

Figure 4.9: Heat flux profiles for different time points (toroidal angles) as well as the averaged profile in the *resonant* configuration.

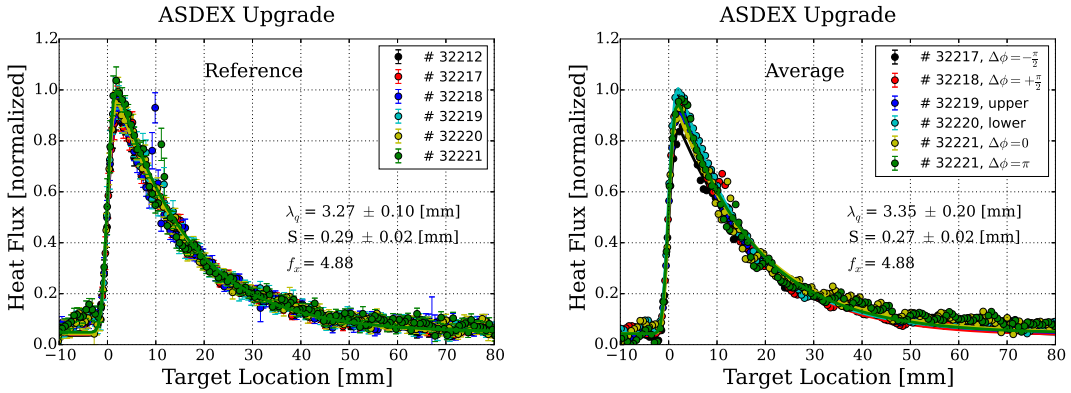

(a) Heat flux profiles in the reference time window without magnetic perturbation.

(b) Time averaged heat flux profiles in presence of an external magnetic perturbation with different phases between upper and lower magnetic perturbation coil currents.

Figure 4.10: Measured heat flux profiles with and without magnetic perturbation.

before the magnetic perturbation field is applied at 2.5 s. The profiles for all discharges are similar and described by the 1D diffusive model (see equation (2.17) on page 13). From this it is concluded that the discharges are comparable in terms of edge transport leading to the observed heat flux pattern. Both transport qualifiers, λ_q and S, obtained by fitting the 1D diffusive model to the experimental data, vary only within the fitting uncertainty. The presented uncertainty is the standard deviation for the obtained values between the discharges.

In figure 4.10(b) time averaged profiles in the phase with rotated magnetic perturbation field are shown. For averaging a time window between 3.0 s and 5.0 s is chosen. Except

for # 32221 where two different *differential phases* are applied and therefore two separate averaged profiles are conducted between 2.7 s and 3.7 s for $\Delta\phi = 0$ and between 4.5 s and 5.5 s for $\Delta\phi = +\pi$. The time windows are chosen to avoid transient phases during switching of the external magnetic perturbation. Averaging over 2.0 s (except for # 32221), which corresponds to two periods, ensures that no artificial heat flux variations are present. The averaged heat flux profiles, in contrast to single profiles (as shown in figure 4.9), are described by the 1D diffusive model. No dependence of the averaged profile on the *differential phase* is observed, in contrast to the different time variations shown in figure 4.3. This is in agreement with the toroidal averaged heat flux obtained by the model also not showing deviations from calculations without magnetic perturbation.
The parameters describing heat transport in the scrape-off layer, λ_q, as well as the divertor region, S, do not show a dependence on the magnetic perturbation. This is interpreted that there is neither significant additional cross-field transport $\chi_\perp$ nor significant additional net radial transport along radially deflected field lines due to the change of radial magnetic field caused by the magnetic perturbation. The lobe structure causes a redistribution of heat flux in toroidal direction with an averaged target profile $\langle q(s)\rangle_\phi$ described by the global λ_q and S.

Toroidal Heat Flux Variation

As shown in the previous section, the time averaged profile with rotating magnetic perturbation is the same as the 1D heat flux profile without magnetic perturbation for the presented discharges. Averaging in time with rotating magnetic perturbation is equivalent with averaging in toroidal direction for a static magnetic perturbation or an infinite fast rotation. Due to the finite rotation frequency in the experiment (1 Hz) the 2D structure on the target is measured by moving it through the field of view of the IR system.
In figure 4.11 heat flux for different target locations in the scrape-off layer, normalized to the averaged heat flux at each position, is shown for the *resonant* configuration (see q' in equation (2.36)). A time window between 3.0 s and 5.0 s is chosen containing two complete periods of the rotation. The target location is expressed in terms of the fitted λ_q for the averaged heat flux profile. Note here, that for convenience the flux expansion f_x is dropped when discussing the target location in terms of λ_q. The black profile ($s = 0.21 \cdot \lambda_q$) corresponds to about the peak in the heat flux profile. Further into the scrape-off layer ($s > \lambda_q$) the IR data becomes more noisy due to the lower signal. The dots show the single IR measurements, the solid line is smoothed over 125 ms (100 time points). The variation between the single time points and the averaged is mainly due to typical heat flux variations in L-Mode and only to a small fraction due to measurement noise.
The measured heat flux variation for the *resonant* configuration is shown in figure 4.11(a). The period in which heat flux is above the mean value is about the same as the period in which it is below with a nearly sinusoidal structure. The peak to peak variation varies for the different target locations, with the largest at about $0.67 \cdot \lambda_q$ away from the strike line with about a factor of 4 in the measurement. Positions further in the scrape-off layer have less heat flux variation and less averaged heat flux. Positions closer to the strike line have

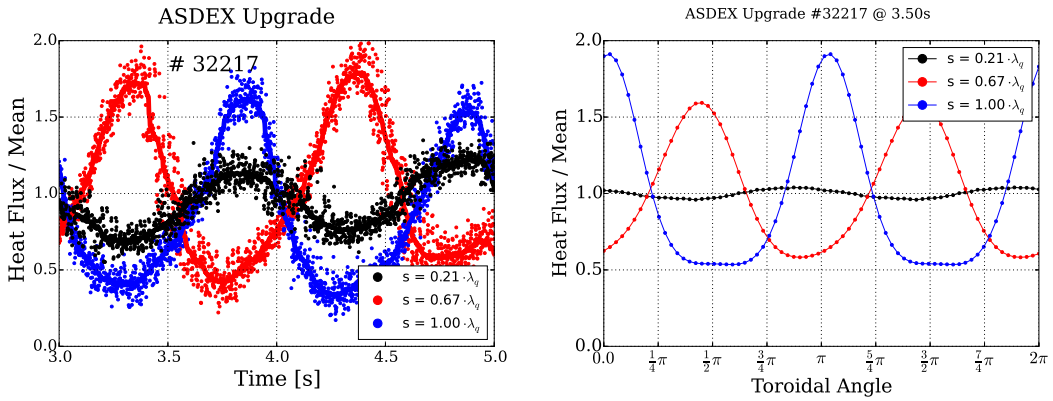

(a) Measurement. (b) Modelling.

Figure 4.11: Heat flux time (toroidal) traces for different target locations normalized to the average heat flux at each position in the *resonant* configuration.

less heat flux variation compared to $0.67 \cdot \lambda_q$ away from the strike line position but with a higher averaged heat flux. This is a direct consequence of the X-point configuration. The slope of the target location depending on the toroidal angle increases with increasing target location. At the strike line position field lines diverge in length and thus all toroidal angles at the target are reached at the same target location s leading to a toroidally symmetric profile at the strike line. This is independent of the heat flux width and set by the (unperturbed) field configuration (see section 3.2.2). However, the most critical part for local over-heating along the target location is around λ_q away from the strike line, where significant averaged heat flux with a strong variation with the cycle of the magnetic perturbation rotation is observed. This is especially given with a partially detached divertor as foreseen in e.g. ITER [Loarte et al., 2007, Pitts et al., 2009], with a reduced heat and particle flux close to the strike line shifting the target peak heat flux further into the scrape-off layer [Kallenbach et al., 2015]. This is further discussed in section 4.3.
The modelled heat flux variation for the *resonant* configuration is shown in figure 4.11(b). The amplitude of the variation is about the same as in the measurement. However, the variation is less sinusoidal and more triangular. Additionally, the variation increases with increasing target location. A more detailed comparison for the variation depending on the target location, *toroidal maximum*, is presented in figure 4.12. The toroidally averaged heat flux profile (mean or $\langle q(s) \rangle_\phi$) is shown in red, the toroidal maximum (max or $\Gamma(s)$) in blue with the normalization described in section 4.2.1. The maximum profile reveals the extent along the target which is above a certain heat flux. The *toroidal maximum* is shown in black. The measurement, shown in figure 4.12(a), exhibits some deviations from the model, figure 4.12(b). The maximum value in the model is never exceeding the peak value of the averaged profile whereas in the experiment the maximum is of the order of 20 % larger than the averaged peak value. However, a hot spot in the measurement close to the peak position leads to an overestimation. The *toroidal maximum* in the experi-

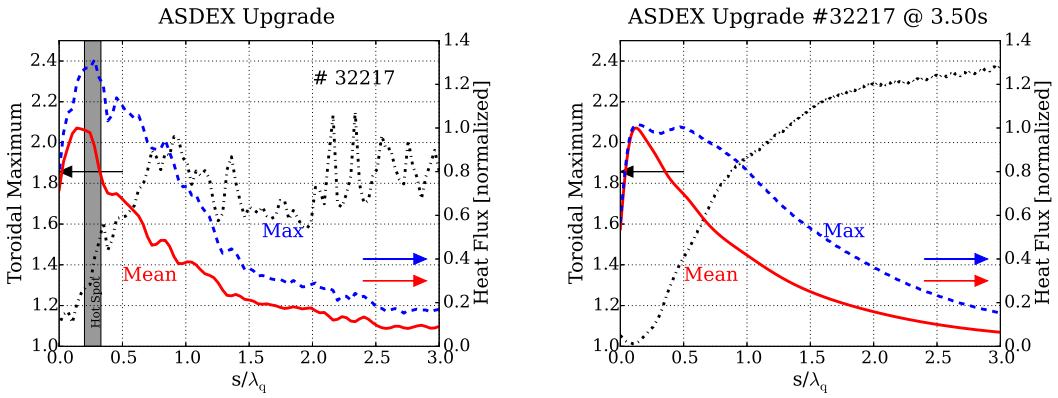

(a) Measurement. (b) Modelling.

Figure 4.12: Impact of the *toroidal maximum* (black) along the target location together with the toroidally averaged (red) and toroidal maximum (blue).

ment is always about 20 % larger, mainly due to typical L-Mode heat flux variations, see section 4.2.1. In the modelled data the *toroidal maximum* monotonically increases with increasing distance from the strike line position. In the measurement the *toroidal peaking* saturates at a distance of one λ_q. However, since the incident (mean) heat flux decreases with distance to the strike line, the uncertainty becomes larger and the interpretation of this saturation has to be treated with caution.

The proposed explanation for the discrepancies is the divertor broadening S. The 1D diffusive model has a single parameter for the diffusion in the divertor region, leading to an effective parameter S for the complete profile. This value is used for the modelled heat flux. It was shown that the parameter depends on the electron temperature in the divertor volume, sufficiently characterized by the target electron temperature for attached conditions [Sieglin et al., 2016b, Scarabosio et al., 2015]. As a result this might lead to a variation along the divertor target as the temperature is not constant. An increased divertor broadening in the far scrape-off layer explains the reduction in the *toroidal maximum*. A linear increase of the (local) divertor broadening would result in about a constant *toroidal maximum* as observed in the measurement.

In figure 4.13 heat flux for different target locations in the scrape-off layer, normalized to the averaged heat flux at each position, for the *non-resonant* configuration is shown. The measured heat flux variation is shown in figure 4.13(a). For this configuration heat flux does not vary significantly in time, already shown in the time trace in figure 4.3(b). The structure of the perturbation, although only altering heat flux marginal, is still observable in the time trace in figure 4.3(b) but is not observed at single target locations as shown in figure 4.13(a).

The modelled heat flux variation for the *non-resonant* configuration is shown in figure 4.13(b). As shown in figure 4.5 the modelled heat flux variation significantly overestimates the measured variation. Although the *toroidal peaking* is reduced from 1.9 in the

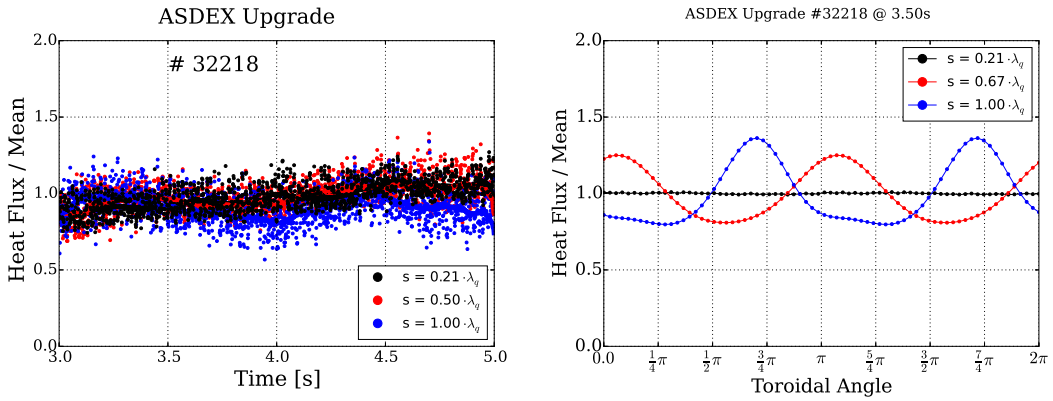

(a) Measurement. (b) Modelling.

Figure 4.13: Heat flux time (toroidal) traces for different target locations normalized to the average heat flux at each position in the *non-resonant* configuration.

resonant configuration to 1.4, the measured heat flux variation is clearly reduced further to below the measurement accuracy.
A variation in time with the rotating magnetic perturbation is also observed by divertor Langmuir probes. The normalized temperature measured by three probes in the scrape-off layer for the *resonant* configuration is shown in figure 4.14. It has to be noted that the

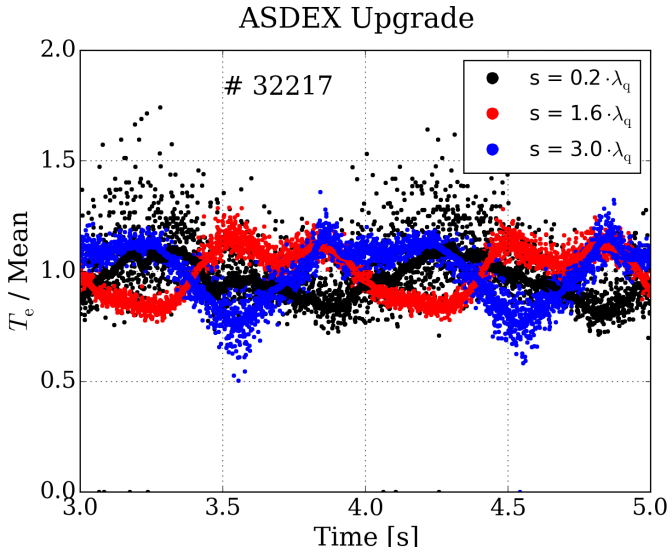

Figure 4.14: Relative electron temperature time traces on the outer divertor target for the *resonant* configuration measured with fixed Langmuir probes.

spatial distance between the probes is 20 mm and there was no strike line sweep in the discharge. Thus, the spatial resolution is low compared to the size of the lobes and no proper profile can be constructed. The about sinusoidal oscillation observed in the heat

flux profile measured by the IR thermography system is also observed in target electron temperature. However, compared to the peak to peak heat flux variation of up to a factor of 4, the variation in target electron temperature is in the range of 20 %. The position of the two probes in the scrape-off layer is substantially further away from the strike line position than the positions where the heat flux variation is extracted from. The probe data shown in black is taken at about the peak heat flux position measured by the IR thermography system. Note here, that IR thermography data is shifted due to a strike line movement, this is not possible for Langmuir probe data due to the limited spatial resolution.

4.2.2 Influence of the Magnetic Perturbation Amplitude on the Heat Flux Pattern

The influence of the magnetic perturbation amplitude for the *resonant* and *non-resonant* configuration on the *toroidal peaking* in the model is shown in figure 4.15. For zero coil

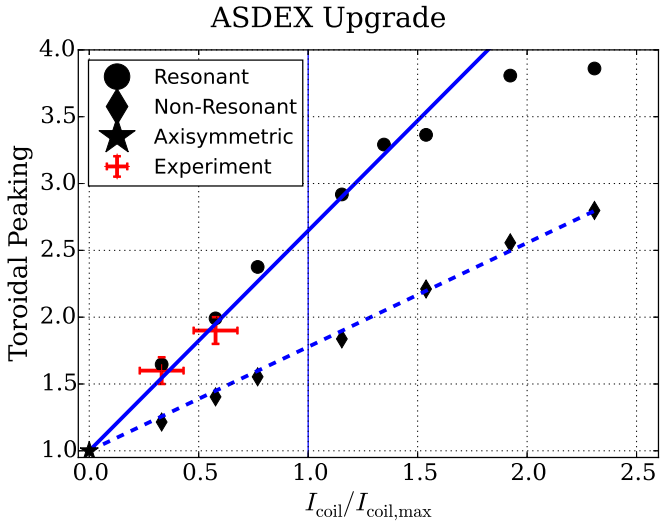

Figure 4.15: Modelled *toroidal peaking* for different coil currents. The current is normalized to the maximum possible current of the ASDEX Upgrade coils.

current an axisymmetric heat flux is expected, having a *toroidal peaking* of 1.0. The coil current in the figure is normalized to the maximum coil current of the ASDEX Upgrade coils (1.3 kA x 5 turns). The nominal current used in the presented study is 5 kAt, the PSL attenuates 25 % of the magnetic field. The normalized coil current in the experiment is ≈ 0.6 in # 32217 and ≈ 0.42 in # 32416. In order to rotate the field with a constant amplitude the effective magnetic perturbation is a square-root reduced for the same coil currents (not all coils have the maximum current at the same time). This is not reflected in the normalization, all experimental data in this thesis are from discharges with a rotated magnetic perturbation field. The magnetic perturbation coil currents used for modelling are taken from # 32217 (# 32218) for the *resonant* (*non-resonant*) configuration, having

the same effective magnetic perturbation amplitude as in the experiments with rotated magnetic perturbation field. The perturbation strength with a static field can be about 1.9 times larger with the same current limit of 5 kAt.
The modelled *toroidal peaking* increases nearly linear with increasing current for a given *differential phase*. The slope is different for the two configurations, the *resonant* configuration has a larger *toroidal peaking* with about a factor two difference in slope. For too high currents in the model (more than 2.0 times the maximum current possible in the experiment) this linear dependence is lost. This is due to the large influence of the perturbation and might be an artefact of this model. The red crosses in the figure show the *toroidal peaking* for the *resonant* case observed in the experiment in line with the linear increase and the absolute value. However, in figure 4.13(a) it is shown that the experimental *toroidal peaking* for the *non-resonant* case at a normalized current of 0.6 is well below the 1.4 observed in the model.

4.2.3 Influence of the Toroidal Mode Number on the Heat Flux Pattern

One essential property of magnetic perturbations is the (fundamental) toroidal mode number. The most exploited toroidal mode number at ASDEX Upgrade is $n = 2$. This is partially due to technical restrictions with four power supplies for the 16 coils. Recently, the power supply system was upgraded in order to individually supply each coil and thus having increased flexibility [Teschke et al., 2017]. This allows for rigid rotations with various *differential phases* for $n = 1$-3 as well as combinations of these.
The toroidal mode number not only changes the symmetry of the 2D heat flux pattern, but also the *toroidal peaking* as well as the interplay with rational surfaces in the confined region. The latter is discussed in section 4.4 due to substantial differences in heat loads that occur with *mode penetration* observed with $n = 1$ magnetic perturbation at -2.5 T and with $n = 2$ at -1.8 T if I_{coil} is above a certain threshold.
In figure 4.16 a discharge with an external magnetic perturbation with $n = 3$ is shown. This

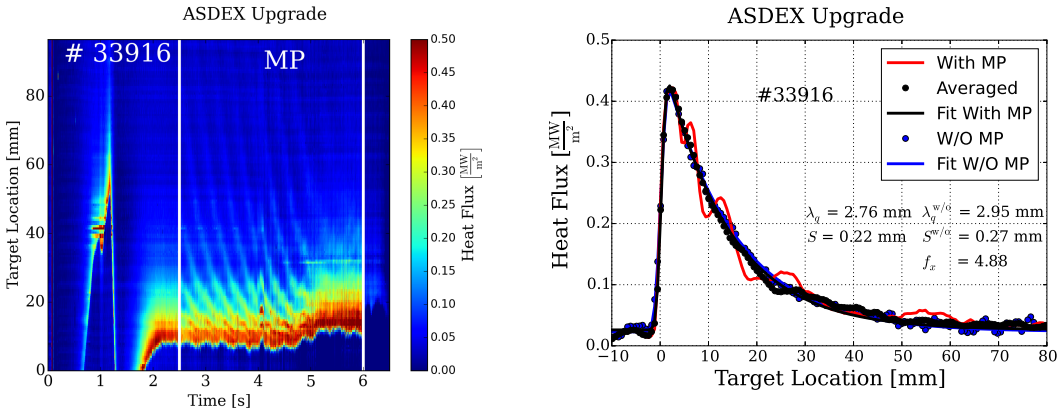

(a) Time trace.

(b) 1D profiles.

Figure 4.16: Measured heat flux profiles for ASDEX Upgrade discharge # 33916 with $n = 3$ magnetic perturbation with $I_{\text{coil}} = 1.25\,\text{kA}$ and $B_{\text{tor}} = -1.8\,\text{T}$.

discharge has an increased perturbation current, $I_{\text{coil}} = 1.25\,\text{kA}$, compared to the $n = 2$ at $B_{\text{tor}} = -2.5\,\text{T}$ discussed so far ($I_{\text{coil}} = 1.00\,\text{kA}$). As in the discussion for the time averaged profiles with $n = 2$, the averaged profile (black) is similar to the axisymmetric reference without a magnetic perturbation (blue). The *differential phase* is *resonant*, but the toroidal variation is significantly smaller compared to the discharge with $n = 2$ *resonant* magnetic perturbation (see figure 4.1 on page 40), despite the larger perturbation amplitude.
Modelled heat flux profiles for $n = 1$-3 are shown in figure 4.17 for fixed values of λ_q and S and without taking the separatrix corrugation into account (see appendix C). The toroidal angle is shown for one period each. In order to compare the difference in the toroidal variation, three target positions are shown in figure 4.18 for each toroidal mode number. Here, the complete toroidal angle is shown in order to display the periodicity. Taking the

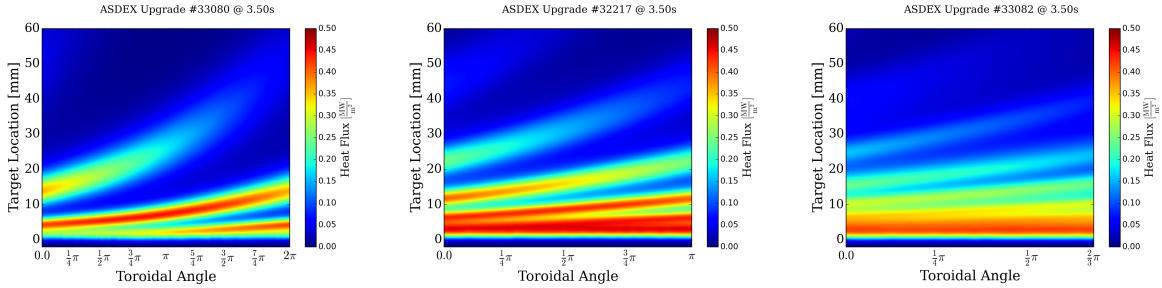

(a) $n=1$ (b) $n=2$ (c) $n=3$

Figure 4.17: Modelled 2D heat flux profiles for different toroidal mode numbers.

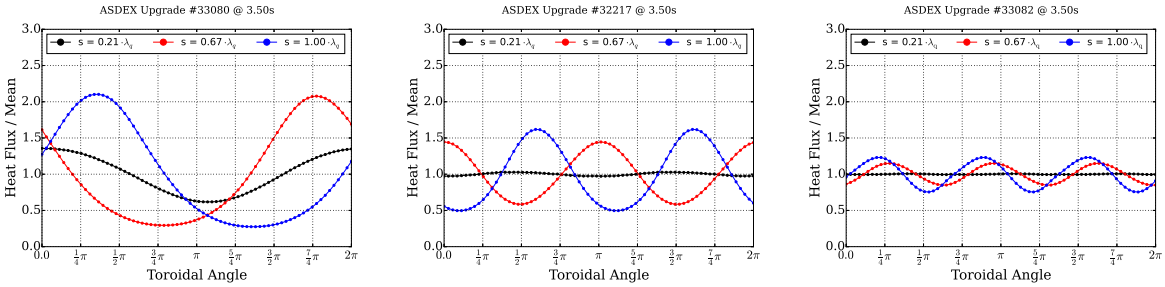

(a) $n=1$ (b) $n=2$ (c) $n=3$

Figure 4.18: Toroidal heat flux variation for different toroidal mode numbers from modelling.

maximum at a distance of λ_q, which is the definition of the *toroidal peaking* σ, we get $\sigma = 2.1, 1.6, 1.2$ for $n = 1, 2, 3$, respectively. The measured heat flux variation is in qualitative agreement, but does not allow a quantitative comparison. This is due to the different magnetic perturbation strength for the $n=2$ and $n=3$ discharges and the fundamental difference with $n=1$ that is discussed in section 4.4.

Mixed Toroidal Mode Numbers The ASDEX Upgrade magnetic perturbation coil power supply allows for combinations of different fundamental mode numbers. A combination of two fundamental mode numbers is discussed for ITER, e.g. [Li et al., 2017]. However, due to the restrictions on the maximum current in the ASDEX Upgrade magnetic perturbation coils, this reduces the amplitude of each fundamental mode spectrum compared to a single mode number. The heat flux variation is reduced to a level that is not able to be observed with the IR system with a combined $n=2$ and 3 magnetic perturbation. At present it is not possible to study experimentally the effect of multiple toroidal mode number spectra on divertor target heat flux in ASDEX Upgrade.

4.3 Influence of the Density on the Heat Flux Pattern

The *resonant* configuration is used to study the effect of magnetic perturbations on λ_q and S on the outer divertor target at various densities. This *differential phase* has the largest heat flux variation and is in agreement with modelled heat flux as discussed in the previous section. It has been reported that in L-Mode discharges at ASDEX Upgrade both, λ_q and S, increase with increasing electron density at the plasma edge [Scarabosio et al., 2013, Sieglin et al., 2013, Sieglin et al., 2016b], see section 2.1.1.3. The main mechanism to increase S with density is thought to be the reduction of electron temperature in the divertor region and, therefore, the reduction of parallel heat conduction [Scarabosio et al., 2015, Sieglin et al., 2016b]. The increase of λ_q with increasing density is thought to be an effect of a decrease of edge electron temperature [Sieglin et al., 2016b] discussed for TCV discharges in chapter 5.
A density scan is performed to be able to choose densities that are low enough to have an attached divertor and no significant divertor radiation. These conditions result in $T_{e,tgt} > 10\,eV$, whilst still spanning an as large as possible density range. To study the toroidally averaged profiles, stable conditions are needed. Three discharges with different density levels are referred to as *low*, *medium* and *high* density corresponding to a line integrated edge density of $n_{e,edge} = 0.8, 1.5, 1.8 \cdot 10^{19}\,m^{-2}$, respectively[2].
The 2D heat flux profiles are shown in figure 4.19, *medium* density in figure 4.19(a) and *high* in figure 4.19(b). The *low* density reference has already been shown in figure 4.3(a) on page 45. In all three discharges the 2D structure of the heat flux profile is seen. Comparing

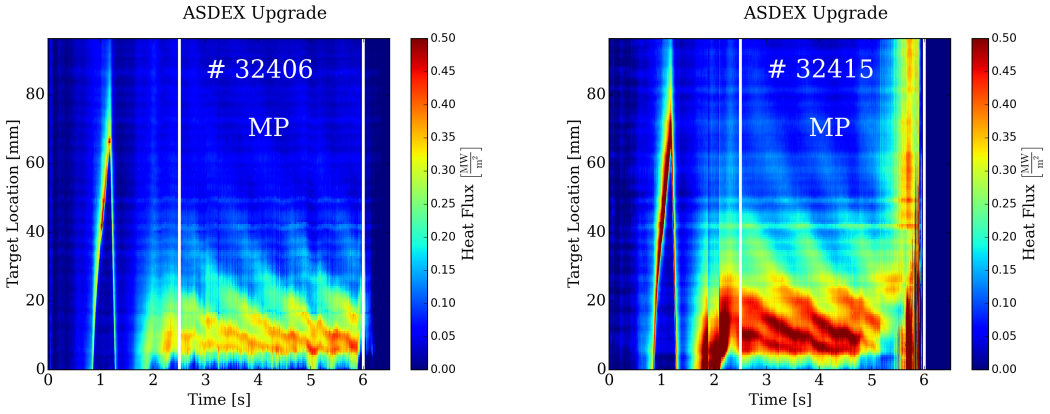

(a) Medium density, $n_{e,edge} = 1.5 \cdot 10^{19}\,m^{-2}$. (b) High density, $n_{e,edge} = 1.8 \cdot 10^{19}\,m^{-2}$.

Figure 4.19: Heat flux time traces for the discharges with elevated density. White bars indicate start and end time of the external magnetic perturbation, respectively.

[2]The terms of *low*, *medium* and *high* density are a choice of convenience for this study. They do not refer to operation at high density essential for high fusion performance and high radiative scenarios. The densities correspond to a Greenwald density fraction of $\frac{n_{e,core}}{n_{GW}} = 0.14, 0.28, 0.34$ with the Greenwald density $n_{GW} = \frac{I_p}{\pi a^2}$ in $10^{20} m^{-3}$ [Greenwald, 2002].

the profiles for the elevated densities with the *low* density reference reveals that increasing density reduces the heat flux variation. This is shown in figure 4.20 for all three densities. The density difference between the *medium* and *high* density discharges is small and no

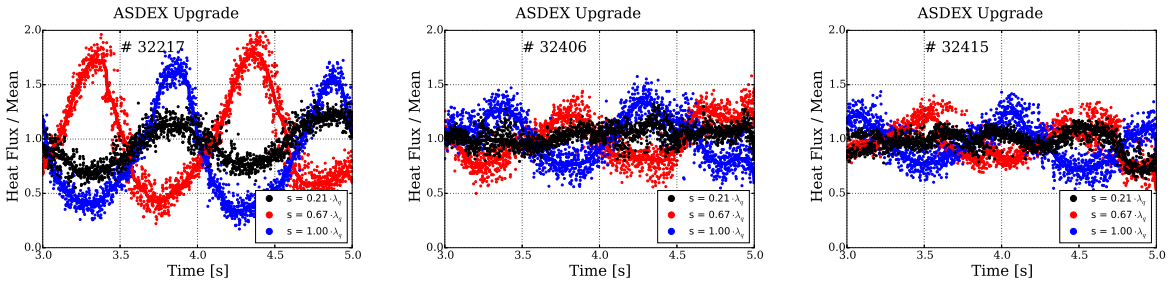

(a) Low density, $n_{\mathrm{e,edge}} = 0.8 \cdot 10^{19}\,\mathrm{m}^{-2}$.

(b) Medium density, $n_{\mathrm{e,edge}} = 1.5 \cdot 10^{19}\,\mathrm{m}^{-2}$.

(c) High density, $n_{\mathrm{e,edge}} = 1.8 \cdot 10^{19}\,\mathrm{m}^{-2}$.

Figure 4.20: Measured heat flux time traces for different target locations normalized to the average heat flux at each position.

clear difference in the variation in time of heat flux is seen. The variation in both cases is around 20 %.
In figure 4.21 a comparison between measured heat flux profiles in the reference time window (figure 4.21(a)) and toroidally averaged profiles with magnetic perturbation (figure 4.21(b)) are shown. The normalization is the same as in section 4.2.1. As mentioned

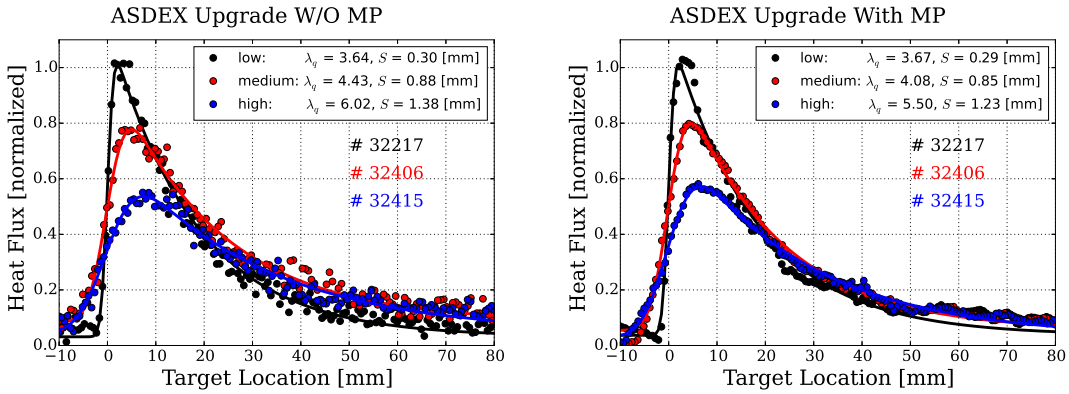

(a) Without magnetic perturbation.

(b) With magnetic perturbation.

Figure 4.21: Measured heat flux profiles with and without magnetic perturbation for three different densities.

in the beginning of the section, an increase for both, λ_{q} and S, is expected for increasing density in ASDEX Upgrade L-Mode. This is confirmed in the three density steps without magnetic perturbation as the normalized peak heat flux is reduced by a factor of two due to larger values of both λ_{q} and S. With increasing density the toroidally averaged profiles with

magnetic perturbation are still described by the 1D diffusive model. The transport qualifiers are similar to the reference values without magnetic perturbation and no significant change in the increase of both transport qualifiers with density is observed. The reduced fluctuation level at low heat flux, e.g. between 30 and 80 mm, in the toroidal averaged profiles compared to the profiles without magnetic perturbation is due to the averaging process. The profiles without magnetic perturbation are single time points compared to an average, although with varying heat flux due to the magnetic perturbation, of 2 s with 1600 measurements from the IR system. The fluctuation level with magnetic perturbation can be seen in figure 4.20 being in the same order as without magnetic perturbation.

Influence of the Divertor Broadening on the Heat Flux Pattern

In figure 4.20 it is shown that the *toroidal maximum* decreases with increasing density. From the axisymmetric reference as well as the toroidally averaged profiles it is observed that both transport qualifiers, λ_q and S, increase with increasing density. In the presented model the divertor broadening S is applied after the heat flux calculations and can be varied independently (see equation (3.2.3)). The *toroidal peaking* with varying divertor broadening is shown in figure 4.22. The black dots have a fixed λ_q using the value from

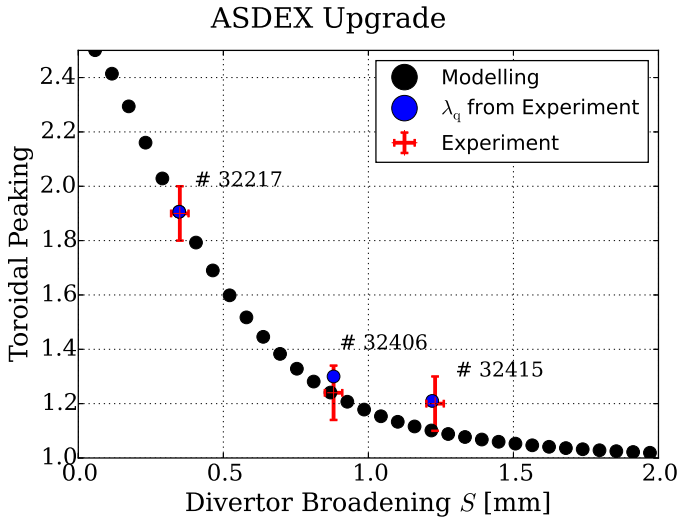

Figure 4.22: *Toroidal peaking* depending on the divertor broadening S.

32217 (*low* density). The blue dots use the value for λ_q from the corresponding discharges. The *toroidal peaking* decreases with increasing divertor broadening S, λ_q does not change this trend significantly. The measured *toroidal peaking* at the fitted divertor broadening S for the three different density steps are plotted in red being in agreement to the modelled values. Thus, the decreasing *toroidal peaking* seen in the experiment with increasing density is explained by the increase of S.
In the model no change in the magnetic perturbation field is needed nor increased heat

transport due to the external magnetic perturbation to explain the density dependence of the heat flux profile with magnetic perturbation. A more detailed characterization with synthetic data scanning both S and λ_q is presented in the following section.

Influence of the Scrape-Off Layer Power Fall-Off Length and Divertor Broadening on the Heat Flux Pattern

It is shown in the last section that S is the dominating parameter in the performed density scan to reduce the *toroidal peaking*. The combined influence of both λ_q and S deduced from synthetic parameter scans is discussed in this section. The magnetic field is kept constant being the same as used for the *resonant* configuration from discharge # 32217 in the previous sections.
For ITER the *toroidal peaking* is a major concern motivating considerations of the magnetic perturbation coils to be able to rotate the magnetic perturbation field in a similar way as performed for the discharges in this chapter [Loarte et al., 2014]. However, alternating currents needed in order to perform such rotations lead to opposing forces on the surrounding structure.
Lower *toroidal peaking* would reduce the requirements for such rotation. Here, considerations for fully attached conditions are discussed where the model for ASDEX Upgrade shows good agreement to measurements. It is noted, that the extrapolation to different operational regimes (detachment, different magnetic perturbation field strength, significant plasma response) and to different machines (ITER) has to be treated with caution due to the assumptions in the model. The model uses the vacuum field approximation shown to be in agreement at low plasma pressure. Plasma response is increased for reactor relevant pressure where the vacuum field approximation is no longer sufficient [Piovesan et al., 2017, Igochine et al., 2017]. Additionally, the model uses the transport qualifiers λ_q and S as input parameters and no transport equations are solved. Heat flux is calculated using electron conduction and the two point model, no volumetric losses are considered. It was shown in [Brida et al., 2017] that the *toroidal peaking* reduces further with increasing density or seeded impurities and (partial) detachment in the divertor.
The *toroidal peaking* leads to a non-axisymmetric heat load on the divertor target or a time variation of heat load if the perturbation field is rotated. The *critical* target location is defined here to be the location with the largest heat flux or the largest variation of heat flux. It has been shown that the detachment process starts at the strike line [Kallenbach et al., 2015]. Partial detachment mitigates heat flux close to the strike line and thus a position farther in the scrape-off layer has the highest heat load under such conditions. However, it is not known if the position of the highest heat flux in partial detached conditions depends on the scrape-off layer power fall-off length.
The *toroidal maximum* increases for increasing target location for a fixed λ_q. In the following discussion two fixed target locations are chosen for the effect of λ_q and S onto the *toroidal maximum*.

In figure 4.23 a fixed $\lambda_q = 3.5\,\mathrm{mm}$ is chosen showing the *toroidal maximum* depending on target location s/λ_q and divertor broadening S. The color bar is chosen to indicate the

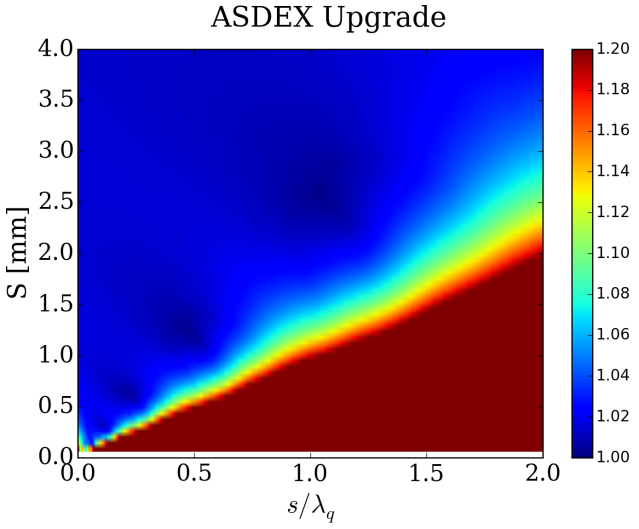

Figure 4.23: *Toroidal maximum* depending on target location s/λ_q and divertor broadening S using a fixed $\lambda_q = 3.5\,\mathrm{mm}$. The color bar is chosen to indicate the *toroidal maximum* up to a factor 1.2. This is arbitrarily set to be an acceptable limit.

toroidal maximum up to a factor 1.2. This is arbitrarily set to be an acceptable limit for the discussion. Using a different value does shift the absolute values but the qualitative observations will be the same.
The necessary value of S to keep the *toroidal maximum* within the limit increases about linear along the target location. This allows to use arbitrary, but fixed target locations for a qualitative discussion in the following.
A constant divertor broadening for the complete profile along the target location is assumed, consistent with the 1D diffusive model. However, it was shown that S depends on the target electron temperature (see section 2.1.1.3) which is proposed to be a proxy for the temperature distribution along field lines in the divertor region [Nille, 2016]. Electron temperature in the far scrape-off layer divertor region is lower compared to the strike line, potentially leading to a larger broadening. Presented scaling laws as well as experimental values in this thesis refer to a single value, dominated by the broadening close to the strike line position and potentially underestimating the effect farther in the scrape-off layer. Thus, a conservative estimation is presented. A larger S in the scrape-off layer farther from the strike line is proposed for the deviation between measurement and modelling for the *toroidal maximum* profile shown in figure 4.12 on page 54.
Two considerations of the *critical* target location are performed. The first one is using the target position as in the definition of the *toroidal peaking* ($s = \lambda_q$). It is shown in section 4.2 that in the experimental data this is the position having the largest *toroidal maximum* for the *resonant* configuration and lowest density whereas in the modelling the

toroidal maximum monotonically increases further into the scrape-off layer.
The second consideration is using a fixed target position, chosen to be $s = 17\,\mathrm{mm}$, which is the position of the *low* density λ_q. Due to the considered fixed magnetic field configuration, the magnetic lobe structure is not varied with changing λ_q and S.
Both considerations are shown in figure 4.24. In figure 4.24(a) the first consideration is

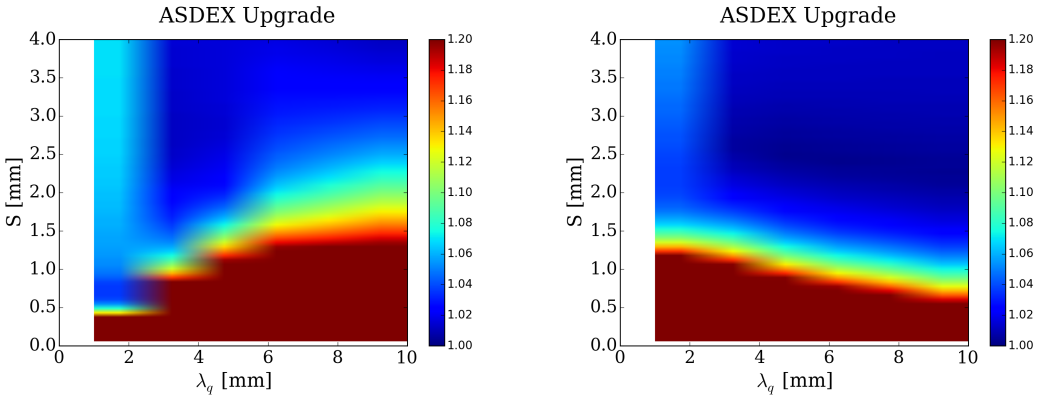

(a) Position of *toroidal maximum* is $s = \lambda_\mathrm{q}$, as in the definition of *toroidal peaking*.

(b) Position of *toroidal maximum* is $s = 17\,\mathrm{mm}$, which is the position of the *low* density λ_q.

Figure 4.24: *Toroidal maximum* depending on λ_q and S for two different target positions. The color bar is chosen to indicate the *toroidal maximum* up to a factor 1.2. This is arbitrarily set to be an acceptable limit.

shown with the target position depending on λ_q. With increasing λ_q the necessary S increases in order to reduce the *toroidal maximum* to an acceptable level.
In figure 4.24(b) a fixed target location is chosen for the *toroidal maximum*. In contrast to a normalization to λ_q, with increasing λ_q the necessary S decreases in order to reduce the *toroidal maximum* to an acceptable level.
A larger value of S is needed to reduce the *toroidal maximum* to an acceptable value if the critical target location depends solely on the magnetic geometry, independent on λ_q. A smaller value of S is needed for a target location depending on λ_q.
ITER has to operate in partial detachment and will have a small $\lambda_\mathrm{q} \approx 1\,\mathrm{mm}$ from the multi machine scaling prediction [Eich et al., 2013] (see section 2.1.1.3). Keeping in mind the limitations of the assumptions of the vacuum field approximation and attached conditions the shown considerations leads to to following qualitative observation:
If the partial detachment extent depends on λ_q the necessary S in order to reduce the *toroidal maximum* to an acceptable level might be significantly smaller compared to the necessary value if the partial detachment extent is independent of λ_q.

4.4 Influence of Field Penetration on the Heat Flux Pattern

In a certain parameter regime [Fitzpatrick, 1998], mainly at low densities (collisionality) and low rotation, an external magnetic perturbation field can penetrate the plasma and lead to full magnetic reconnection generating magnetic islands at resonant flux surfaces [Fietz et al., 2015]. These small islands can act as a seed perturbation for neoclassical tearing modes reducing confinement or leading to disruptions [Hender et al., 1992, Koslowski et al., 2006, Yu et al., 2008, Fitzpatrick, 2012].
Such islands are described by a current sheet on the resonant flux surface[3]. They often lock and amplify the external magnetic perturbation. The effect on the 2D heat flux pattern at the divertor target is shown in figure 4.25 for a magnetic perturbation with $n=1$. Exceeding a threshold in the magnetic perturbation amplitude of $250\,\mathrm{A} < I_{\mathrm{coil}}^{\mathrm{threshold}} < 400\,\mathrm{A}$

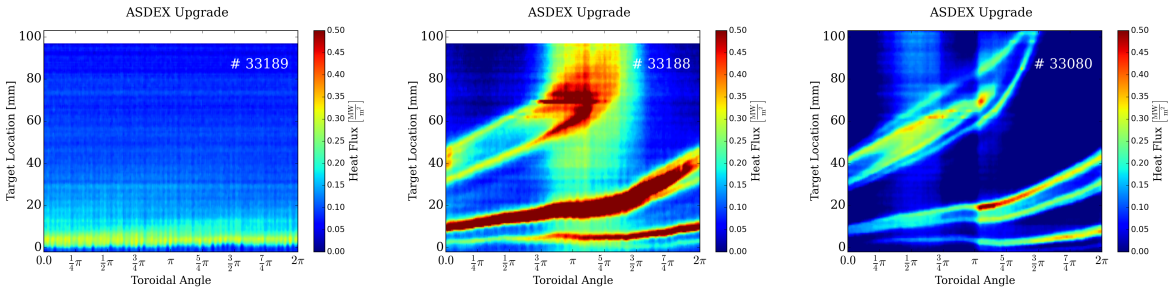

(a) $I_{\mathrm{coil}} = 0.25\,\mathrm{kA}$ (b) $I_{\mathrm{coil}} = 0.4\,\mathrm{kA}$ (c) $I_{\mathrm{coil}} = 1.0\,\mathrm{kA}$

Figure 4.25: 2D heat flux pattern for discharges with $n=1$ magnetic perturbation with different amplitude. The heat flux pattern changes significantly with an amplitude $250\,\mathrm{A} < I_{\mathrm{coil}}^{\mathrm{threshold}} < 400\,\mathrm{A}$, attributed to exceeding a threshold leading to field penetration.

leads to a significant change of the heat flux pattern. The vertical blurry pattern, visible in e.g. figure 4.25(b) between a toroidal angle of $\frac{3}{4}\pi < \phi < \frac{3}{2}\pi$ and figure 4.25(c) between $\frac{1}{2}\pi < \phi < \frac{3}{4}\pi$, are due to reflections from the inner divertor target in the IR signal caused by the large radial extent of the heat flux pattern.
In figure 4.26 a comparison between (a) the 2D heat flux profile from the IR measurement, (b) 2D heat flux using the model described in section 3.2 and (c) connection length using the vacuum field approximation (see section 3.2.2) is shown. The measured heat flux extent is significantly larger than the model prediction and the connection length profile.
However, expanding the connection length profile along the target location, equivalent with increasing the magnetic perturbation amplitude, reveals remarkable similarity between measured heat flux pattern and pattern of connection length, shown in figure 4.27. An expansion factor of 2.5 is used in order to match the extent along the target location of

[3]Due to the distance between the scrape-off layer and the resonant flux surface one can approximate the current as a delta function instead of having a finite width perpendicular to the flux surface.

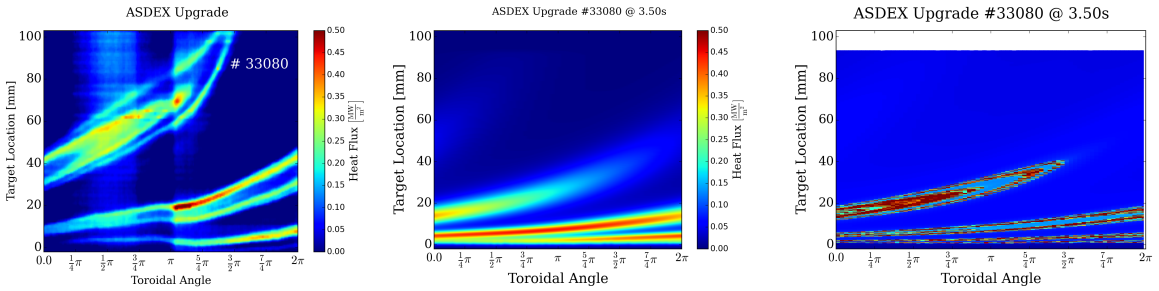

(a) Measured heat flux pattern. (b) Modelled heat flux pattern using the vacuum field approximation.. (c) Connection length using the vacuum field approximation.

Figure 4.26: 2D divertor target pattern for # 33080 with $n = 1$, $I_{\text{coil}} = 1.0\,\text{kA}$.

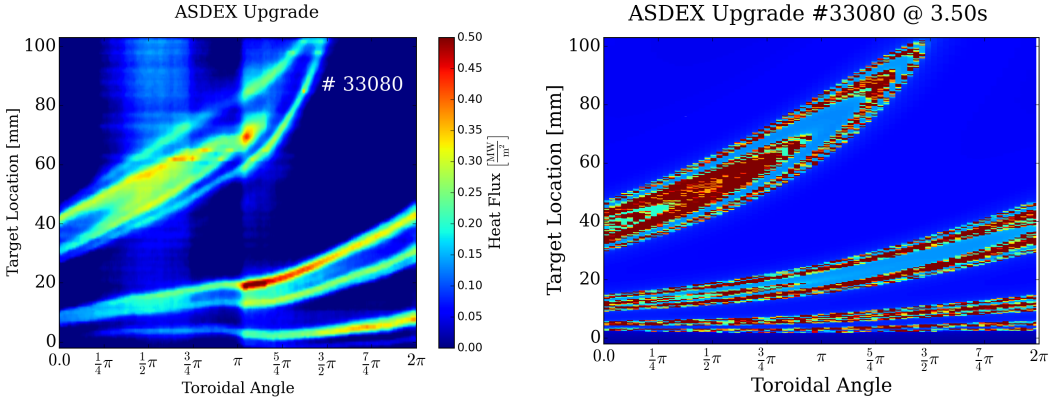

(a) Measured heat flux pattern.

(b) Connection length using the vacuum field approximation, scaled by a factor 2.5.

Figure 4.27: 2D divertor target pattern for # 33080 with $n = 1$, $I_{\text{coil}} = 1.0\,\text{kA}$.

measured heat flux.

This onion like structure is not reproduced using the model. It is observable in connection length calculations due to an ergodization of field lines at the plasma boundary with neighbouring field lines having significant different connection length [Nguyen et al., 1997, Finken et al., 1998]. This ergodization pattern has a characteristic extent with a clearly defined boundary. Such a structure is not observed in the experimental observations and modelling in the sections before. The model uses field line tracing in the vacuum field approximation to map 2D target location to 2D outer mid-plane location. The magnetic perturbation in the vacuum field approximation leads to an ergodization of the plasma boundary which can be seen in the connection length in figure 4.26(c). However, the model uses only the field line between the outer divertor target and the first intersection of the outer mid-plane which leads to a non-ergodic pattern as discussed in section 3.2.2 which is in line with measured heat flux in the previous sections but deviates from the

observations in this section.
In order to mimic the field penetration and the resulting internal mode, current filaments are added along field lines at the resonant surface. These current filaments are treated the same way as the current inside the coils producing the external magnetic perturbation; solving Biot-Savart's law and using the vacuum field approximation. We use a current of the form

$$I_{\text{filament}} = \hat{I} \cos\left(\frac{\Phi_{\text{OMP}} - \Phi_0}{n}\right) \tag{4.1}$$

with $\hat{I}$ amplitude, n toroidal mode number and Φ_{OMP} (Φ_0) toroidal phase of the field line (mode) at the outer mid-plane.
Here, a mode at the $q=2$ surface is assumed with $m=2$ and $n=1$, m being the poloidal mode number. This position is inferred from the electron temperature profile, shown in figure 4.28, measured with an electron cyclotron emission (ECE) system [Rathgeber et al., 2013, Willensdorfer et al., 2016]. The temperature profile at the measurement position is

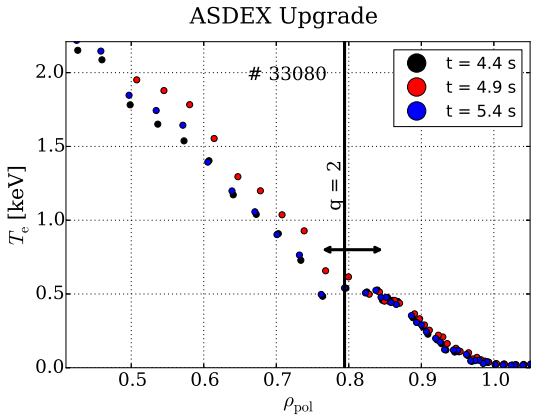

Figure 4.28: Electron temperature profiles from ECE measurements. The arrow marks the width of the flattening of the temperature profile around the q = 2 surface marked with a vertical black line at $\rho_{\text{pol}} \approx 0.8$.

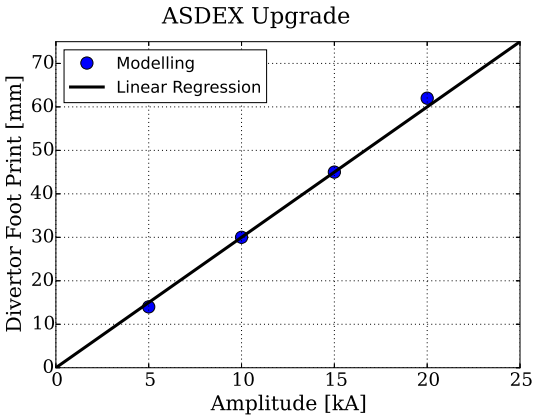

Figure 4.29: Extent of the divertor foot print of the connection length for different perturbation amplitudes $\hat{I}$ at the q = 2 surface.

flattened around the $q=2$ surface and marked with an arrow. The profile is similar for the time points $t=4.4$ and 5.4 s, being 1.0 s apart from each other, interpreted as the locking of this mode to the external magnetic perturbation rotated at 1 Hz. The profile at $t=4.9$ s shows no flattening which is interpreted as the X-point of the mode.
The calculated effect on field lines intersecting the divertor target is shown in figure 4.30 for two different current amplitudes on this surface. Note, no additional external magnetic perturbation is applied for this comparison. The divertor connection length foot print is similar for internal and external magnetic perturbation, with the extent being about the same for an external magnetic perturbation with $I_{\text{coil}} = 1$ kA and an internal mode with

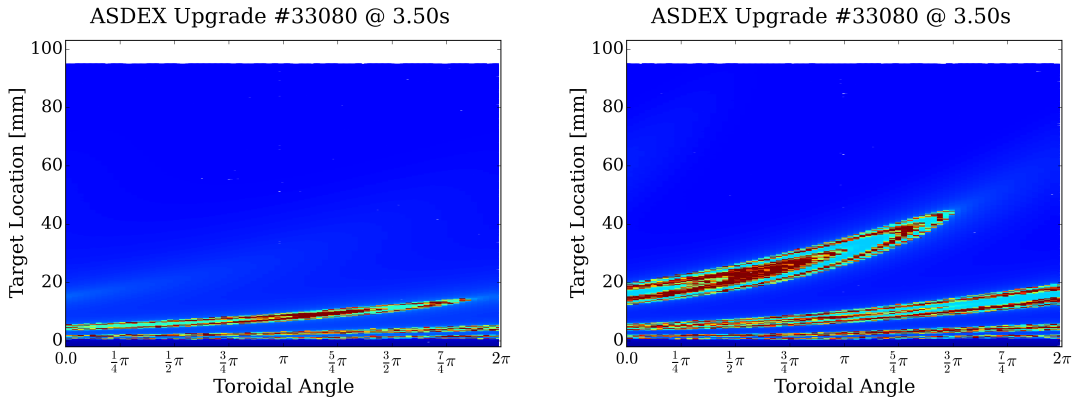

(a) $\hat{I} = 5\,\mathrm{kA}$ (b) $\hat{I} = 15\,\mathrm{kA}$

Figure 4.30: Connection length profile at the divertor target for two different perturbation amplitudes $\hat{I}$ at the q = 2 surface.

$\hat{I} = 15\,\mathrm{kA}$ at the q = 2 surface.
The characteristic extent of the foot print, the largest target location s of the well defined boundary, along the divertor target for different $\hat{I}$ is presented in figure 4.29. Increasing the internal perturbation amplitude $\hat{I}$ linearly increases the divertor foot print $\Delta s_{\mathrm{internal}}$.

$$\Delta s_{\mathrm{internal}}[\mathrm{mm}] = 3 \cdot \hat{I}[\mathrm{kA}] \tag{4.2}$$

Thus, it is possible to estimate the current that is needed in order to explain the measured heat flux pattern having both an internal as well as an external magnetic perturbation simultaneous. Assuming that the external and internal magnetic perturbation are in phase[4] and using a linear superposition[5] the foot print extent can be expressed as

$$\Delta s_{\mathrm{IR}} = \Delta s_{\mathrm{MP}} + \Delta s_{\mathrm{internal}}. \tag{4.3}$$

The visible extent from IR measurements is $\Delta s_{\mathrm{IR}} = 100\,\mathrm{mm}$. The foot print reaches up to $\Delta s_{\mathrm{MP}} = 40\,\mathrm{mm}$ from field line tracing using the external magnetic perturbation field. Thus, $\Delta s_{\mathrm{internal}} = 60\,\mathrm{mm}$ is deduced. Using the linear regression presented in equation (4.2), a current of $\hat{I} = 20\,\mathrm{kA}$ is needed at the $q = 2$ surface.

[4]The internal mode locks to the external magnetic perturbation field and is a *resonant* effect.
[5]This is the vacuum field approximation as used in section 3.2 for the external magnetic perturbation.

4.5 Experimental Results in H-Mode

Applying an external magnetic perturbation is studied as a tool to control ELMs that occur in H-Mode operation. The heat flux is divided into two periods in H-Mode plasmas, heat flux associated with ELM crashes and inter-ELM, *steady state*, heat flux. Two aspects of ELM associated heat flux are discussed, the peak ELM energy fluence (section 4.5.1) and the position where filaments impinge (section 4.5.2).
The peak ELM energy fluence is one of the major concerns related to ELMs due to the possible reduced divertor lifetime if the energy fluence exceeds material limits, making it the primary objective for active ELM control by applying an external magnetic perturbation.
ELM filaments may carry highly energetic ions from the pedestal region towards the divertor and first wall. Temporal or spatial variations in the applied magnetic perturbation might be needed in ITER to prevent enhanced sputtering at distinguished positions if the ELM filaments lock to the external magnetic perturbation.
In section 4.5.3 inter-ELM heat flux is compared to modelling results as well as to L-Mode heat flux discussed in previous section.
Due to the edge pressure gradient, forming the H-Mode pedestal, and the associated bootstrap current, plasma response is thought to be more important compared to L-Mode [Liu et al., 2016, Ryan et al., 2017]. This is confirmed by experiments showing that the largest density pump-out occurs not at the vacuum field *resonant* differential phase but at the largest calculated plasma response [Kirk et al., 2015, Willensdorfer et al., 2016, Suttrop et al., 2017].

4.5.1 Influence of the Magnetic Perturbation on the ELM Energy Fluence

A recent scaling and model has been established for ASDEX Upgrade, JET and MAST for the ELM peak energy fluence with the main parameter being pressure at the top of the pedestal [Eich et al., 2017] (see section 2.1.2). Type-I ELMs during phases with magnetic perturbation follow this scaling at ASDEX Upgrade [Sieglin et al., 2017]. The application of a magnetic perturbation can lead to a reduction in density, the so called *density pump-out*, and with this a reduction in pedestal pressure. The measured ELM energy fluence for discharges with and without density pump-out are compared to the model prediction in figure 4.31. As discussed in [Sieglin et al., 2017], measured ELM

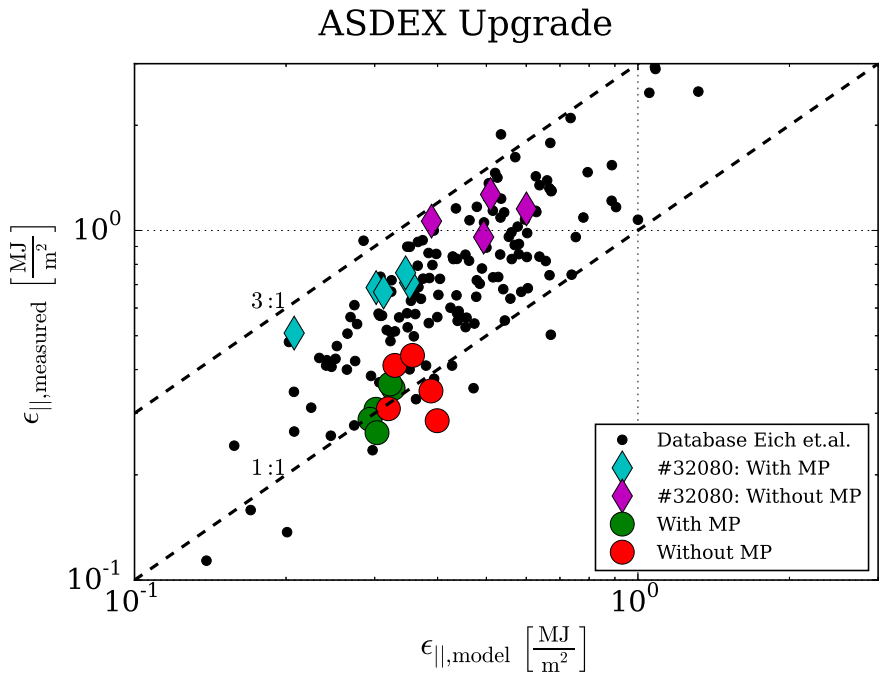

Figure 4.31: Measured parallel ELM energy fluence depending on the model prediction (equation (2.33)). Shown is a selection of the database published in [Eich et al., 2017] in black, a discharge with density pump-out (# 32080) presented in [Sieglin et al., 2017] (diamonds) and discharges without substantial density pump-out and various *differential phase*s (red and green dots).

energy fluence during phases with magnetic perturbation and density pump-out (# 32080, diamonds) are reduced, however, still described by the model due to the reduced pedestal pressure. For discharges without density pump-out (red and green dots), but still visible effects on the inter-ELM profiles, no change in the measured as well as predicted ELM energy fluence is found.

4.5.2 Influence of the Magnetic Perturbation on the ELM Filament Foot Print

The application of an external magnetic perturbation leads to a 2D heat flux distribution in L-Mode and inter-ELM due to the breaking of the axisymmetry. In figure 4.32 the time trace of heat flux at the outer divertor target measured with IR thermography is shown for # 33222 with vacuum field *resonant* magnetic perturbation. The phase with magnetic

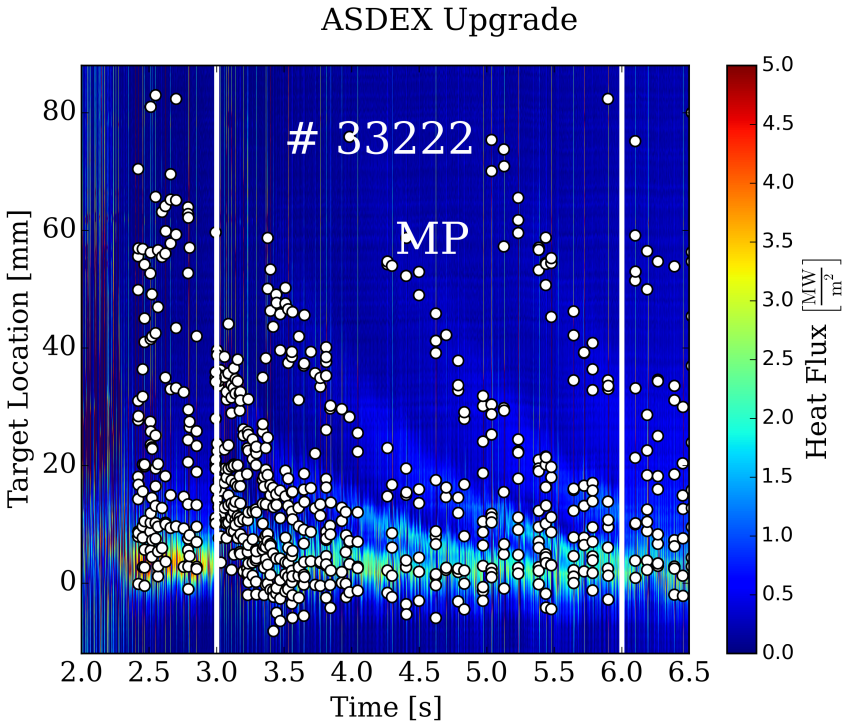

Figure 4.32: Measured H-Mode heat flux time trace with superimposed ELM filament location (white dots). The phase with MP is between 3.0-6.0 s (vertical white lines).

perturbation (3.0 - 6.0 s) is marked with vertical white lines. The ELM filament position for individual ELMs is depicted with white dots. The position is manually marked in the ELM peak heat flux time points from the IR measurement and taken to be the position with a clear deviation from an exponential fall-off in the scrape-off layer. Before and after the phase with magnetic perturbation the position is stochastic. During the phase with a magnetic perturbation the position of filaments coincides with the position of elevated inter-ELM heat flux. For small ELMs, not being type-I, this locking is routinely observed. For the presented discharges with type-I ELMs in this thesis the locking is not observed uniformly in discharges with similar plasma and magnetic perturbation field parameters. Further investigations are needed to understand the conditions leading to the locking of type-I ELMs.

4.5.3 Influence of the Magnetic Perturbation on the Inter-ELM Heat Flux Pattern

The inter-ELM target heat flux pattern without magnetic perturbation is characterized with the same transport model as the L-Mode heat flux profile. However, in H-Mode significantly more power is deposited at the divertor target and in general a smaller λ_q is observed.
In figure 4.33 and figure 4.34 a comparison between the inter-ELM heat flux pattern from experimental measurements (left) and modelling (right) is shown for discharges with a vacuum field *resonant* and *non-resonant* magnetic perturbation, respectively. The presented inter-ELM heat flux consists of time slices, averaged in the period between 75-90 % between consecutive ELMs and normalized to the deposited power.
Although plasma response is neglected in this comparison, the vacuum field *resonant* configuration exhibits a larger variation compared to the *non-resonant* configuration in both measurement as well as modelling. The power fall-off length assumed for modelling is $\lambda_q = 2.0\,\mathrm{mm}$, consistent with the value obtained using the H-Mode scaling law for ASDEX Upgrade and JET (see equation (2.22) on page 14). The modelled and measured profile

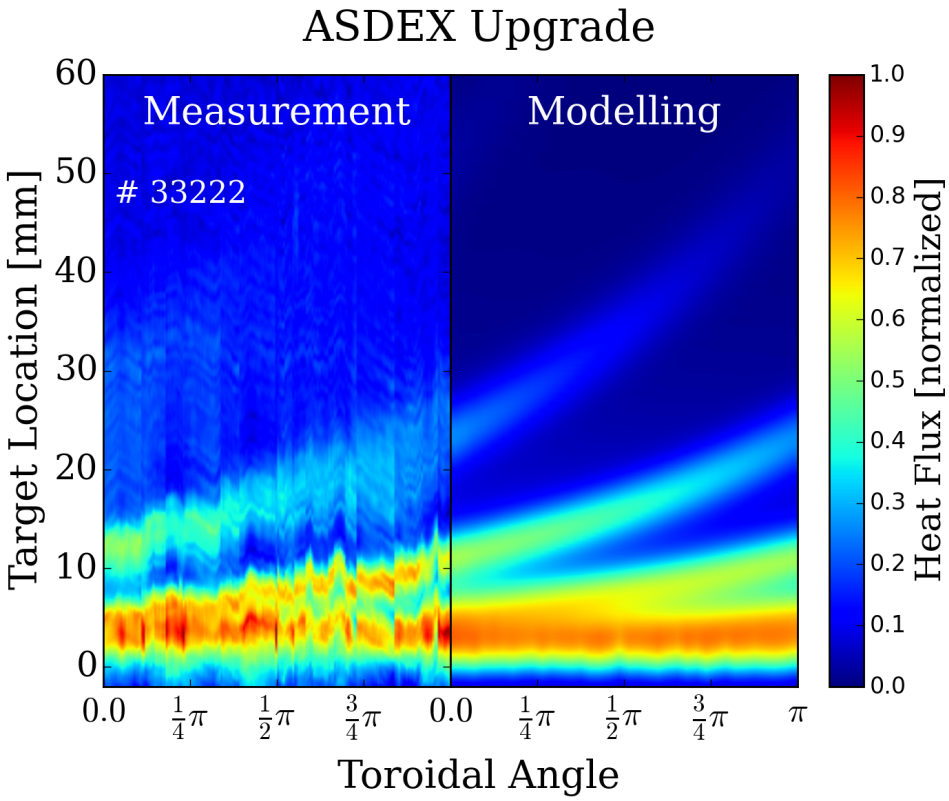

Figure 4.33: 2D heat flux profiles obtained by IR measurements (left) and modelling (right) for # 33222 with a *resonant* external magnetic perturbation.

for the *resonant* configuration are in agreement. The modelled profile for the *non-resonant* configuration shows a significant larger variation compared to the measurement. This is also observed in the L-Mode comparison.
Due to the high ELM frequency and diagnostic limitations in frame rate and imperfections in the correction of vibrations of the optical path excited by ELMs, the heat flux is normalized for each inter-ELM period. No meaningful toroidal averaged profile can be calculated from the measured heat flux.
A comparison between vacuum field modelling and measured heat flux pattern for an ELM suppressed discharge is shown in figure 4.35. Although an amplification of the external magnetic perturbation due to plasma response is thought to be important for the ELM suppression in this discharge [Suttrop et al., 2017], the divertor heat flux is described by modelling using the vacuum field approximation. Due to imperfections in the correction of vibrations of the optical path the measured heat flux exhibits significant noise making this comparison only qualitative.

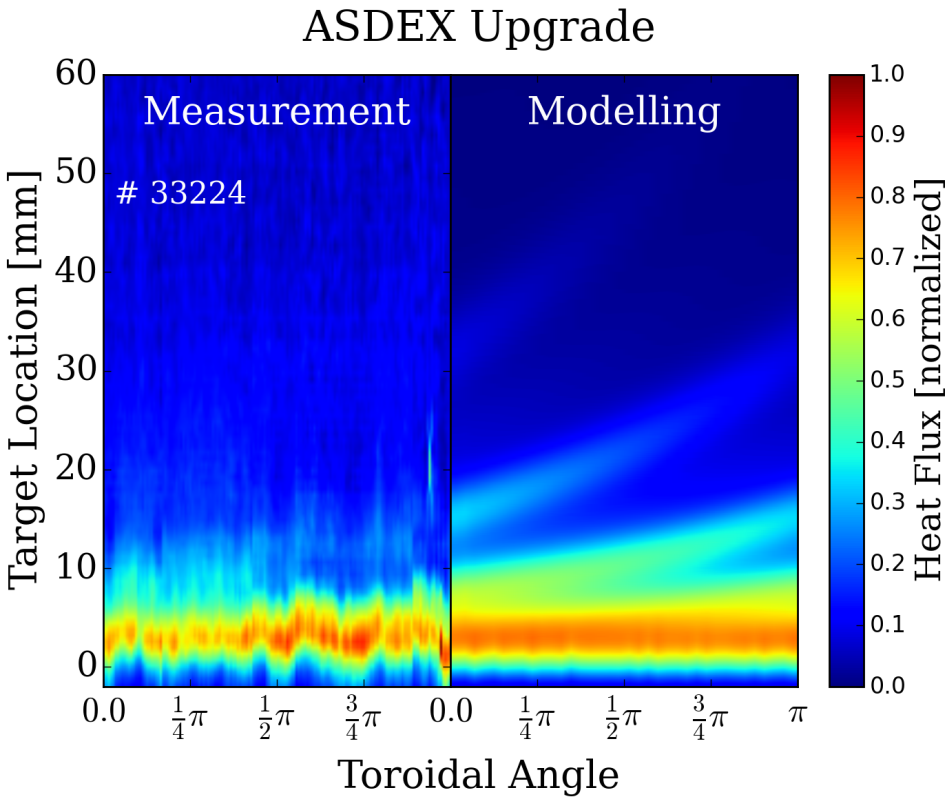

Figure 4.34: 2D heat flux profiles obtained by IR measurements (left) and modelling (right) for # 33224 with a *non-resonant* external magnetic perturbation.

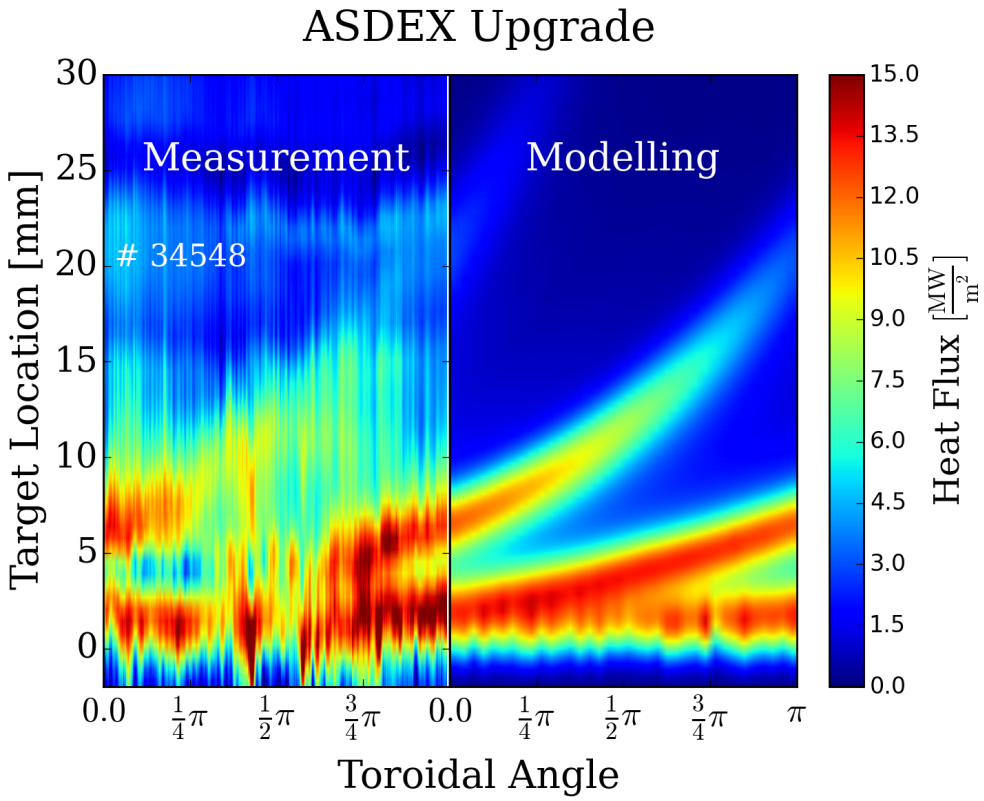

Figure 4.35: 2D heat flux pattern for an ELM suppressed H-Mode, # 34548.

4.5.3.1 Comparison to the L-Mode Heat Flux Pattern

In figure 4.36 a comparison between L-Mode and H-Mode discharges is presented, both with the external magnetic perturbation being vacuum field *resonant*. In H-Mode the extent of significant heat flux along the target location is reduced compared to L-Mode due to a narrower power fall-off length λ_q, which is reproduced in modelled heat flux with $\lambda_q^{L-Mode} = 3.5\,mm$ and $\lambda_q^{H-Mode} = 2.0\,mm$ used in the model. No limitation of the used vacuum field approximation is observable.
The effect of decreasing *toroidal peaking* with an increasing divertor broadening, discussed in section 4.3 for L-Mode, holds for H-Mode as well assuming that transport in the divertor volume is unaffected by the confinement regime. The increase of the *toroidal peaking* with perturbation strength as well as the decrease with increasing toroidal mode number, discussed in section 4.2 for modelling in L-Mode, can be transferred to modelling in H-Mode as well.
Overall, the data quality of H-Mode inter-ELM heat flux measurements limits the comparison between L- and H-Mode as well as the comparison to the model. Especially a comparison between toroidally averaged heat flux in presence of a magnetic perturbation and without magnetic perturbation is not possible in the measured heat flux for the presented H-Mode discharges.

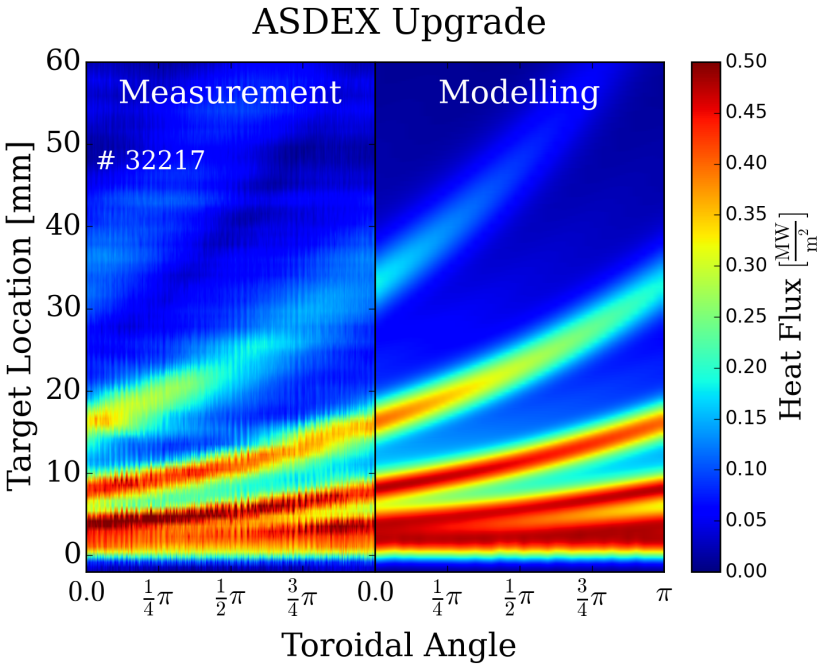

(a) L-Mode

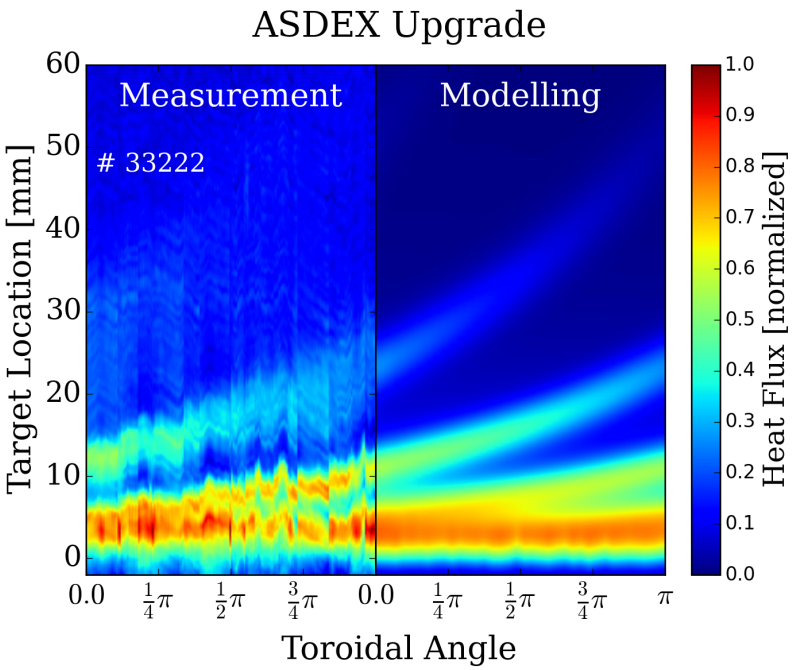

(b) H-Mode

Figure 4.36: 2D heat flux profiles obtained by IR measurements and modelling for both L-Mode and H-Mode.

Chapter 5

Triangularity Dependence of Scrape-Off Layer Heat Transport in TCV

Increased energy confinement with negative triangularity in low [Pochelon et al., 1999] and medium [Moret et al., 1997] density L-Mode plasmas has been reported. Due to the increased confinement, recent reactor studies investigate negative triangularity reactor designs [Kikuchi et al., 2014, Medvedev et al., 2015, Sauter, 2016]. These studies use empirical scaling laws for the scrape-off layer power fall-off length to estimate the divertor heat flux density. However, these scaling laws are conducted with positive triangularity and without dedicated scans of the triangularity.

TCV offers a unique plasma shaping capability. The presented study focuses on experimental observations with a scan in upper triangularity δ_{up}, including negative triangularity, focusing on the power fall-off length λ_{q} in L-Mode[1].

The discharge parameter for the presented study are discussed in section 5.1 focusing on changes of plasma parameter with varying δ_{up}. In section 5.2 target heat flux is characterized for both divertor targets and correlations with changes of plasma parameter are presented. The experimental results are discussed in section 5.3. Comparisons to available empirical scaling laws, a prediction for the asymmetry between inner and outer λ_{q} from a heuristic drift-based model and recent turbulence simulations are presented.

[1]This chapter is submitted for publication [Faitsch et al., 2017a].

5.1 Upstream and Target Conditions as Function of Upper Triangularity

The database used for this study consists of ohmically heated L-Mode discharges, in deuterium (D) and helium (He) in standard lower single null divertor configuration. For each main ion species, discharges with both toroidal field directions were performed. A negative (positive) toroidal field corresponds to the downwards (upwards) ion drift direction and will be referred to as favourable (non-favourable) drift direction towards (away from) the X-point, *fav* (*non*)[2]. The direction of plasma current is changed together with the magnetic field direction to keep plasma helicity. The range of global plasma parameters is shown in table 5.1. Absolute values of plasma current and toroidal magnetic field are 240 kA and

Table 5.1: Discharge Parameters of the database.

Ion	Drift	$\mathbf{B}_{\mathrm{tor}}$ [T]	$\mathbf{I}_{\mathrm{p}}$ [kA]	$\mathbf{n}_{\mathrm{e,avg}}$ [$10^{19}\,\mathrm{m}^{-3}$]	P_{SOL} [kW]	$\mathbf{q}_{95}$	κ	δ_{up}
D	fav.	-1.43	-240	4.1 to 6.2	170 to 230	2.5 to 3.2	1.3 to 1.5	-0.26 to +0.45
D	non	1.43	240	4.4 to 7.0	160 to 200	2.5 to 3.3	1.3 to 1.5	-0.28 to +0.46
He	fav.	-1.43	-240	4.5 to 7.7	200 to 230	2.6 to 3.1	1.3 to 1.5	-0.25 to +0.47
He	non	1.43	240	5.4 to 6.5	180 to 200	2.8 to 3.5	1.3 to 1.5	-0.26 to +0.60

1.43 T, respectively. Plasma shape for both species is altered by scanning upper triangularity δ_{up} between -0.28 and +0.47 (+0.60 for helium and non-favourable drift direction). The plasma separatrix given by the magnetic equilibrium reconstruction code LIUQE [Hofmann and Tonetti, 1988] together with profiles of field line length in the scrape-off layer from the outer mid-plane to each target for four discharges are shown in figure 5.1. The lower part of the magnetic configuration is not changed, keeping the divertor geometry fixed. While the field line length between outer mid-plane and outer target is not changing during the δ_{up} scan, the field line length to the inner target varies mainly because of the decreasing distance, mapped to the outer mid-plane, between the active (lower) and non-active (upper) X-points. The vertical lines in figure 5.1(b) and figure 5.1(c) mark the position ($R - R_{\mathrm{sep}} = 5\,\mathrm{mm}$) at which the field line length L_{OMP} is taken in further discussions. L_{OMP} is taken 5 mm away from the separatrix in the scrape-off layer where the length does not change significantly anymore with increasing distance [Maurizio et al., 2017], except for discharges with the secondary X-point at a poloidal flux surface close to the separatrix. This choice is further motivated by the smallest power fall-off length $\lambda_{\mathrm{q}}^{\mathrm{out}} \approx 5\,\mathrm{mm}$ measured at the outer divertor target within this database. The outer mid-plane at TCV is defined as the outermost point of the separatrix w.r.t. major radius R.
The elongation κ at the normalized poloidal flux surface $\rho_{\mathrm{pol}} = 0.95$ is around 1.4 with a variation between 1.28 and 1.53 with smaller average κ for $\delta_{\mathrm{up}} < 0$ (figure 5.2(a)). The

[2]This typically refers to the lower H-Mode power threshold. In this chapter L-Mode plasmas are discussed and the expressions favourable and non-favourable are a choice of convenience to be consistent with other studies.

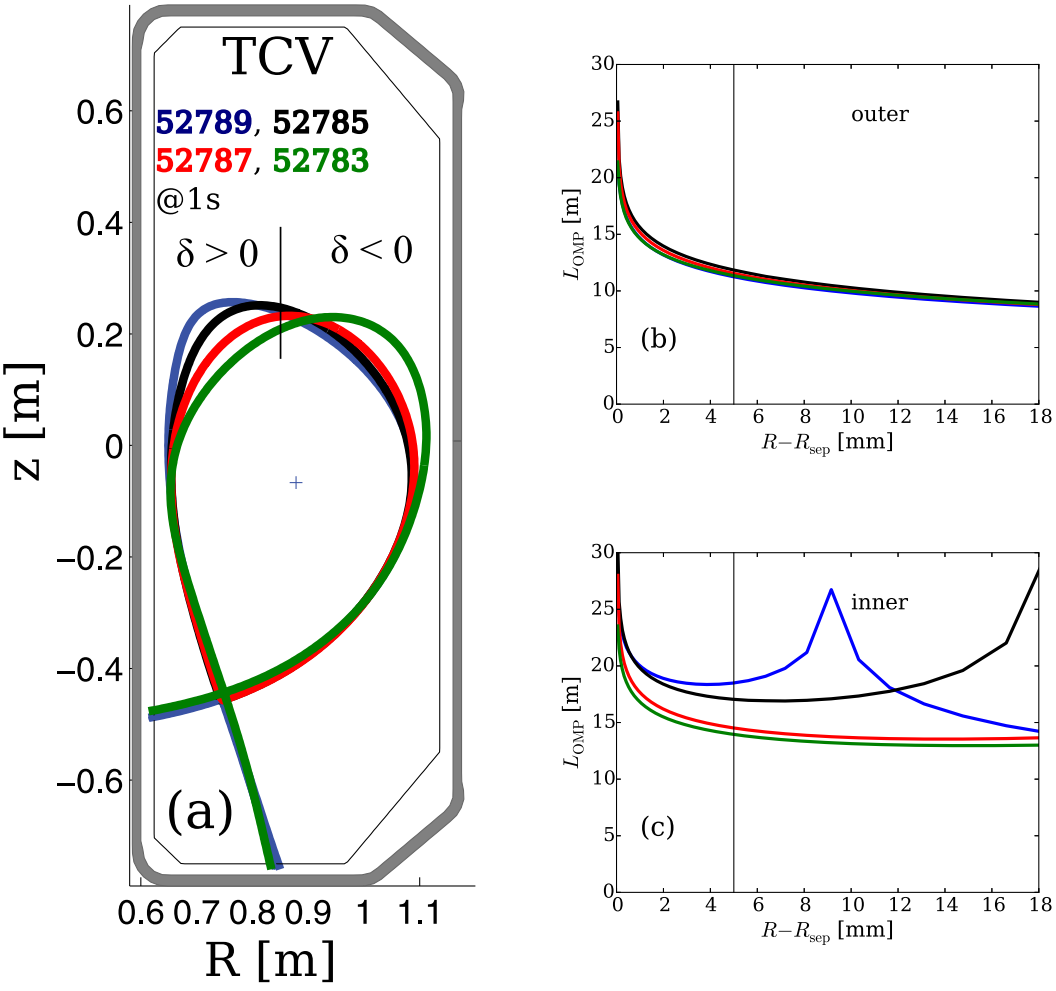

Figure 5.1: (a) Poloidal cross-section and radial profiles of field line length L_{OMP} to (b) outer and (c) inner target at the outer mid-plane for four different upper triangularities.

database for deuterium contains additional discharges with lower κ. The edge safety factor q_{95} varies between 2.5 and 3.5 correlated with δ_{up}, figure 5.2(b). Plasma density is kept constant during discharges but varies between discharges. The density is kept low enough to be fully attached (peak target electron temperature above 10 eV) but high enough to avoid strong MHD activity. The line averaged electron density $n_{\mathrm{e,avg}}$ lies between $4\text{-}8 \cdot 10^{19}\,\mathrm{m}^{-3}$ with on average larger values for helium plasmas compared to deuterium (figure 5.3(c)).
The power crossing the separatrix P_{SOL} is estimated by subtracting the radiated power in the confined region $P_{\mathrm{rad,main}}$, deduced from tomographic inversion of bolometry [Sheikh et al., 2016], from the ohmic power P_{ohm}, deduced from the equilibrium reconstruction code LIUQE [Hofmann and Tonetti, 1988]. P_{SOL} is in the range of $200 \pm 50\,\mathrm{kW}$ for all discharges in this database without correlation to δ_{up}.
Edge electron temperature $T_{\mathrm{e,edge}}$ is measured using a Thomson scattering system [Franke,

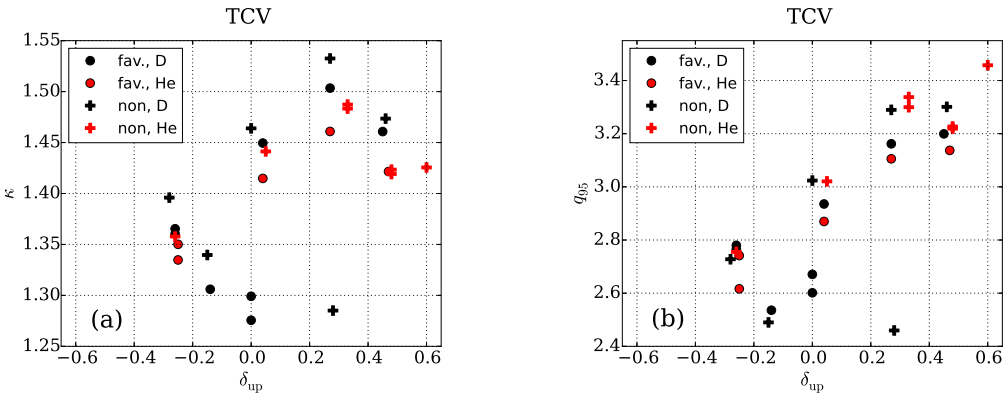

Figure 5.2: Correlation of upper triangularity δ_{up} with (a) elongation κ and (b) edge safety factor q_{95}.

1997]. The value at $\rho_{pol} = 0.95$ is chosen as representation of the edge electron temperature of an L-Mode plasma, deduced from a linear fit to the plasma edge profiles within a time period of 200 ms with constant plasma parameters [Sauter et al., 2014].
A clear correlation between $T_{e,edge}$ and δ_{up} is shown in figure 5.3, which is independent of main ion species. However, the non-favourable drift direction exhibits higher $T_{e,edge}$ at similar δ_{up}. Since, as mentioned before, P_{SOL} does not change in the database, the dependence of $T_{e,edge}$ on δ_{up} may indicate that the energy transport of the plasma decreases with decreasing (or negative) triangularity, consistent with previous studies [Moret et al., 1997, Pochelon et al., 1999, Marinoni et al., 2009]. The stored energy W_{MHD} increases for decreasing triangularity, too. The variation at fixed δ_{up} is mainly due to the plasma density, varying about a factor of two between individual discharges (figure 5.3(c)). The

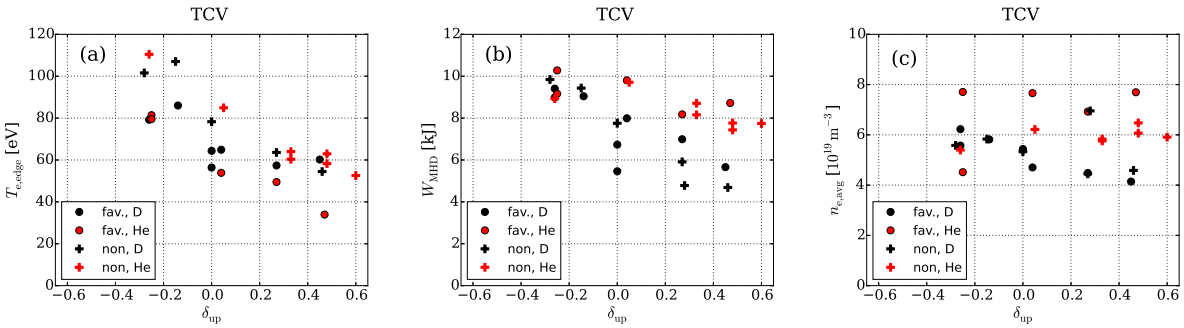

Figure 5.3: Correlation between upper triangularity δ_{up} and (a) edge electron temperature $T_{e,edge}$, (b) stored energy W_{MHD} and (c) line averaged density $n_{e,avg}$.

variation in δ_{up} changes q_{95} and correspondingly the field line length in the scrape-off layer. Field line length L^{in}_{OMP} to the inner target (figure 5.4(a)) exhibits a pronounced change of more than 60 % with changing δ_{up} as already noted in the discussion of figure 5.1(c). The

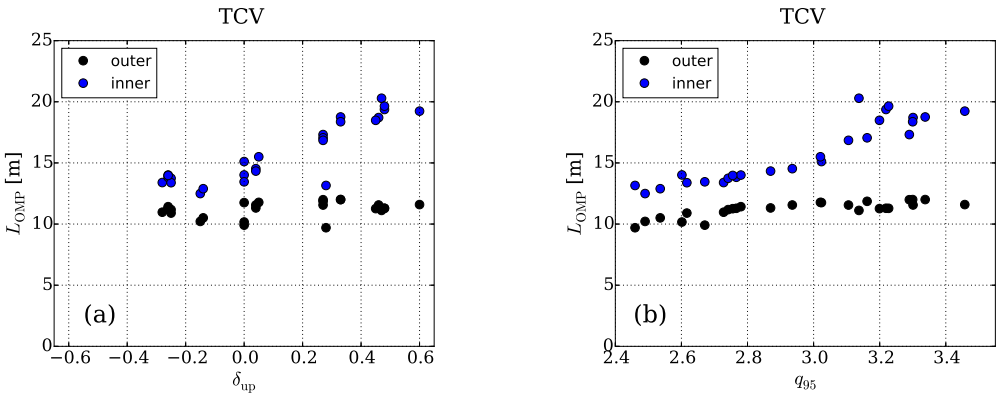

Figure 5.4: Field line length L_{OMP} from 5 mm outside the outermost point of the separatrix to both divertor targets versus (a) upper triangularity δ_{up} and (b) edge safety factor q_{95}.

effect is small (less than 25 %) for L^{out}_{OMP}. This change is correlated with the change in q_{95}, shown with comparing both L^{in}_{OMP} and L^{out}_{OMP} to q_{95} in figure 5.4(b).
The temperature evolution of both strike zones is measured using two IR thermography systems, described in section 3.1.2. Target electron temperature $T_{e,tgt}$ and density $n_{e,tgt}$ are estimated using Langmuir probes [Pitts et al., 2003].
A power balance between P_{ohm} and sum of total radiated power from bolometry, $P_{rad,tot}$, and power to inner and outer divertor target plate, P_{in} and P_{out}, calculated from profiles measured with the IR system, is shown in figure 5.5(c) depending on δ_{up}. The power bal-

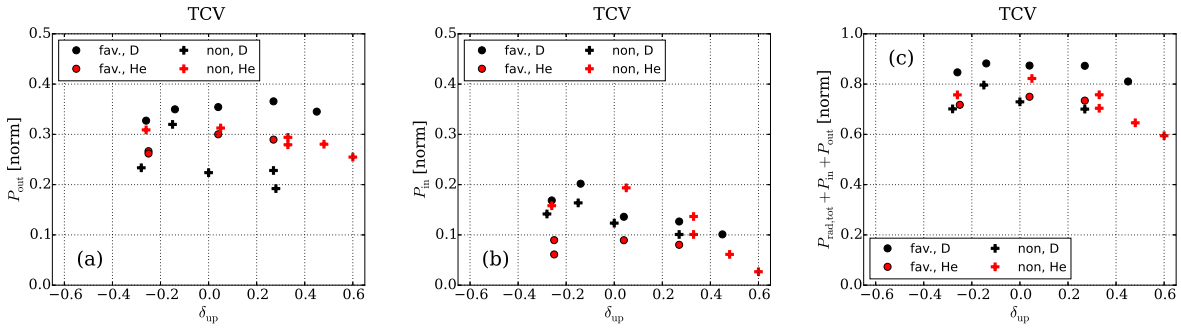

Figure 5.5: Correlation between upper triangularity δ_{up} and power to (a) outer P_{out} and (b) inner P_{in} divertor target and (c) power balance. The power is normalized to the ohmic heating power.

ance is in the range of 70-90 % except for the highest positive δ_{up} cases for which, being very close to double null, part of the power is deposited at non-monitored areas.
The power on outer and inner target is shown in figures 5.5(a) and (b) with no clear correlation with δ_{up}. It is seen that more power flows to the outer target, which is in line with previous studies [Eich et al., 2005, Pitts et al., 2005, Maurizio et al., 2017].

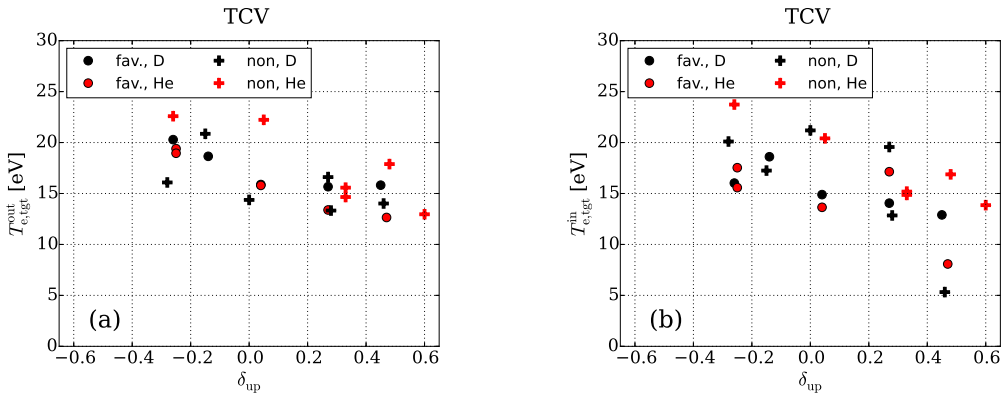

Figure 5.6: Correlation between upper triangularity δ_{up} and target electron temperature for (a) outer $T^{\mathrm{out}}_{\mathrm{e,tgt}}$ and (b) inner $T^{\mathrm{in}}_{\mathrm{e,tgt}}$ target.

In figure 5.6 peak target electron temperature for both outer, $T^{\mathrm{out}}_{\mathrm{e,tgt}}$, and inner, $T^{\mathrm{in}}_{\mathrm{e,tgt}}$, target is shown. Only heat flux profiles for peak temperatures above 10 eV are used for the database, assuring attached conditions. For this reason data for the inner target are excluded from two discharges since there $T^{\mathrm{in}}_{\mathrm{e,tgt}} < 10\,\mathrm{eV}$.

5.2 Divertor Target Heat Flux Characterization

Typical heat flux profiles for inner and outer divertor targets are shown in figure 5.7. The solid line represents a fit using the 1D diffusive model (equation (2.17) on page 13) and corresponding values for λ_{q} and S are presented.

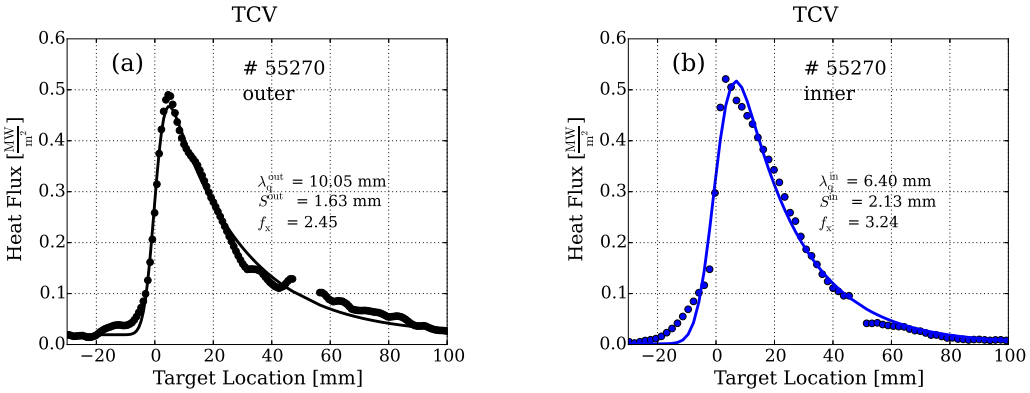

Figure 5.7: IR target profiles for # 55270 (He, non-favourable, $\delta_{\mathrm{up}} = 0$) together with a fit using the 1D diffusive model (equation (2.17)) for (a) outer and (b) inner target.

The values for λ_q in this chapter are calculated using the method described in [Maurizio et al., 2017]: The heat flux profile is mapped onto flux labels, converted into real space coordinates of the outer mid-plane. They are fitted afterwards, directly obtaining (upstream) λ_q. This is done because the flux expansion may vary strongly at TCV with the possibility of using advanced divertor configurations. In order to distinguish values measured at outer and inner target the notation λ_q^{out} and λ_q^{in} is used in the following. This is adapted when comparing to previous results, typically using λ_q for the value measured at the outer target. The profiles for both targets are mapped to the outer mid-plane to have a common reference point. Single heat flux profiles are fitted for every 5 ms and the values averaged over typically 200 ms (40 profiles) for each discharge. Asymmetries for λ_q have been reported in previous studies at e.g. ASDEX Upgrade [Eich et al., 2005, Faitsch et al., 2015, Sieglin et al., 2016b], JET [Pitts et al., 2005] and TCV [Maurizio et al., 2017] and are discussed separately.
Figure 5.8 shows the correlation between δ_{up} and (a) λ_q^{out} and (b) λ_q^{in}. The values for λ_q^{out} monotonically increase with increasing δ_{up}. The values for λ_q^{in} do not show a monotonic behaviour with δ_{up}. For $\delta_{up} < 0$ the values for λ_q^{in} increases and for $\delta_{up} > 0$ they decrease, having a maximum value around $\delta_{up} \approx 0$.
Figure 5.9 shows λ_q^{in} and λ_q^{out} depending on δ_{up} for deuterium and favourable drift direction. They appear to diverge for $\delta_{up} > 0$ and behave mostly indifferent for $\delta_{up} < 0$.

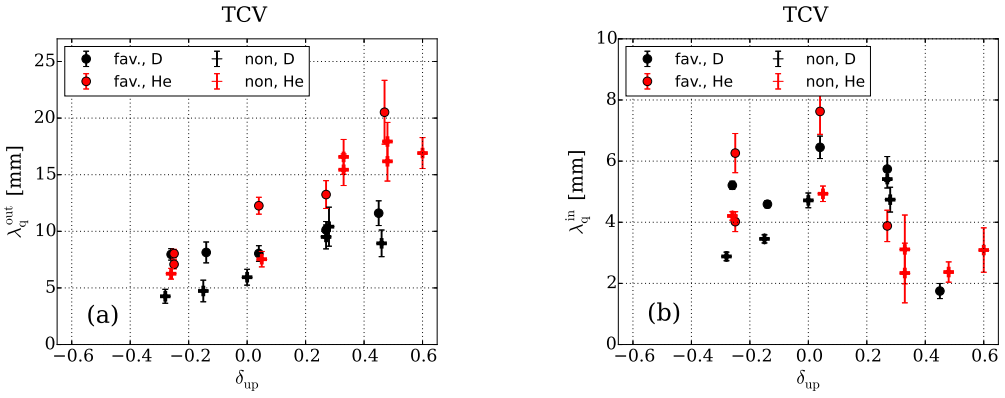

Figure 5.8: Correlation between upper triangularity δ_{up} and power all-of length for the (a) outer and (b) inner target.

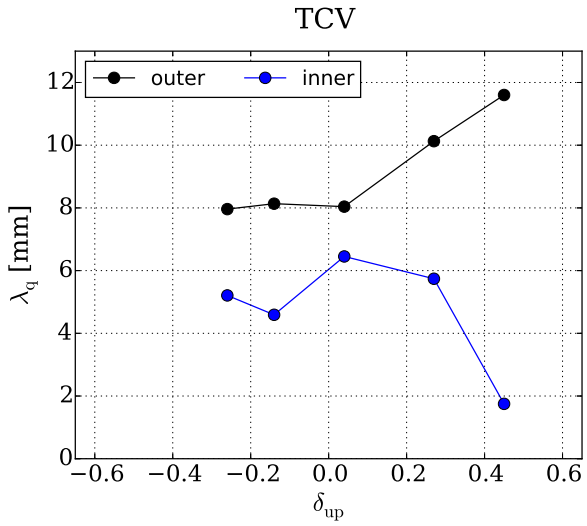

Figure 5.9: Correlation between upper triangularity δ_{up} and power fall-off length λ_q on both divertor targets for discharges in deuterium and favourable drift direction.

5.2.1 Further Correlations of the Power Fall-Off Length

Magnetic drift direction

The drift direction does not display notable influence on λ_q^{out} and λ_q^{in} for the presented database.

Edge safety factor

Dedicated discharges with lower κ are performed to vary q_{95} independently of δ_{up}, presented in table 5.2. This is aiming at a distinction between the effect of δ_{up} and q_{95} on λ_q. The change of q_{95} at fixed δ_{up} does not affect λ_q^{out} outside of error bars. A change of δ_{up} at fixed q_{95} on the contrary leads to a change of λ_q^{out}. For λ_q^{in} no correlation outside the experimental uncertainty is found for this subset of discharges. Since no Thomson scattering data is available for discharge 52355, no discrimination is possible between q_{95} and δ_{up} for $T_{e,edge}$ effects in this data set.

Table 5.2: Discharge parameters for a selected subset of the database.

Shot number	δ_{up}	q_{95}	κ	λ_q^{out} [mm]	λ_q^{in} [mm]	$T_{e,edge}$ [eV]
52307	-0.15	2.49	1.34	4.7 ± 1.0	3.5 ± 0.2	107
52315	0.27	3.29	1.53	9.5 ± 1.0	5.4 ± 0.3	64
52355	0.28	2.46	1.29	10.4 ± 1.7	4.7 ± 0.4	-

Field line length

An increase of λ_q^{out} with increasing field line length L_{OMP}^{out} to the outer target by shifting the vertical position of the magnetic axis and hence increasing the distance between X-point and outer target has been reported [Gallo et al., 2016, Gallo et al., 2018, Maurizio et al., 2017]. Since L_{OMP}^{out} is fixed in the presented study, the variation of λ_q^{out} cannot be explained by a field line length variation.
The values for λ_q^{in} decrease for increasing L_{OMP}^{in}. Note, L_{OMP}^{in} in the database is altered by varying δ_{up} which does not affect L_{OMP}^{out}.

Main ion species

Helium shows on average larger values for λ_q^{out} compared to deuterium, in line with ASDEX Upgrade L-Mode [Sieglin et al., 2016a] and JET H-Mode [Fundamenski et al., 2011, Eich et al., 2011] observations. For λ_q^{in} no difference is observed outside experimental uncertainties.

Edge electron temperature

In figure 5.10 the dependence of λ_q^{out} and λ_q^{in} on $T_{e,edge}$ is shown. Both, λ_q^{out} and $T_{e,edge}$, are changing when δ_{up} is scanned. A larger λ_q^{out} is measured for lower $T_{e,edge}$. At low $T_{e,edge}$ a large variation in λ_q^{in} is observed, whereas at larger $T_{e,edge}$ λ_q^{in} decreases for increasing $T_{e,edge}$.

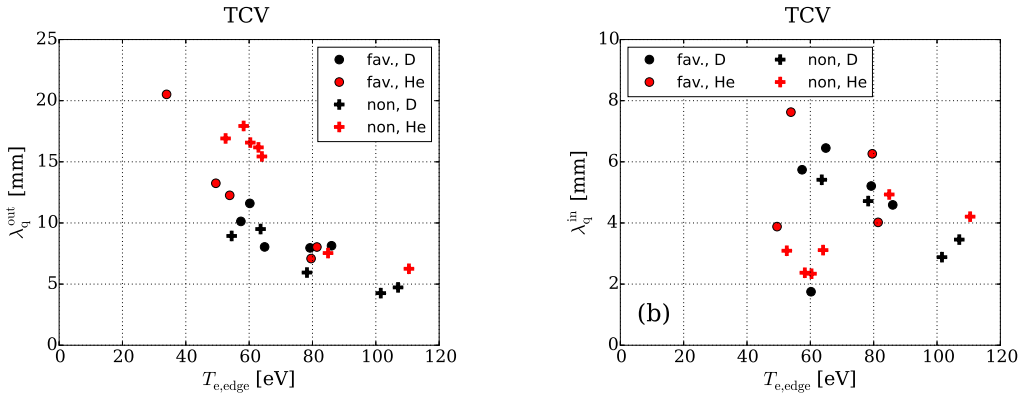

Figure 5.10: Correlation between edge electron temperature $T_{e,edge}$ and power fall-off length at the (a) outer and (b) inner target.

These findings will be discussed in light of different scaling laws and possible explanations for the observations are discussed in the following section.

5.3 Discussion

5.3.1 Comparison to Empirical Scaling Laws

In recent years multiple attempts have been made in order to scale λ_q^{out}. Empirical scaling laws in both L- and H-Mode are presented in section 2.1.1.3. The measured values of the presented database are compared to these scaling laws in this section.
A recent scaling law for λ_q^{out} in H-Mode based on a multi machine database (not including TCV) show that the poloidal magnetic field at the outer mid-plane B_{pol}^{OMP} is the main quantity determining λ_q^{out} [Eich et al., 2013].

$$\lambda_q^{Multi}[\text{mm}] = 0.63 \cdot B_{pol}^{OMP}[\text{T}]^{-1.19} \tag{5.1}$$

The database discussed in this chapter has a fixed plasma current and variations of B_{pol} due to the plasma shaping of less than 15%. No multi machine scaling for L-Mode exists up to now. However, a scaling law for JET and ASDEX Upgrade was presented by [Scarabosio et al., 2013]:

$$\lambda_q^{Scarabosio}[\text{mm}] = 1.44 \cdot B_{tor}[\text{T}]^{-0.80} \cdot q_{95}^{1.14} \cdot P_{SOL}[\text{MW}]^{0.22} \cdot R[\text{m}]^{-0.03} \tag{5.2}$$

Since for JET and ASDEX Upgrade the L-Mode λ_q^{out} is about twice that of the H-Mode scaling [Scarabosio et al., 2013, Faitsch et al., 2015, Sieglin et al., 2016b], a comparison of the database to the scaling law presented by [Eich et al., 2011] with an additional pre factor of 2 is done.

$$\lambda_q^{L-Mode,Eich}[\text{mm}] = 2 \cdot \lambda_q^{Eich}[\text{mm}] = 2 \cdot 0.73 \cdot B_{tor}[\text{T}]^{-0.78} \cdot q_{cyl}^{1.2} \cdot P_{SOL}[\text{MW}]^{0.1} \cdot R[\text{m}]^{0.02} \tag{5.3}$$

The measured values versus these scaling law predictions are shown in figure 5.11. All

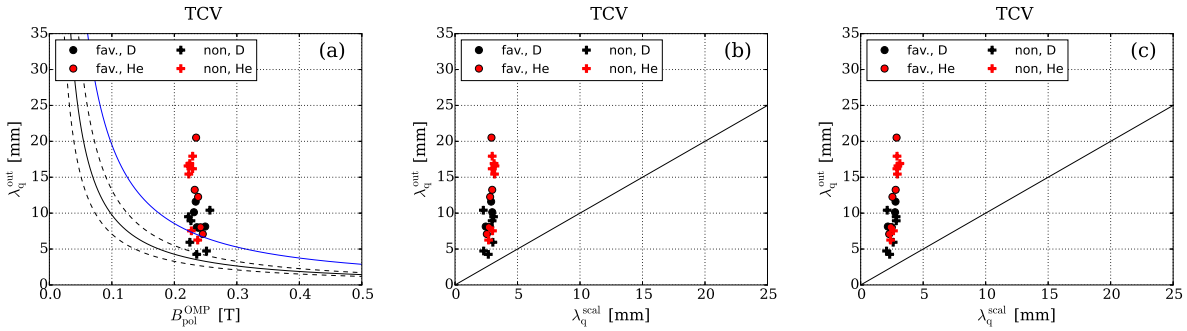

Figure 5.11: Comparison between measured λ_q^{out} and empirical scaling laws. (a) multi machine H-Mode scaling (equation (5.1)) (black) with typical database scatter of 25 % (dashed black) and 2 x scaling prediction (blue), (b) 2 x Eich H-Mode scaling (equation (5.3)) and (c) Scarabosio L-Mode scaling (equation (5.2)).

three scaling laws, using global discharge parameters, disagree in absolute magnitude as

well as in the increase of λ_q^{out} with increasing δ_{up}. Using an additional pre factor of 2 for the multi machine H-Mode scaling (equation (5.1)) as well, shown in figure 5.11(a) with a blue line, matches about the average value for deuterium. Note, that the databases used for this scaling laws do not contain dedicated triangularity scans.
A more recent study at ASDEX Upgrade by [Sieglin et al., 2016b] revealed that λ_q^{out} in L-Mode is dependent not only on B_{pol} but also on stored energy W_{MHD}, edge electron density $n_{e,edge}$ and main ion mass A (in atomic units u):

$$\lambda_q^{Sieglin}[\text{mm}] = 0.16 \cdot B_{pol}[\text{T}]^{-0.66} \cdot A[\text{u}]^{-0.15} \cdot \left(\frac{W_{MHD}[\text{MJ}]}{n_{e,edge}[10^{19}\text{m}^{-3}]} \right)^{-0.93} \tag{5.4}$$

The dependence on $W_{MHD}/n_{e,edge}$ is interpreted to be a dependence on $T_{e,edge}$ [Sieglin et al., 2016b].
A linear correlation between $W_{MHD}/n_{e,edge}/V$ and $T_{e,edge}$ is shown in figure 5.12 for the presented TCV database with V plasma volume.

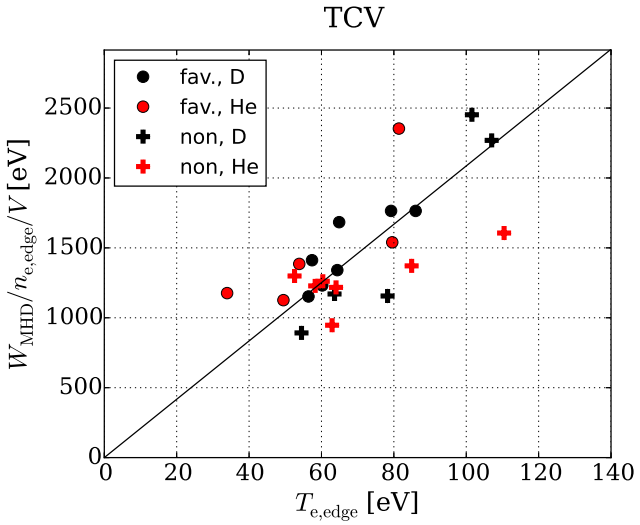

Figure 5.12: Correlation between edge electron temperature $T_{e,edge}$ and stored energy divided by edge electron density and plasma volume $W_{MHD}/n_{e,edge}/V$.

The plasma volume is not changing significantly for the presented database for TCV but is used to keep the same physical dimension and accounts for the size dependence of the stored energy.
The ASDEX Upgrade scaling is generalized by using $T_{e,edge}$ instead of $W_{MHD}/n_{e,edge}$. The pre factor is adapted for ASDEX Upgrade $T_{e,edge}$ at $\rho_{pol} = 0.95$.

$$\lambda_q[\text{mm}] = 163 \cdot B_{pol}[\text{T}]^{-0.66} \cdot A[\text{u}]^{-0.15} \cdot T_{e,edge}[\text{eV}]^{-0.93} \cdot \left(\frac{R}{R_{AUG}} \right)^{x} \tag{5.5}$$

The unknown major radius R dependence (R^x) due to the single machine scaling law is explicitly taken into account.

The exponent of the major radius R is found to be -0.03 in order to match the absolute values for deuterium with favourable drift direction in the presented TCV database using the same exponents otherwise.

$$\lambda_q^{\mathrm{L-Mode}}[\mathrm{mm}] = 165 \cdot B_{\mathrm{pol}}[\mathrm{T}]^{-0.66} \cdot A[\mathrm{u}]^{-0.15} \cdot T_{\mathrm{e,edge}}[\mathrm{eV}]^{-0.93} \cdot R[\mathrm{m}]^{-0.03} \tag{5.6}$$

The pre factor contains the value of $R_{\mathrm{AUG}}^{0.03}$.
A comparison between measured values for λ_q^{out} and the scaling law prediction (equation (5.6)) is shown in figure 5.13.

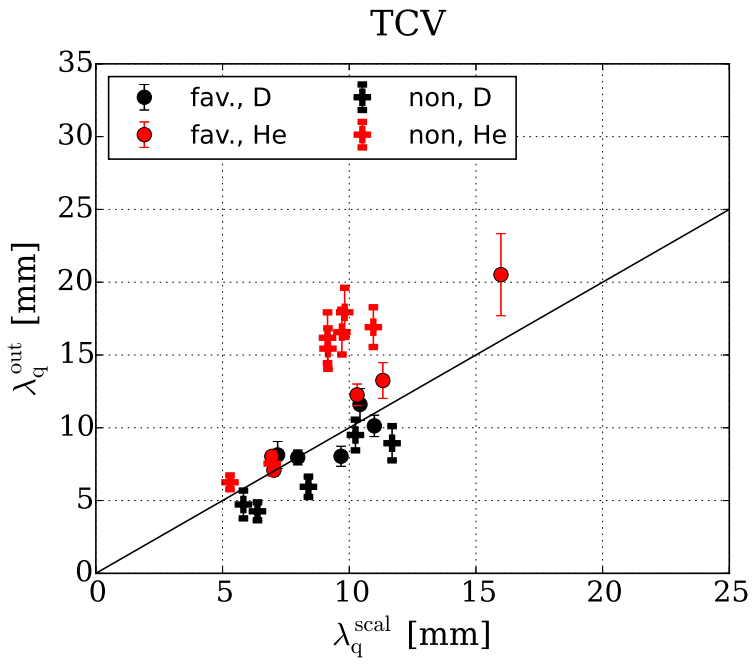

Figure 5.13: λ_q^{out} versus L-Mode scaling law (equation (5.6)).

Deuterium discharges with non-favourable drift direction are about 22 % lower than the scaling prediction. Helium discharges with favourable (non-favourable) drift direction are about 15 % (55 %) above the scaling predictions.
A scaling based uniquely on global machine parameters, e.g. B_{pol}, is not able to reproduce the variation of λ_q^{out} with the measured factor of four in this L-Mode TCV database. The $R^{-0.03}$ dependence is in line with multi machine regression results for H-Mode as well as the L-Mode scaling for JET and ASDEX Upgrade as discussed in section 2.1.1.3.
The ASDEX Upgrade database leading to the scaling law (equation (5.4)) contains discharges in deuterium and hydrogen in favourable drift direction [Sieglin et al., 2016b]. The 15 % larger values in helium and favourable drift direction in the presented TCV database is explained by a charge dependence of $Z[\mathrm{e}]^{0.20}$ in units of elementary charge e. The observed variations for reversed field direction hint toward additional dependencies.

5.3.2 Comparison to Turbulent Transport

The enhanced energy confinement with negative triangularity has been reported to be caused by reduced turbulent transport in the confined region [Pochelon et al., 2012, Camenen et al., 2007, Marinoni et al., 2009]. This is in line with the increased $T_{\mathrm{e,edge}}$ and W_{MHD} at constant heating power in the presented TCV database.
Recently, reduced turbulent transport has been reported for the scrape-off layer in elongated limited plasmas with negative triangularity using linear and nonlinear simulations [Riva et al., 2017]. This is in qualitative agreement with the observed decreasing $\lambda_{\mathrm{q}}^{\mathrm{out}}$ with decreasing δ_{up}. In the presented database only δ_{up} was changed and the lower part of the plasma was kept constant with a positive δ_{low}. A more detailed comparisons with these turbulence simulations are proposed to investigate the influence of δ_{up} on turbulence and its link to λ_{q} in diverted plasma configurations.
The experimental data does not allow to distinguish if the triangularity directly effects λ_{q} or indirectly by changing $T_{\mathrm{e,edge}}$ due to the correlation between δ_{up} and $T_{\mathrm{e,edge}}$. A direct triangularity effect is proposed by the discussed turbulence simulations. An indirect effect due to the change of $T_{\mathrm{e,edge}}$ is consistent with the L-Mode scaling law (equation (5.6)) presented in the previous section. In the ASDEX Upgrade database $T_{\mathrm{e,edge}}$ is changed with a scan in plasma density with fixed plasma shape [Sieglin et al., 2016b].

5.3.3 Implication for Reactor Studies

A negative triangularity reactor concept has been discussed in recent years, e.g. [Kikuchi et al., 2014, Medvedev et al., 2015, Sauter, 2016]. One of the key advantages in terms of power exhaust of such a device is the possibility of the divertor region being at a larger major radius R_{div} and with this having a larger toroidal divertor extent ($2\pi R_{\mathrm{div}} f_{\mathrm{tor}}$, with f_{tor} toroidal wetted fraction) for heat exhaust. We use the wetted area A as discussed in section 2.1.1.2:

$$A = 2\pi R_{\mathrm{div}} f_{\mathrm{tor}}\, \lambda_{\mathrm{int,tgt}}$$

with $\lambda_{\mathrm{int,tgt}}$ being the width of the profile at the divertor target. Using the 1D diffusive model, this width is

$$\lambda_{\mathrm{int,tgt}} = f_{\mathrm{x}} \left(\lambda_{\mathrm{q}} + 1.64S\right).$$

In the presented study the lower triangularity was kept constant in order to keep the divertor geometry fixed and R_{div} was unchanged. However, $\lambda_{\mathrm{q}}^{\mathrm{out}}$ decreased for decreasing δ_{up}. This counteracts the beneficial effect of negative triangularity leading to a larger R_{div} with decreasing δ_{low}. Additionally, a narrower scrape-off layer width decreases the capability to radiate power by impurity seeding in the scrape-off layer. The presented experiments, however, may not be fully representative for a plasma shape with both, negative upper and lower triangularity.

5.3.4 Comparison to Heuristic Drift-Based Model

A prominent edge heat transport model is the heuristic drift-based model by [Goldston, 2012]. This model predicts, independent of the actual value for the parallel flow velocity, a ratio of inner and outer power fall-off length λ_q of (equation (21) in [Faitsch et al., 2015], see derivation in appendix A):

$$\frac{\lambda_q^{in}}{\lambda_q^{out}} = \frac{1-\delta_x}{1+\delta_x} \tag{5.7}$$

were 'x' denotes upper or lower triangularity, dependent on the vertical drift direction of electrons or ions. Here, it is assumed that T_e at the outer and inner mid-plane separatrix position are equal as well as that the averaged parallel flow velocity is the same. Figure 5.14 shows the comparison between equation (5.7) and the ratio of the power fall-off lengths, using the upper triangularity. For positive δ_{up} the ratio decreases for increasing

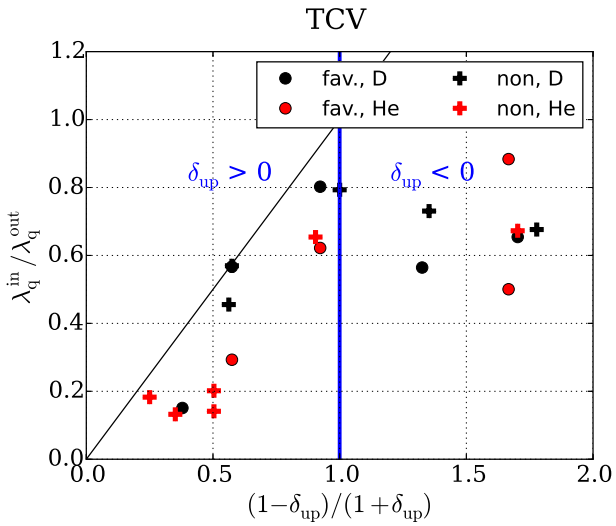

Figure 5.14: Ratio between inner and outer power fall-off length depending on the triangularity factor (equation (5.7)) using the upper triangularity δ_{up}.

δ_{up}, saturating at a value around 0.75 ± 0.15 for negative δ_{up}.
The data for $\delta_{up} > 0$ shows agreement to the prediction using δ_{up}. A drift-based model, as discussed here, predicts changes with the vertical drift direction. Using for both field direction either ion or electron drift direction in equation (5.7) results in diverse defining triangularity. This is in contrast to the measurement, the ratio between inner and outer λ_q shows no clear difference between the two field directions. For both field directions the ratio changes with the upper triangularity.
The saturation in the ratio for $\delta_{up} < 0$ in the experiment is in disagreement with the heuristic drift-based model prediction. From the model a linear decrease of λ_q^{out} is predicted for decreasing δ, in line with the measurement. A linear increase of λ_q^{in} is predicted

for decreasing δ, only observed for $\delta_{\mathrm{up}} > 0$. For $\delta_{\mathrm{up}} < 0$ the model predicts $\lambda_{\mathrm{q}}^{\mathrm{in}} > \lambda_{\mathrm{q}}^{\mathrm{out}}$, not observed in this experiment.

Chapter 6

Summary and Conclusions

In this thesis divertor power load is investigated in two medium sized tokamaks, ASDEX Upgrade and TCV. Power exhaust is a major challenge for future and larger machines towards a possible fusion plant for electricity production.
For the design and operation of future machines, the energy transport from the confined region into the scrape-off layer and along field lines towards the divertor target has to be known. In next step fusion devices, where actively cooled components have to be used due to the long pulse duration, steady state heat flux is limited to about 10 $\frac{\mathrm{MW}}{\mathrm{m}^2}$. Type-I ELMy H-Mode is a very attractive operational regime in e.g. ITER due to its good confinement properties and stationary density. ELMs help to control the impurity content in the plasma by flushing out impurities effectively. However, heat fluxes due to ELMs might limit the lifetime of the divertor target in such next step devices.
This thesis reports on two aspects of divertor power load. One is the change of divertor heat flux patterns when applying an external magnetic perturbation for both transient and steady state heat flux in ASDEX Upgrade. Applying a non-axisymmetric external magnetic perturbation is one technique that is studied in order to mitigate or suppress ELMs. The second aspect is changes in the scrape-off layer width and the dependence on plasma geometry in TCV to gain further insight into L-Mode scrape-off layer transport physics.
Applying an external magnetic perturbation leads to a major change in the divertor heat flux pattern. The inter-ELM and L-Mode pattern, being axisymmetric without magnetic perturbation, develop a 2D structure. This structure is reproduced for the investigated discharges in both L- and H-Mode with a simplified scrape-off layer model that was developed within this thesis, based on field line tracing using the vacuum field approximation. In the model a non-axisymmetric separatrix is defined using a constant connection length and the axisymmetric separatrix position as average value. The scrape-off layer power fall-off length is used as input and parallel heat flux is calculated using the two point model for each field line. Cross-field transport in the divertor region is simplified by convolving the target profile, resulting from the two point model, with a Gaussian, consistent with the 1D diffusive model.
The toroidally averaged experimental heat flux profile in L-Mode with magnetic perturbation is similar to the reference profile without magnetic perturbation, being characterized

by the same values for the transport qualifiers, power fall-off length λ_q and divertor broadening S. No change in the heat transport is observed, in line with the model prediction. The peak heat flux is unchanged for all toroidal phases with rotating magnetic perturbation. This is the same location as in the reference phase without magnetic perturbation. Although the toroidally averaged heat flux is unchanged, the application of the magnetic perturbation has an effect onto the toroidal variation of the heat flux. The *toroidal peaking* is largest for the *resonant* configuration and at lowest density with up to a factor of about 2. The variation decreases by shifting the *differential phase* away from the *resonant* configuration. For the *non-resonant* configuration no changes are observed outside typical heat flux variations in L-Mode. Increasing the density increases the divertor broadening S for the outer divertor of ASDEX Upgrade. This density increase leads to a reduced *toroidal peaking* and a nearly axisymmetric profile in attached divertor conditions for the discharge parameters obtained in the discussed L-Mode study. The reduction of the *toroidal peaking* is explained by the model through the increase of the divertor broadening S solely and is in quantitative agreement with the measurements.

The comparison of the model with experimental data suggests a linear increase of the *toroidal peaking* with magnetic perturbation coil current, i.e. perturbation strength. Increasing the fundamental mode number of the external magnetic perturbation reduces the *toroidal peaking*.

The overall agreement between the measurements and the model leads to the conclusion that in these discharge conditions plasma response is not a dominant factor for scrape-off layer heat transport, although the modelled heat flux variation in the *non-resonant* configuration overestimates the measured variation.

Previous studies reported that in H-Mode heat load caused by edge localized modes (ELMs) correlates with the pedestal pressure. In this thesis this correlation is confirmed in presence of a magnetic perturbation.

ELM filaments, that, without magnetic perturbation, are expelled at varying toroidal positions, are reported to *lock* to the external magnetic perturbation field, leading to enhanced sputtering and thermal loads on distinguished toroidal locations with respect to the phase of the magnetic perturbation.

Field penetration, as observed in low density L-Mode discharges with a $n = 1$ magnetic perturbation, leads to a fundamentally different heat flux pattern at the divertor target. The heat flux structure is in line with connection length calculations due to an ergodization of field lines at the plasma boundary with neighbouring field lines having significant different connection length. However, the extent along the target location is considerably larger than in discharges without field penetration and cannot be explained by the vacuum field approximation of the external magnetic perturbation. Due to the field penetration a flattening of the temperature profile around the $q = 2$ flux surface is observed, interpreted as a magnetic island. Characterizing this island as a current perturbation leads to similar connection length patterns as observed with an external magnetic perturbation. The observed heat flux pattern is in line with an ergodization of the plasma edge due to the superposition of the external magnetic perturbation and the internal magnetic island being locked in phase.

Shaping the plasma boundary can change the power fall-off length beyond established empirical multi machine scaling laws typically using global plasma parameters without dedicated shaping scans. Extending an L-Mode scaling law from ASDEX Upgrade reveals a dependence on edge electron temperature $T_{\mathrm{e,edge}}$ in both machines and no explicit size dependence. Changing the upper triangularity leads to changes in confinement as well as the power fall-off length in the presented TCV L-Mode database. Enhanced energy confinement at negative triangularity, explained by a reduction of turbulent transport in the confined region [Marinoni et al., 2009], is confirmed. The effect of triangularity on scrape-off layer turbulence could be a possible explanation for smaller $\lambda_{\mathrm{q}}^{\mathrm{out}}$ for decreasing δ_{up}, in qualitative agreement with turbulence simulation in limited plasmas [Riva et al., 2017].
Helium discharges exhibit a larger λ_{q} compared to deuterium, in line with previous studies on JET and ASDEX Upgrade. Reversal of the vertical drift direction has no significant influence on both, $\lambda_{\mathrm{q}}^{\mathrm{out}}$ and $\lambda_{\mathrm{q}}^{\mathrm{in}}$, in the presented database. The power fall-off length measured at the inner divertor target exhibits a non monotonic behaviour for changing δ_{up}. The largest $\lambda_{\mathrm{q}}^{\mathrm{in}}$ is obtained for $\delta_{\mathrm{up}} \approx 0$. The asymmetry between inner and outer λ_{q} is compared to an interpretation of the heuristic drift-based model used in previous studies finding partial agreement at positive, and no agreement at negative δ_{up}. The similarity between observations comparing both vertical drift directions challenge the assumption of a drift-based transport.
Considerations of a negative triangularity reactor due to reduced core turbulence and larger major radius of the divertor R_{div} apply λ_{q} from scaling laws deduced from positive triangularity discharges. The effect of a smaller λ_{q} for negative δ needs to be taken into account for an overall assessment of such novel configurations.

6.1 Outlook

The toroidally averaged heat flux in presence of a magnetic perturbation in L-Mode is characterized by the same values for the transport qualifiers, power fall-off length λ_q and divertor broadening S, compared to the profile without magnetic perturbation in the presented study. Due to measurement limitations this comparison was not possible for H-Mode discharges potentially having significant plasma response.
The presented model is in agreement with the heat flux variation in the *resonant* configuration but overestimates the heat flux variation in the *non-resonant* configuration in both L- and H-Mode. A comparison to more sophisticated models to reveal the limitations of the assumptions in the presented model is needed to investigate the reason for this overestimation as well as the potential difference in plasma conditions leading to significant plasma response.
It is observed that type-I ELM filaments can lock to the external magnetic perturbation field. For the presented discharges with type-I ELMs in this thesis this locking is not observed uniformly in discharges with similar plasma and magnetic perturbation field parameters. Further investigations are needed to understand the conditions leading to the locking of type-I ELM filaments.
The studies in TCV revealed a correlation of both, λ_q^{out} and $T_{e,edge}$, with δ_{up}. In order to distinguish between a direct effect of the triangularity on λ_q^{out} or an indirect effect through the change of $T_{e,edge}$ further simulations and experiments are needed.
It has been shown in ASDEX Upgrade that the two point model is in agreement between λ_{T_e} at the outer mid-plane and λ_q^{out} [Sun et al., 2015, Faitsch et al., 2015]. Using the two point model for both inner and outer divertor target with the same upstream point being the outer mid-plane predicts equal values for both inner and outer λ_q. The value for λ_q^{in} in the presented study is always smaller than λ_q^{out}. Further investigations are needed to study the asymmetry between inner and outer λ_q.

Appendix A

Vertical Drift-Based Model

A heuristic drift-based model has been introduced by Goldston [Goldston, 2012]. This model is able to describe H-Mode inter-ELM power fall-off length λ_q values measured in many nowadays tokamaks and is in good agreement to an empirical multi machine scaling law [Eich et al., 2013].
This model assumes vertical drifts, curvature and ∇ B drift, and balances the associated drift velocity with ion sound speed for the parallel velocity $v_{||}$. A poloidal width λ of the displacement of poloidal flux Ψ_p is defined as

$$\lambda = \frac{\Delta\Psi_p}{|\nabla\Psi_p|} \tag{A.1}$$

with $\Delta\Psi_p$ being displacement and $|\nabla\Psi_p|$ gradient of poloidal flux. This poloidal width is called the scrape-off layer width and is associated with the power fall-off length by Goldston.
The Maxwellian averaged ∇ B and curvature drift velocity is:

$$\langle \boldsymbol{v}_D \rangle = \frac{2T}{eZRB}\hat{\boldsymbol{z}} \tag{A.2}$$

with T temperature[1], e elementary charge, Z average ion charge, R major radius, B magnetic field strength and $\hat{\boldsymbol{z}}$ unit vector in z (vertical) direction. Note here, that the ion drift velocity is used for the derivation. A factor of Z has to be added taking the electron drift velocity.

[1]Goldston assumes equal ion and electron temperature, $T_e = T_i = T$. However, it is seen at the plasma boundary that this is not always satisfied and $T_i > T_e$ at the separatrix in most cases.

The displacement in poloidal flux at the separatrix between mid-plane MP (outer or inner) and highest (lowest) point S_x is:

$$\Delta\Psi_\mathrm{p} = \frac{1}{v_{||}} \int_{MP}^{S_\mathrm{x}} (\langle \boldsymbol{v}_\mathrm{D} \rangle \cdot \nabla\Psi_\mathrm{p}) \mathrm{d}l_{||} \tag{A.3}$$

with an averaged parallel velocity $v_{||}$[2].
Poloidal magnetic field B_pol is defined as:

$$B_\mathrm{pol} = \frac{|\nabla\Psi_\mathrm{p}|}{R}. \tag{A.4}$$

Integrating equation (A.3) in the poloidal plane along the flux surface:

$$\begin{aligned}
\Delta\Psi_\mathrm{p} &= \frac{1}{v_{||}} \int_{MP}^{S_\mathrm{x}} (\langle \boldsymbol{v}_\mathrm{D} \rangle \cdot \nabla\Psi_\mathrm{p}) \frac{B}{B_\mathrm{pol}} \mathrm{d}l_p \\
&= \frac{1}{v_{||}} \int_{MP}^{S_\mathrm{x}} \left(\langle \boldsymbol{v}_\mathrm{D} \rangle \cdot \frac{\nabla\Psi_\mathrm{p}}{|\nabla\Psi_\mathrm{p}|} \right) RB \mathrm{d}l_\mathrm{p} \\
&= \frac{1}{v_{||}} \int_{MP}^{S_\mathrm{x}} \frac{2T}{eZRB} RB \left(\hat{\boldsymbol{z}} \cdot \frac{\nabla\Psi_\mathrm{p}}{|\nabla\Psi_\mathrm{p}|} \right) \mathrm{d}l_\mathrm{p} \\
&= \frac{2T}{v_{||}eZ} \int_{MP}^{S_\mathrm{x}} \left(\hat{\boldsymbol{z}} \cdot \frac{\nabla\Psi_\mathrm{p}}{|\nabla\Psi_\mathrm{p}|} \right) \mathrm{d}l_\mathrm{p}.
\end{aligned} \tag{A.5}$$

For the last step a constant averaged T and Z along the integration path is assumed.
Rewriting the direction of the poloidal flux gradient as

$$\frac{\nabla\Psi_\mathrm{p}}{|\nabla\Psi_\mathrm{p}|} \mathrm{d}l_\mathrm{p} = \hat{\boldsymbol{\phi}} \times \mathrm{d}\boldsymbol{l}_\mathbf{p} \tag{A.6}$$

with $\hat{\boldsymbol{\phi}}$ being the unit vector in toroidal direction.
Inserting equation (A.6) into equation (A.5):

$$\begin{aligned}
\Delta\Psi_\mathrm{p} &= \frac{2T}{v_{||}eZ} \int_{MP}^{S_\mathrm{x}} \hat{\boldsymbol{z}} \cdot \left(\hat{\boldsymbol{\phi}} \times \mathrm{d}\boldsymbol{l}_\mathbf{p} \right) \\
&= \frac{2T}{v_{||}eZ} \int_{MP}^{S_\mathrm{x}} \left(\hat{\boldsymbol{z}} \times \hat{\boldsymbol{\phi}} \right) \cdot \mathrm{d}\boldsymbol{l}_\mathbf{p}.
\end{aligned} \tag{A.7}$$

[2]Goldston uses $v_{||} = \frac{1}{2} c_\mathrm{s}$ with c_s ion sound speed.

Using the definition of triangularity δ from appendix D as presented in [Faitsch et al., 2015], the integral is solved as[3]:

$$\int_{MP}^{S_\mathrm{x}} \left(\hat{\boldsymbol{z}} \times \hat{\boldsymbol{\phi}}\right) \cdot \mathrm{d}\boldsymbol{l}_\mathbf{p} = \int_{MP}^{S_\mathrm{x}} \hat{\boldsymbol{R}} \cdot \mathrm{d}\boldsymbol{l}_\mathbf{p} = a \cdot (1 \pm \delta_\mathrm{x}) \tag{A.8}$$

with '+' corresponding to outer and '-' to inner λ and $\hat{\boldsymbol{R}}$ unit vector in radial direction. The displacement in poloidal flux is hence:

$$\Delta\Psi_\mathrm{p} = \frac{2T}{v_{||} e Z} a \cdot (1 \pm \delta_\mathrm{x})\,. \tag{A.9}$$

Therefore, λ (equation (A.1)) is written as:

$$\lambda = \begin{cases} \frac{2T}{v_{||} e Z B_\mathrm{pol} R} a \cdot (1 \pm \delta_\mathrm{x}) & \text{ion drift} \\ \frac{2T}{v_{||} e B_\mathrm{pol} R} a \cdot (1 \pm \delta_\mathrm{x}) & \text{electron drift} \end{cases} \tag{A.10}$$

with 'x' being either upper or lower, depending on the drift direction of the considered species. The ratio between inner and outer λ is:

$$\frac{\lambda^\mathrm{in}}{\lambda^\mathrm{out}} = \frac{1 - \delta_\mathrm{x}}{1 + \delta_\mathrm{x}} \frac{v_{||}^\mathrm{out}}{v_{||}^\mathrm{in}}. \tag{A.11}$$

Inserting the assumption for the parallel flow velocity for H-Mode from [Goldston, 2012]:

$$v_{||} = \frac{1}{2} c_\mathrm{s} = \frac{1}{2} \left(\frac{(1+Z) T_\mathrm{sep}}{A m_\mathrm{p}}\right)^{\frac{1}{2}} \tag{A.12}$$

with Z and A average ion charge and mass, respectively and m_p proton mass and neglecting triangularity leads to (equation. (1) from [Goldston, 2012]):

$$\lambda_\mathrm{q}^\mathrm{H-Mode,Goldston} = \begin{cases} \frac{4a}{Z e B_\mathrm{pol} R} \left(\frac{A m_\mathrm{p} T_\mathrm{sep}}{(1+Z)}\right)^{\frac{1}{2}} & \text{ion drift} \\ \frac{4a}{e B_\mathrm{pol} R} \left(\frac{A m_\mathrm{p} T_\mathrm{sep}}{(1+Z)}\right)^{\frac{1}{2}} & \text{electron drift.} \end{cases} \tag{A.13}$$

[3] Goldston derived the equations for a plasma without triangularity.

Appendix B

Transformation of Time into Toroidal Angle with Rotating Magnetic Perturbation

In section 4 the time evolution of measured heat flux at a fixed toroidal location is related to a toroidal distribution (for a fixed time, or static magnetic perturbation). In this section the differences between a toroidal distribution and the variation of the coil currents in order to rotate the magnetic perturbation field are discussed using synthetic data. In the presented model both approaches can be compared. One is the *fixed time*, starting field lines at different toroidal positions at the target and computing the 2D heat flux structure for the given fixed magnetic coil currents. The other is the *fixed position*, starting field lines at a fixed toroidal position at the target and changing the currents in the magnetic perturbation coils in the same way as in the experiment. For an infinite number of coils the result would be the same. For a low number of coils per row, as it is the case for the experiments (8 in the case of ASDEX Upgrade, 9 foreseen for ITER [Daly et al., 2013]), the representation of the sinusoidal perturbation varies for different absolute phases[1]. For illustration the magnetic perturbation field from # 32217 with $n = 2$ and $I_{\mathrm{coil}} = 1\,\mathrm{kA}$ is taken. The Fourier spectrum of the magnetic perturbation field consists mainly of an $n = 2$ component with $800 \pm 10\,\mathrm{A}$ and an $n = 6$ component with $370 \pm 5\,\mathrm{A}$. The error bars indicate the change in time due to the rotation. The representation of the magnetic perturbation field is not changing significantly in time. The $n = 6$ component is a result of the finite coil extent in toroidal direction and aliasing from the 8 coils. The 2D heat flux is shown in figure B.1 for both approaches. For an $n = 2$ perturbation with 8 coils in toroidal direction the difference in the heat flux pattern is negligible. The corrugation of the separatrix is not taken into account here (see appendix C). A figure of merit discussed in this thesis is the toroidal variation of heat flux at different target locations (see q' in equation (2.36)). The variation in toroidal direction (or time transferred to a toroidal angle) at fixed target

[1] The time is also discrete due to finite current changes in the coils, however, this is in the order of ms compared to a rotation frequency at 1 Hz and negligible compared to the spatial discretization.

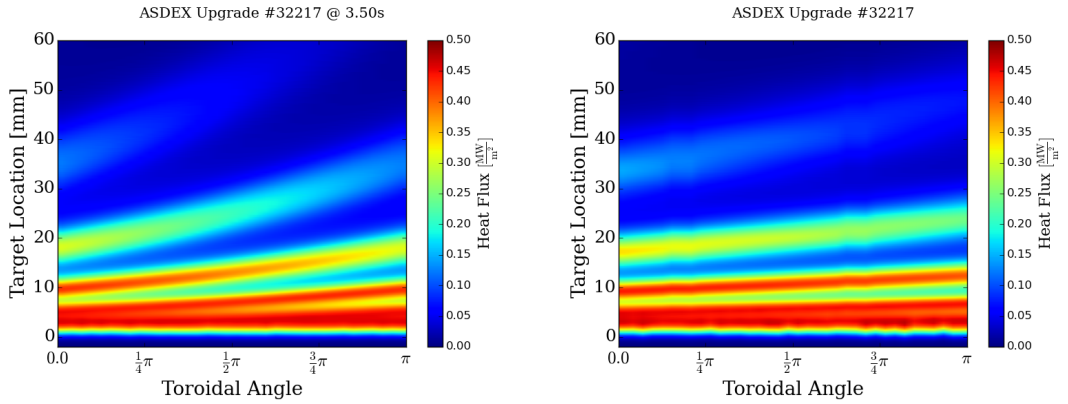

(a) Fixed time. (b) Fixed position.

Figure B.1: Modelled 2D heat flux profile for fixed time and fixed position, both without taking the separatrix corrugation into account.

locations $s = 0.21, 0.67, 1 \cdot \lambda_q$ is shown in figure B.2. In both approaches the variation is close to sinusoidal with two periods within 2π due to the toroidal mode number $n = 2$ of the magnetic perturbation.

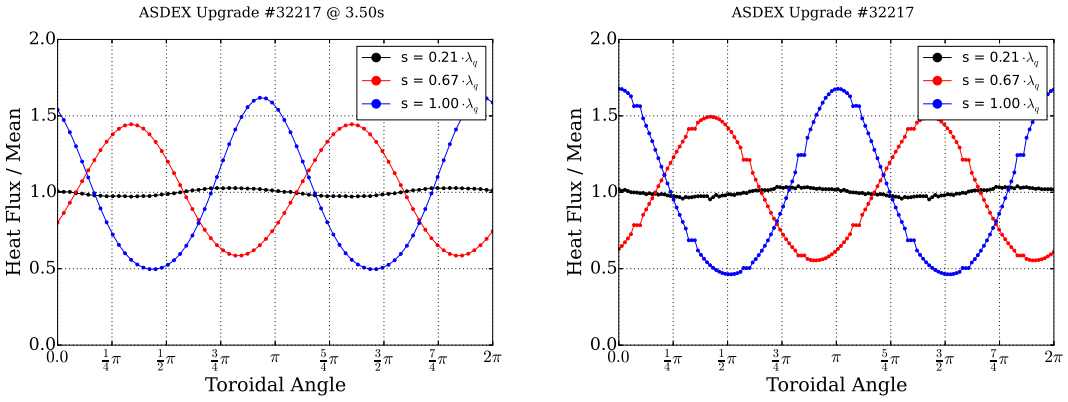

(a) Fixed time. (b) Fixed position.

Figure B.2: Modelled toroidal (time) heat flux variation for fixed time and fixed position, both without taking the separatrix corrugation into account.

Appendix C

Influence of the Radial Displacement of the Plasma Boundary in the Model

With the application of the external magnetic perturbation the plasma boundary is radially corrugated, e.g. [Willensdorfer et al., 2016, Kirschner, 2017]. As discussed in section 3.2.3, this deformation can be treated with the model. The model is based on field lines, making it convenient to handle the displacement as the change of the length of field lines at the outer mid-plane. The field line length at the outer mid-plane is shown in figure C.1. The black line indicates the used non-axisymmetric separatrix. Field lines are traces starting at the outer divertor target and either intersect the first wall or are terminated at a maximum length of 2 km. The separatrix corrugation is obtained from field lines with a length of 120-125 m. The mean value is shifted afterwards to be the same as the axisymmetric separatrix

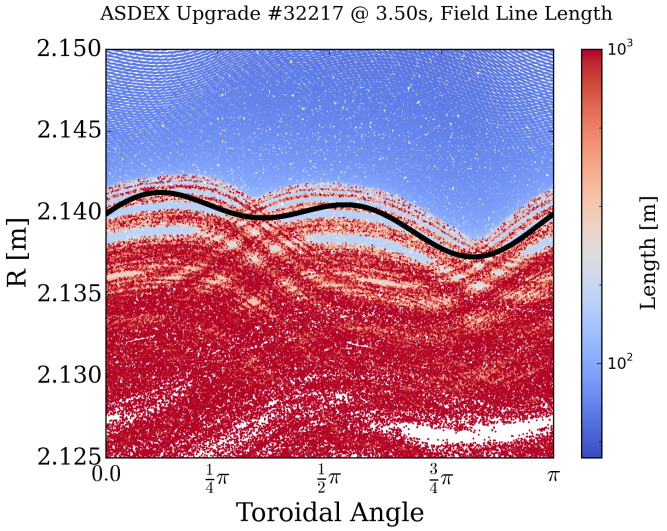

Figure C.1: Connection length at the outer mid-plane with the separatrix obtained as presented in section 3.2.

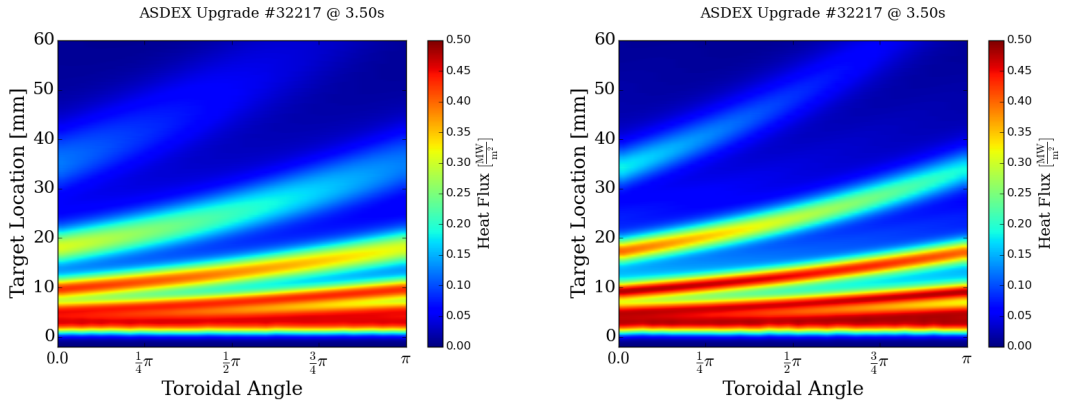

(a) Modelling without separatrix corrugation. (b) Modelling with separatrix corrugation $R_{sep}(\Phi)$.

Figure C.2: Modelled 2D heat flux profile for the *resonant* configuration.

without a magnetic perturbation.
The correction of the radial displacement at the outer mid-plane leads to an increase of the heat flux variation in the *resonant* configuration and a decrease in the *non-resonant* configuration in the model. The 2D heat flux is compared in figure C.2 for the *resonant* configuration, showing only moderate differences. Different toroidal positions and the averaged profile are shown in figure C.3. The averaged profile is the same with and without taking the separatrix corrugation into account. The averaged profile is the same as the profile without magnetic perturbation. However, the variation along the target location is increased taking the separatrix corrugation into account. The maximum heat flux at

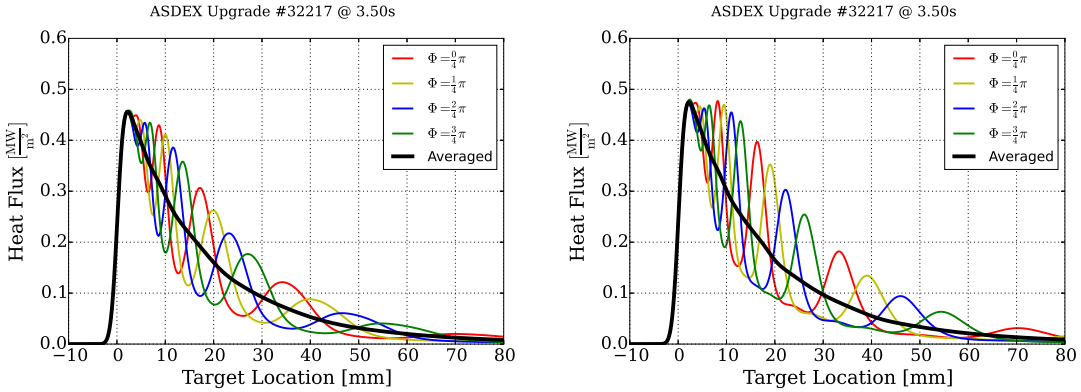

(a) Modelling without separatrix corrugation. (b) Modelling with separatrix corrugation $R_{sep}(\Phi)$.

Figure C.3: Different toroidal phases and averaged heat flux profiles for the *resonant* configuration from modelling.

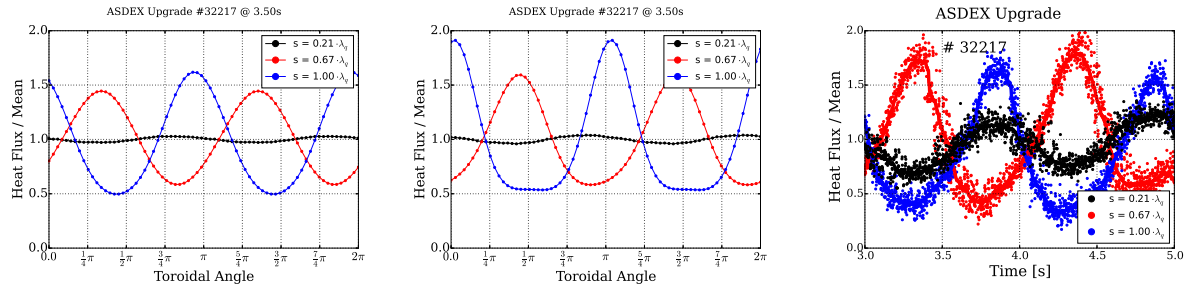

(a) Modelling without separatrix corrugation.

(b) Modelling with separatrix corrugation $R_{sep}(\Phi)$.

(c) Measurement.

Figure C.4: Toroidal (time) heat flux variation for the *resonant* configuration.

a given toroidal position is not changed and is at the position of the axisymmetric, or toroidally averaged, maximum where the variation is negligible.
The toroidal variation $q'(s, \phi)$ (see definition in equation (2.36)) at three target locations is shown in figure C.4 for the *resonant* configuration. The variation at a given target location changes from a nearly sinusoidal for the complete profile to a more triangular shaped variation far away from the separatrix (blue lines in figure C.4) in the modelled heat flux by taking the separatrix corrugation into account. The measured toroidal variation exhibits a more sinusoidal shape than the modelled heat flux with separatrix corrugation but the *toroidal maximum* is closer than without separatrix corrugation in the model.

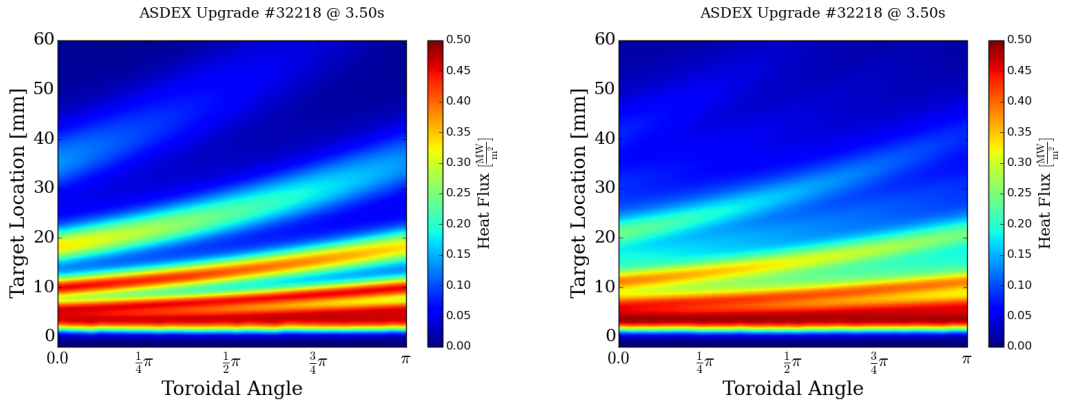

(a) Modelling without separatrix corrugation. (b) Modelling with separatrix corrugation $R_{sep}(\Phi)$.

Figure C.5: Modelled 2D heat flux profile for the *non-resonant* configuration.

The same three comparisons for the *non-resonant* configuration are shown in figure C.5, figure C.6 and figure C.7. Without taking the radial displacement into account, modelled profiles do not differ significantly when varying *differential phase* (*resonant*, *non-resonant*). The heat flux variation significantly varies with the correction of the corrugation in the *non-resonant* configuration.
In the experiment, a clear difference is observed with the variation of the *differential phase*, e.g. in the heat flux time traces in figure 4.3. In the modelled heat flux this is only reproduced by taking plasma boundary displacement into account, although, the *non-resonant* case in the model still exhibits larger variations than observed in the experiment.

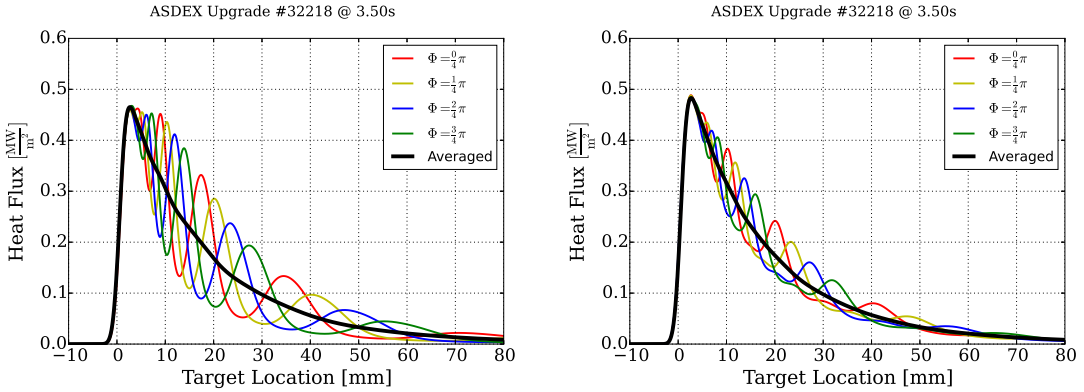

(a) Modelling without separatrix corrugation. (b) Modelling with separatrix corrugation $R_{sep}(\Phi)$.

Figure C.6: Different toroidal phases and averaged heat flux profiles for the *non-resonant* configuration from modelling.

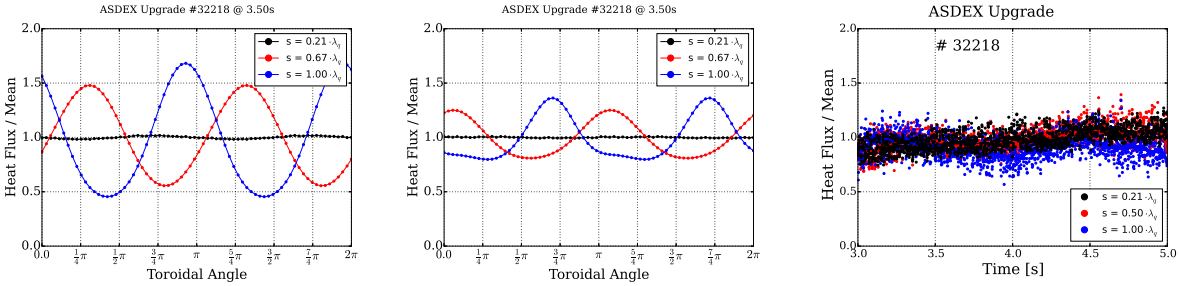

(a) Modelling without separatrix corrugation.

(b) Modelling with separatrix corrugation $R_{sep}(\Phi)$.

(c) Measurement.

Figure C.7: Toroidal (time) heat flux variation for the *non-resonant* configuration.

This can be seen by comparing the toroidal variation in figure C.7(b) and (c).
The separatrix corrugation is taken into account for all modelled heat flux profile shown in chapter 4 unless stated otherwise.

Appendix D

Tokamak Geometry Definitions

The tokamak geometry as used for the scaling laws in section 2.1.1.3 is defined as in [Luce, 2013]:

$$a = \frac{R_{\max} - R_{\min}}{2} \tag{D.1}$$

$$R_{\text{geo}} = \frac{R_{\max} + R_{\min}}{2} \tag{D.2}$$

$$\kappa = \frac{z_{\max} - z_{\min}}{2a} = \frac{b}{a} \tag{D.3}$$

$$\delta_{\text{up}} = \frac{R_{\text{geo}} - R_{\text{up}}}{a} \tag{D.4}$$

$$\delta_{\text{low}} = \frac{R_{\text{geo}} - R_{\text{low}}}{a} \tag{D.5}$$

with $R_{\max}$, $R_{\min}$, R_{up} and R_{low} the radius of the inner, outer, upper and lower most points of the separatrix for a diverted plasma and $z_{\max}$, $z_{\min}$ the vertical coordinate at the upper, lower most point of the separatrix.
In figure D.1 a poloidal cross-section of a typical separatrix in ASDEX Upgrade is shown together with the (geometrical) major radius R_{geo}, the major radius of the plasma axis R_{axis} and the width (2a) and height (2b) of the plasma. a is referred to as *minor radius*, κ as the *elongation* and δ_{up} (δ_{low}) the *upper* (*lower*) *triangularity*. Commonly used definitions of plasma parameters:
Aspect ratio A:

$$A = \frac{R}{a}. \tag{D.6}$$

Effective elongation $\hat{\kappa}$:

$$\hat{\kappa} = \sqrt{\frac{1 + \kappa^2}{2}}. \tag{D.7}$$

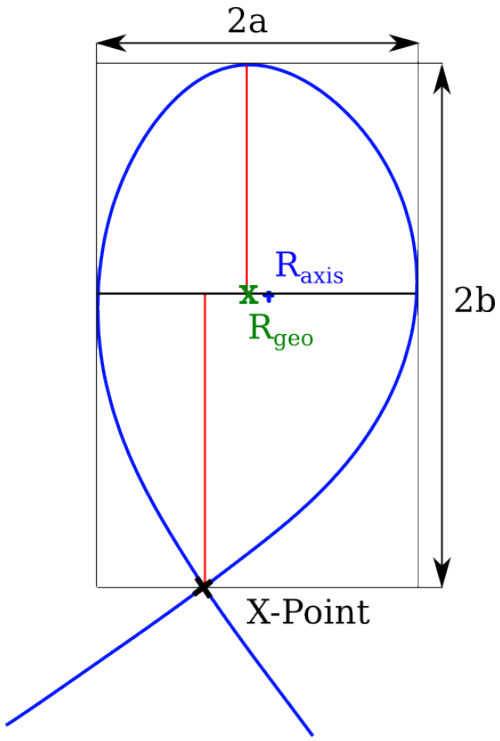

Figure D.1: Poloidal cross-section of a typical separatrix in ASDEX Upgrade.

Poloidal magnetic field B_{pol}:

$$B_{\mathrm{pol}} = \frac{\mu_0 I_{\mathrm{p}}}{2\pi a \hat{\kappa}} \tag{D.8}$$

with μ_0 vacuum permeability and I_{p} plasma current.
Cylindrical safety factor q_{cyl}:

$$q_{\mathrm{cyl}} = \frac{B_{\mathrm{tor}}}{B_{\mathrm{pol}}} \frac{1}{A} \hat{\kappa}. \tag{D.9}$$

Field line length L_{OMP}[1]:

$$L_{\mathrm{OMP}} = \pi q_{\mathrm{cyl}} R. \tag{D.10}$$

[1]This is an approximation for a cylindrical plasma without X-point and taking the outer mid-plane to be in the middle of the field line. The connection length at the separatrix diverges and the divertor leg length is not captured in this formula. However, for a typical field line in the scrape-off layer of ASDEX Upgrade starting a few mm away from the separatrix towards the outer target, this formula is in good agreement to field line tracing.

Bibliography

[Ahn et al., 2010] Ahn, J.-W., Canik, J., Soukhanovskii, V., Maingi, R., and Battaglia, D. (2010). Modification of divertor heat and particle flux profiles with applied 3D fields in NSTX H-mode plasmas. *Nuclear Fusion*, 50, 045010.

[Brezinsek et al., 2013] Brezinsek, S., Loarer, T., Philipps, V., et al. (2013). Fuel retention studies with the ITER-Like Wall in JET. *Nuclear Fusion*, 53, 083023.

[Brida et al., 2017] Brida, D., Lunt, T., Wischmeier, M., et al. (2017). Heat flux pattern in detached L-modes and ELM mitigated H-modes with rotating magnetic perturbations in ASDEX Upgrade. *Nuclear Fusion*, 57, 116006.

[Cahyna et al., 2014] Cahyna, P., Peterka, M., Nardon, E., Frerichs, H., and Panek, R. (2014). Method for comparison of tokamak divertor strike point data with magnetic perturbation models. *Nuclear Fusion*, 54, 064002.

[Camenen et al., 2007] Camenen, Y., Pochelon, A., Behn, R., et al. (2007). Impact of plasma triangularity and collisionality on electron heat transport in TCV L-mode plasmas. *Nuclear Fusion*, 47, 510.

[Coda et al., 2017] Coda, S., Ahn, J., Albanese, R., et al. (2017). Overview of the TCV tokamak program: scientific progress and facility upgrades. *Nuclear Fusion*, 57, 102011.

[Daly et al., 2013] Daly, E. et al. (2013). Update on design of the ITER in-vessel coils. *Fusion Science and Technology*, 64, 168.

[Dux et al., 2009] Dux, R., Bobkov, V., Herrmann, A., et al. (2009). Plasma-wall interaction and plasma behaviour in the non-boronised all tungsten ASDEX Upgrade. *Journal of Nuclear Materials*, 390, 858.

[Eich et al., 2003a] Eich, T., Herrmann, A., Andrew, P., and Loarte, A. (2003a). Power deposition measurements in deuterium and helium discharges in JET MKIIGB divertor by IR-thermography. *Journal of Nuclear Materials*, 313-316, 919.

[Eich et al., 2003b] Eich, T., Herrmann, A., and Neuhauser, J. (2003b). Nonaxisymmetric energy deposition pattern on ASDEX Upgrade divertor target plates during type-I edge-localized modes. *Phys. Rev. Lett.*, 91, 195003.

[Eich et al., 2005] Eich, T., Herrmann, A., Neuhauser, J., et al. (2005). Type-I ELM substructure on the divertor target plates in ASDEX Upgrade. *Plasma Physics and Controlled Fusion*, 47, 815.

[Eich et al., 2013] Eich, T., Leonard, A., Pitts, R., et al. (2013). Scaling of the tokamak near the scrape-off layer H-mode power width and implications for ITER. *Nuclear Fusion*, 53, 093031.

[Eich et al., 2000] Eich, T., Reiser, D., and Finken, K. (2000). Two dimensional modelling approach to transport properties of the TEXTOR-DED laminar zone. *Nuclear Fusion*, 40, 1757.

[Eich et al., 2011] Eich, T., Sieglin, B., Scarabosio, A., et al. (2011). Inter-ELM power decay length for JET and ASDEX Upgrade: Measurement and comparison with heuristic drift-based model. *Physical Review Letters*, 107, 215001.

[Eich et al., 2017] Eich, T., Sieglin, B., Thornton, A., et al. (2017). ELM divertor peak energy fluence scaling to ITER with data from JET, MAST and ASDEX Upgrade. *Nuclear Materials and Energy*, 12, 84.

[euro-fusion.org, 2011] euro-fusion.org (2011). *Figure of Tokamak Principle*. `https://www.euro-fusion.org/wpcms/wp-content/uploads/2011/09/JG05.537-1c.jpg` (accessed April 11, 2017).

[Evans et al., 2004] Evans, T. E., Moyer, R. A., Thomas, P. R., et al. (2004). Suppression of large edge-localized modes in high-confinement DIII-D plasmas with a stochastic magnetic boundary. *Phys. Rev. Lett.*, 92, 235003.

[Faitsch et al., 2017a] Faitsch, M., Maurizio, R., Gallo, A., et al. (2017a). Triangularity dependence of the L-mode scrape-off layer power fall-off length in TCV. *Plasma Physics and Controlled Fusion*, submitted.

[Faitsch et al., 2017b] Faitsch, M., Sieglin, B., Eich, T., et al. (2017b). 2D heat flux in ASDEX Upgrade L-Mode with magnetic perturbation. *Nuclear Materials and Energy*, 12, 1020.

[Faitsch et al., 2017c] Faitsch, M., Sieglin, B., Eich, T., et al. (2017c). Divertor heat load in ASDEX Upgrade L-mode in presence of external magnetic perturbation. *Plasma Physics and Controlled Fusion*, 59, 095006.

[Faitsch et al., 2015] Faitsch, M., Sieglin, B., Eich, T., et al. (2015). Change of the scrape-off layer power width with the toroidal B-field direction in ASDEX Upgrade. *Plasma Physics and Controlled Fusion*, 57, 075005.

[Federici et al., 2014] Federici, G., Kemp, R., Ward, D., et al. (2014). Overview of EU DEMO design and R & D activities. *Fusion Engineering and Design*, 89, 882.

[Feng et al., 1997] Feng, Y., Sardei, F., Kisslinger, J., and Grigull, P. (1997). A 3D monte carlo code for plasma transport in island divertors. *Journal of Nuclear Materials*, 241, 930.

[Fietz et al., 2015] Fietz, S., Bergmann, A., Classen, I., et al. (2015). Influence of externally applied magnetic perturbations on neoclassical tearing modes at ASDEX Upgrade. *Nuclear Fusion*, 55, 013018.

[Finken et al., 1998] Finken, K., Eich, T., and Kaleck, A. (1998). First modelling of the TEXTOR DED near field divertor. *Nuclear Fusion*, 38, 515.

[Fitzpatrick, 1998] Fitzpatrick, R. (1998). Bifurcated states of a rotating tokamak plasma in the presence of a static error-field. *Physics of Plasmas*, 5, 3325.

[Fitzpatrick, 2012] Fitzpatrick, R. (2012). Nonlinear error-field penetration in low density ohmically heated tokamak plasmas. *Plasma Physics and Controlled Fusion*, 54, 094002.

[Franke, 1997] Franke, S. (1997). *Application of Thomson scattering at 1.06mm as a diagnostic for spatial profile measurements of electron temperature and density on the TCV tokamak*. PhD thesis, EPFL-Lausanne, Switzerland.

[Fundamenski et al., 2011] Fundamenski, W., Eich, T., Devaux, S., et al. (2011). Multiparameter scaling of divertor power load profiles in D, H and He plasmas on JET and implications for ITER. *Nuclear Fusion*, 51, 083028.

[Gallo et al., 2018] Gallo, A., Fedorczak, N., Elmore, S., et al. (2018). Impact of the plasma geometry on divertor power exhaust: experimental evidence from TCV and simulations with SolEdge2D and TOKAM3X. *Plasma Physics and Controlled Fusion*, 60, 014007.

[Gallo et al., 2016] Gallo, A., Fedorczak, N., Maurizio, R., et al. (2016). Effect of plasma geometry on divertor heat flux spreading: MONALISA simulations and experimental results from TCV. *Nuclear Materials and Energy*, 12, 893.

[Garcia-Munoz et al., 2013] Garcia-Munoz, M., kslompolo, S., de Marne, P., et al. (2013). Fast-ion losses induced by ELMs and externally applied magnetic perturbations in the ASDEX Upgrade tokamak. *Plasma Physics and Controlled Fusion*, 55, 124014.

[Goldston, 2012] Goldston, R. J. (2012). Heuristic drift-based model of the power scrape-off width in low-gas-puff H-mode tokamaks. *Nuclear Fusion*, 52, 013009.

[Gourdon et al., 1971] Gourdon, C., Marty, D., Maschke, E., and Touche, J. (1971). The torsatron without toroidal field coils as a solution of the divertor problem. *Nuclear Fusion*, 11, 167.

[Greenwald, 2002] Greenwald, M. (2002). Density limits in toroidal plasmas. *Plasma Physics and Controlled Fusion*, 44, R27.

[Gruber et al., 1993] Gruber, O., Lackner, K., Pautasso, G., Seidel, U., and Streibl, B. (1993). Vertical displacement events and halo currents. *Plasma Physics and Controlled Fusion*, 35, B191.

[Gunn et al., 2007] Gunn, J., Boucher, C., Dionne, M., et al. (2007). Evidence for a poloidally localized enhancement of radial transport in the scrape-off layer of the tore supra tokamak. *Journal of Nuclear Materials*, 363-365, 484.

[Gunn et al., 2016] Gunn, J., Carpentier-Chouchana, S., Dejarnac, R., et al. (2016). Ion orbit modelling of ELM heat loads on ITER divertor vertical targets. *Nuclear Materials and Energy*, 12, 75.

[Harting et al., 2012] Harting, D., Liang, Y., Jachmich, S., et al. (2012). Strike point splitting in the heat and particle flux profiles compared with the edge magnetic topology in a n=2 resonant magnetic perturbation field at JET. *Nuclear Fusion*, 52, 054009.

[Hender et al., 1992] Hender, T., Fitzpatrick, R., Morris, A., et al. (1992). Effect of resonant magnetic perturbations on COMPASS-C tokamak discharges. *Nuclear Fusion*, 32, 2091.

[Herrmann, 2002] Herrmann, A. (2002). Overview on stationary and transient divertor heat loads. *Plasma Physics and Controlled Fusion*, 44, 883.

[Herrmann et al., 2011] Herrmann, A., Drube, R., Lunt, T., and de Marne, P. (2011). Real-time protection of in-vessel components in ASDEX Upgrade. *Fusion Engineering and Design*, 86, 530.

[Herrmann et al., 2013] Herrmann, A., Greuner, H., Jaksic, N., et al. (2013). Design and concept validation of the new solid tungsten divertor for ASDEX Upgrade. *Fusion Engineering and Design*, 88, 577.

[Herrmann et al., 1995] Herrmann, A., Junker, W., Guenther, K., et al. (1995). Energy flux to the ASDEX-Upgrade divertor plates determined by thermography and calorimetry. *Plasma Physics and Controlled Fusion*, 37, 17.

[Hirshman and Whitson, 1983] Hirshman, S. P. and Whitson, J. C. (1983). Steepest-descent moment method for three-dimensional magnetohydrodynamic equilibria. *The Physics of Fluids*, 26, 3553.

[Hofmann et al., 1994] Hofmann, F., Lister, J. B., Anton, W., et al. (1994). Creation and control of variably shaped plasmas in TCV. *Plasma Physics and Controlled Fusion*, 36, B277.

[Hofmann and Tonetti, 1988] Hofmann, F. and Tonetti, G. (1988). Tokamak equilibrium reconstruction using faraday rotation measurements. *Nuclear Fusion*, 28, 1871.

[Huysmans and Czarny, 2007] Huysmans, G. and Czarny, O. (2007). Mhd stability in x-point geometry: simulation of elms. *Nuclear Fusion*, 47, 659.

[Igochine et al., 2017] Igochine, V., Piovesan, P., Classen, I., et al. (2017). MHD limits and plasma response in high-beta hybrid operations in ASDEX Upgrade . *Nuclear Fusion*, 57, 116027.

[ITER Physics Basis Editors et al., 1999] ITER Physics Basis Editors, ITER Physics Expert Group Chairs and Co-Chairs, and ITER Joint Central Team and Physics Integration Unit (1999). Chapter 1: Overview and summary. *Nuclear Fusion*, 39, 2137.

[ITER Physics Expert Group on Confinement and Transport et al., 1999] ITER Physics Expert Group on Confinement and Transport, ITER Physics Expert Group on Confinement Modelling and Database, and ITER Physics Basis Editors (1999). Chapter 2: Plasma confinement and transport. *Nuclear Fusion*, 39, 2175.

[Jakubowski et al., 2009] Jakubowski, M., Evans, T., Fenstermacher, M., et al. (2009). Overview of the results on divertor heat loads in RMP controlled H-mode plasmas on DIII-D. *Nuclear Fusion*, 49, 095013.

[Jeon et al., 2012] Jeon, Y. M., Park, J.-K., Yoon, S. W., et al. (2012). Suppression of edge localized modes in high-confinement KSTAR plasmas by nonaxisymmetric magnetic perturbations. *Phys. Rev. Lett.*, 109, 035004.

[Kallenbach et al., 2015] Kallenbach, A., Bernert, M., Beurskens, M., et al. (2015). Partial detachment of high power discharges in ASDEX Upgrade. *Nuclear Fusion*, 55, 053026.

[Kallenbach et al., 2001] Kallenbach, A., Carlson, A., Pautasso, G., et al. (2001). Electric currents in the scrape-off layer in ASDEX Upgrade . *Journal of Nuclear Materials*, 290293, 639.

[Kallenbach et al., 2005] Kallenbach, A., Neu, R., Dux, R., et al. (2005). Tokamak operation with high-Z plasma facing components . *Plasma Physics and Controlled Fusion*, 47, B207.

[Keilhacker et al., 1984] Keilhacker, M., Becker, G., Bernhardi, K., et al. (1984). Confinement studies in L and H-type Asdex discharges. *Plasma Physics and Controlled Fusion*, 26, 49.

[Kikuchi et al., 2014] Kikuchi, M., Takizuka, T., and Furukawa, M. (2014). Negative triangularity as a possible tokamak scenario. In *Proceedings of the 12th Asia Pacific Physics Conference (APPC12)*, volume 1, page 015014.

[Kirk et al., 2015] Kirk, A., Suttrop, W., Chapman, I., et al. (2015). Effect of resonant magnetic perturbations on low collisionality discharges in MAST and a comparison with-ASDEX Upgrade. *Nuclear Fusion*, 55, 043011.

[Kirschner, 2017] Kirschner, J. (2017). *Influence of external magnetic perturbations on the plasma boundary in L-mode and on the plasma position control system of ASDEX Upgrade*. Diploma thesis, TU Wien.

[Klimov et al., 2009] Klimov, N., Podkovyrov, V., Zhitlukhin, A., et al. (2009). Experimental study of PFCs erosion under ITER-like transient loads at plasma gun facility QSPA. *Journal of Nuclear Materials*, 390, 721.

[Koslowski et al., 2006] Koslowski, H., Liang, Y., Kraemer-Flecken, A., et al. (2006). Dependence of the threshold for perturbation field generated m / n = 2/1 tearing modes on the plasma fluid rotation. *Nuclear Fusion*, 46, L1.

[Lang et al., 2013] Lang, P., Loarte, A., Saibene, G., et al. (2013). ELM control strategies and tools: status and potential for ITER. *Nuclear Fusion*, 53, 043004.

[Leonard, 2014] Leonard, A. W. (2014). Edge-localized-modes in tokamaks. *Physics of Plasmas*, 21, 090501.

[Leuterer et al., 2001] Leuterer, F., Beckmann, M., Borchegowski, A., et al. (2001). The ECRH system of ASDEX Upgrade. *Fusion Engineering and Design*, 56, 615 .

[Li et al., 2017] Li, L., Liu, Y. Q., Wang, N., et al. (2017). Toroidal modeling of plasma response to RMP fields in ITER. *Plasma Physics and Controlled Fusion*, 59, 044005.

[Liang et al., 2007] Liang, Y., Koslowski, H. R., Thomas, P. R., et al. (2007). Active control of type-I edge-localized modes with $n = 1$ perturbation fields in the JET tokamak. *Phys. Rev. Lett.*, 98, 265004.

[Liu et al., 2011] Liu, Y., Kirk, A., Gribov, Y., et al. (2011). Modelling of plasma response to resonant magnetic perturbation fields in MAST and ITER. *Nuclear Fusion*, 51, 083002.

[Liu et al., 2016] Liu, Y., Ryan, D., Kirk, A., et al. (2016). Toroidal modelling of RMP response in ASDEX Upgrade: coil phase scan, q95 dependence, and toroidal torques. *Nuclear Fusion*, 56, 056015.

[Liu et al., 2000] Liu, Y. Q., Bondeson, A., Fransson, C. M., Lennartson, B., and Breitholtz, C. (2000). Feedback stabilization of nonaxisymmetric resistive wall modes in tokamaks. i. electromagnetic model. *Physics of Plasmas*, 7, 3681.

[Loarte et al., 1999] Loarte, A., Bosch, S., Chankin, A., et al. (1999). Multi-machine scaling of the divertor peak heat flux and width for L-mode and H-mode discharges. *Journal of Nuclear Materials*, 266, 587.

[Loarte et al., 2014] Loarte, A., Huijsmans, G., Futatani, S., et al. (2014). Progress on the application of ELM control schemes to ITER scenarios from the non-active phase to DT operation. *Nuclear Fusion*, 54, 033007.

[Loarte et al., 2007] Loarte, A., Lipschultz, B., Kukushkin, A., et al. (2007). Chapter 4: Power and particle control. *Nuclear Fusion*, 47, S203.

[Loarte et al., 2003] Loarte, A., Saibene, G., Sartori, R., et al. (2003). Characteristics of type I ELM energy and particle losses in existing devices and their extrapolation to ITER. *Plasma Physics and Controlled Fusion*, 45, 1549.

[Loewenhoff et al., 2015] Loewenhoff, T., Linke, J., Pintsuk, G., Pitts, R., and Riccardi, B. (2015). ITER-W monoblocks under high pulse number transient heat loads at high temperature. *Journal of Nuclear Materials*, 463, 202.

[Luce, 2013] Luce, T. C. (2013). An analytic functional form for characterization and generation of axisymmetric plasma boundaries. *Plasma Physics and Controlled Fusion*, 55, 095009.

[Makowski et al., 2012] Makowski, M. A., Elder, D., Gray, T. K., et al. (2012). Analysis of a multi-machine database on divertor heat fluxes. *Physics of Plasmas*, 19, 056122.

[Marinoni et al., 2009] Marinoni, A., Brunner, S., Camenen, Y., et al. (2009). The effect of plasma triangularity on turbulent transport: modeling TCV experiments by linear and non-linear gyrokinetic simulations. *Plasma Physics and Controlled Fusion*, 51, 055016.

[Matthews, 2013] Matthews, G. (2013). Plasma operation with an all metal first-wall: Comparison of an ITER-like wall with a carbon wall in JET. *Journal of Nuclear Materials*, 438, S2.

[Maurizio et al., 2017] Maurizio, R., Elmore, S., Fedorczak, N., et al. (2017). Divertor power load studies for attached L-mode single-null plasmas in TCV. *Nuclear Fusion*, submitted.

[McCarthy et al., 1999] McCarthy, P. J., Martin, P., and Schneider, W. (1999). The CLISTE interpretive equilibrium code. Garching: Max-Planck-Institut für Plasmaphysik.

[Medvedev et al., 2015] Medvedev, S., Kikuchi, M., Villard, L., et al. (2015). The negative triangularity tokamak: stability limits and prospects as a fusion energy system. *Nuclear Fusion*, 55, 063013.

[Mlynek et al., 2010] Mlynek, A., Schramm, G., Eixenberger, H., et al. (2010). Design of a digital multiradian phase detector and its application in fusion plasma interferometry. *Review of Scientific Instruments*, 81, 033507.

[Moret et al., 1997] Moret, J.-M., Franke, S., Weisen, H., et al. (1997). Influence of plasma shape on transport in the TCV tokamak. *Phys. Rev. Lett.*, 79, 2057.

[Moyer et al., 2017] Moyer, R. A., Paz-Soldan, C., Nazikian, R., et al. (2017). Validation of the model for ELM suppression with 3D magnetic fields using low torque ITER baseline scenario discharges in DIII-D. *Physics of Plasmas*, 24, 102501.

[Müller et al., 2013] Müller, H., Lunt, T., Suttrop, W., et al. (2013). Modification of scrape-off layer transport and turbulence by non-axisymmetric magnetic perturbations in ASDEX Upgrade. *Journal of Nuclear Materials*, 438, S64.

[Neu et al., 2007] Neu, R., Balden, M., Bobkov, V., et al. (2007). Plasma wall interaction and its implication in an all tungsten divertor tokamak. *Plasma Physics and Controlled Fusion*, 49, B59.

[Nguyen et al., 1997] Nguyen, F., Chendrih, P., and Grosman, A. (1997). Interaction of stochastic boundary layer with plasma facing components. *Nuclear Fusion*, 37, 743.

[Nille, 2016] Nille, D. (2016). Comparison between 1D and 2D approximations describing heat diffusion in the ASDEX Upgrade Divertor. Master's thesis, Universität Ulm.

[Nille et al., 2017] Nille, D., von Toussaint, U., Sieglin, B., Faitsch, M., and ASDEX Upgrade Team (2017). Probabilistic inference of surface heat flux densities from infrared thermography. *Science and Engineering*, submitted.

[Orain et al., 2013] Orain, F., Bcoulet, M., Dif-Pradalier, G., et al. (2013). Non-linear magnetohydrodynamic modeling of plasma response to resonant magnetic perturbations. *Physics of Plasmas*, 20, 102510.

[Orain et al., 2017] Orain, F., Hoelzl, M., Viezzer, E., et al. (2017). Non-linear modeling of the plasma response to RMPs in ASDEX Upgrade. *Nuclear Fusion*, 57, 022013.

[Orain et al., 2016] Orain, F., Hoelzl, M., Viezzer, E., et al. (2016). Non-linear modeling of the Edge Localized Mode control by Resonant Magnetic Perturbations in ASDEX Upgrade. *26th IAEA Fusion Energy Conference, Kyoto, Japan (10/2016)*, TH/P1-26.

[Pamela et al., 2009] Pamela, J., Becoulet, A., Borba, D., et al. (2009). Efficiency and availability driven R&D issues for DEMO. *Fusion Engineering and Design*, 84, 194.

[Piovesan et al., 2017] Piovesan, P., Igochine, V., Turco, F., et al. (2017). Impact of ideal MHD stability limits on high-beta hybrid operation. *Plasma Physics and Controlled Fusion*, 59, 014027.

[Pitts et al., 2003] Pitts, R., Alberti, S., Blanchard, P., et al. (2003). ELM driven divertor target currents on TCV. *Nuclear Fusion*, 43, 1145.

[Pitts et al., 2005] Pitts, R. A., Andrew, P., Bonnin, X., et al. (2005). Edge and divertor physics with reversed toroidal field in JET. *Journal of Nuclear Materials*, 337339, 146.

[Pitts et al., 2009] Pitts, R. A., Kukushkin, A., Loarte, A., et al. (2009). Status and physics basis of the ITER divertor. *Physica Scripta*, 2009, 014001.

[Planck, 1900a] Planck, M. (1900a). ber eine Verbesserung der Wienschen Spektralgleichung. *Deutsche Physikalische Gesellschaft, Verhandlungen*, 2, 202.

[Planck, 1900b] Planck, M. (1900b). Zur Theorie des Gesetzes der Energieverteilung im Normalspektrum. *Deutsche Physikalische Gesellschaft, Verhandlungen*, 2, 237.

[Pochelon et al., 2012] Pochelon, A., Angelino, P., Behn, R., et al. (2012). Recent TCV results - innovative plasma shaping to improve plasma properties and insight. *Plasma and Fusion Research*, 7, 2502148.

[Pochelon et al., 1999] Pochelon, A., Goodman, T., Henderson, M., et al. (1999). Energy confinement and MHD activity in shaped TCV plasmas with localized electron cyclotron heating. *Nuclear Fusion*, 39, 1807.

[Rathgeber et al., 2013] Rathgeber, S. K., Barrera, L., Eich, T., et al. (2013). Estimation of edge electron temperature profiles via forward modelling of the electron cyclotron radiation transport at ASDEX Upgrade. *Plasma Physics and Controlled Fusion*, 55, 025004.

[Riccardi et al., 2011] Riccardi, B., Giniatulin, R., Klimov, N., Koidan, V., and Loarte, A. (2011). Preliminary results of the experimental study of PFCs exposure to ELMs-like transient loads followed by high heat flux thermal fatigue. *Fusion Engineering and Design*, 86, 1665.

[Riva et al., 2017] Riva, F., Lanti, E., Jolliet, S., and Ricci, P. (2017). Plasma shaping effects on tokamak scrape-off layer turbulence. *Plasma Physics and Controlled Fusion*, 59, 035001.

[Roth et al., 2009] Roth, J., Tsitrone, E., Loarte, A., et al. (2009). Recent analysis of key plasma wall interactions issues for ITER. *Journal of Nuclear Materials*, 390, 1.

[Ryan et al., 2017] Ryan, D. A., Liu, Y. Q., Li, L., et al. (2017). Numerically derived parametrisation of optimal RMP coil phase as a guide to experiments on ASDEX Upgrade. *Plasma Physics and Controlled Fusion*, 59, 024005.

[Sauter, 2016] Sauter, O. (2016). Geometric formulas for system codes including the effect of negative triangularity. *Fusion Engineering and Design*, 112, 633 .

[Sauter et al., 2014] Sauter, O., Brunner, S., Kim, D., et al. (2014). On the non-stiffness of edge transport in L-mode tokamak plasmas. *Physics of Plasmas*, 21, 055906.

[Scarabosio et al., 2013] Scarabosio, A., Eich, T., Herrmann, A., and Sieglin, B. (2013). Outer target heat fluxes and power decay length scaling in L-mode plasmas at JET and AUG. *Journal of Nuclear Materials*, 438, Supplement, S426.

[Scarabosio et al., 2015] Scarabosio, A., Eich, T., Hoppe, F., et al. (2015). Scaling of the divertor power spreading (S-factor) in open and closed divertor operation in JET and ASDEX Upgrade. *Journal of Nuclear Materials*, 463, 49.

[Schmitz et al., 2008] Schmitz, O., Jakubowski, M., Frerichs, H., et al. (2008). Identification and analysis of transport domains in the stochastic boundary of TEXTOR-DED for different mode spectra. *Nuclear Fusion*, 48, 024009.

[Schneider et al., 2000] Schneider, W., McCarthy, P., Lackner, K., et al. (2000). ASDEX Upgrade MHD equilibria reconstruction on distributed workstations. *Fusion Engineering and Design*, 48, 127.

[Sheikh et al., 2016] Sheikh, U., Duval, B., Labit, B., and Nespoli, F. (2016). A novel carbon coating technique for foil bolometers. *Review of Scientific Instruments*, 87, 11D431.

[Sieglin, 2014] Sieglin, B. (2014). *Divertor Power Load Studies in All Metal ASDEX Upgrade and JET*. PhD thesis, TU München.

[Sieglin et al., 2017] Sieglin, B., Eich, T., Faitsch, M., et al. (2017). Assessment of divertor heat load with and without external magnetic perturbation. *Nuclear Fusion*, 57, 066045.

[Sieglin et al., 2016a] Sieglin, B., Eich, T., Faitsch, M., et al. (2016a). Density dependence of SOL power width in ASDEX Upgrade L-Mode. *Nuclear Materials and Energy*, 12, 216.

[Sieglin et al., 2016b] Sieglin, B., Eich, T., Faitsch, M., et al. (2016b). Investigation of scrape-off layer and divertor heat transport in ASDEX Upgrade L-mode. *Plasma Physics and Controlled Fusion*, 58, 055015.

[Sieglin et al., 2013] Sieglin, B., Eich, T., Scarabosio, A., et al. (2013). Power load studies in JET and ASDEX-Upgrade with full-W divertors. *Plasma Physics and Controlled Fusion*, 55, 124039.

[Sieglin et al., 2015] Sieglin, B., Faitsch, M., Herrmann, A., et al. (2015). Real time capable infrared thermography for ASDEX Upgrade. *Review of Scientific Instruments*, 86, 113502.

[Snyder et al., 2011] Snyder, P., Groebner, R., Hughes, J., et al. (2011). A first-principles predictive model of the pedestal height and width: development, testing and iter optimization with the EPED model. *Nuclear Fusion*, 51, 103016.

[Stangeby, 2000] Stangeby, P. C. (2000). *The Plasma Boundary of Magnetic Fusion Devices*. Bristol: Institute of Physics.

[Streibl et al., 2003] Streibl, B., Lang, P. T., Leuterer, F., Noterdaeme, J.-M., and Staebler, A. (2003). Chapter 2: Machine design, fueling, and heating in ASDEX Upgrade. *Fusion Science and Technology*, 44, 578.

[Strumberger, 1996] Strumberger, E. (1996). SOL studies for W7-X based on the island divertor concept. *Nuclear Fusion*, 36, 891.

[Strumberger, 2000] Strumberger, E. (2000). Deposition patterns of fast ions on plasma facing components in W7-X. *Nuclear Fusion*, 40, 1697.

[Strumberger et al., 2014] Strumberger, E., Guenter, S., and Tichmann, C. (2014). MHD instabilities in 3d tokamaks. *Nuclear Fusion*, 54, 064019.

[Sun et al., 2015] Sun, H. J., Wolfrum, E., Eich, T., et al. (2015). Study of near scrape-off layer (SOL) temperature and density gradient lengths with Thomson scattering. *Plasma Physics and Controlled Fusion*, 57, 125011.

[Sun et al., 2016] Sun, Y., Liang, Y., Liu, Y. Q., et al. (2016). Nonlinear transition from mitigation to suppression of the edge localized mode with resonant magnetic perturbations in the EAST tokamak. *Phys. Rev. Lett.*, 117, 115001.

[Suttrop, 2000] Suttrop, W. (2000). The physics of large and small edge localized modes. *Plasma Physics and Controlled Fusion*, 42, A1.

[Suttrop et al., 2011] Suttrop, W., Eich, T., Fuchs, J. C., et al. (2011). First observation of edge localized modes mitigation with resonant and nonresonant magnetic perturbations in ASDEX Upgrade. *Phys. Rev. Lett.*, 106, 225004.

[Suttrop et al., 2009a] Suttrop, W., Gruber, O., Gnter, S., et al. (2009a). In-vessel saddle coils for MHD control in ASDEX Upgrade. *Fusion Engineering and Design*, 84, 290 .

[Suttrop et al., 2009b] Suttrop, W., Hahn, D., Hartmann, J., et al. (2009b). Physical description of external circuitry for resistive wall mode control in ASDEX Upgrade. In *36th EPS Conf. on Plasma Physics*, volume 33.

[Suttrop et al., 2017] Suttrop, W., Kirk, A., Nazikian, R., et al. (2017). Experimental studies of high-confinement mode plasma response to non-axisymmetric magnetic perturbations in ASDEX Upgrade. *Plasma Physics and Controlled Fusion*, 59, 014049.

[Teschke et al., 2017] Teschke, M., Arden, N., Eixenberger, H., et al. (2017). BUSSARD - the high current high bandwidth multiple-phases inverter for ASDEX Upgrade. In *2017 IEEE International Conference on Environment and Electrical Engineering and 2017 IEEE Industrial and Commercial Power Systems Europe (EEEIC / I CPS Europe)*, pages 1–6.

[Teschke et al., 2015] Teschke, M., Arden, N., Eixenberger, H., Rott, M., and Suttrop, W. (2015). Electrical design of the BUSSARD inverter system for ASDEX Upgrade saddle coils. *Fusion Engineering and Design*, 96 - 97, 171 .

[Thornton et al., 2015] Thornton, A., Kirk, A., Cahyna, P., et al. (2015). ELM mitigation via rotating resonant magnetic perturbations on MAST. *Journal of Nuclear Materials*, 463, 723 .

[Thornton et al., 2014] Thornton, A., Kirk, A., Cahyna, P., et al. (2014). The effect of resonant magnetic perturbations on the divertor heat and particle fluxes in MAST. *Nuclear Fusion*, 54, 064011.

[Wagner, 2014] Wagner, F. (2014). Electricity by intermittent sources: An analysis based on the german situation 2012. *The European Physical Journal Plus*, 129, 20.

[Wagner et al., 1985] Wagner, F., Bartiromo, R., Becker, G., et al. (1985). Experimental evidence for neoclassical ion transport effects in the h-transition of ASDEX. *Nuclear Fusion*, 25, 1490.

[Wagner et al., 1982] Wagner, F., Becker, G., Behringer, K., et al. (1982). Regime of improved confinement and high beta in neutral-beam-heated divertor discharges of the ASDEX tokamak. *Phys. Rev. Lett.*, 49, 1408.

[Wenninger et al., 2014] Wenninger, R., Bernert, M., Eich, T., et al. (2014). DEMO divertor limitations during and in between ELMs. *Nuclear Fusion*, 54, 114003.

[Wesson and Campbell, 2011] Wesson, J. and Campbell, D. (2011). *Tokamaks*. International Series of Monographs on Physics. OUP Oxford.

[Willensdorfer et al., 2016] Willensdorfer, M., Denk, S. S., Strumberger, E., et al. (2016). Plasma response measurements of external magnetic perturbations using electron cyclotron emission and comparisons to 3D ideal MHD equilibrium. *Plasma Physics and Controlled Fusion*, 58, 114004.

[Yu et al., 2008] Yu, Q., Guenter, S., Kikuchi, Y., and Finken, K. (2008). Numerical modelling of error field penetration. *Nuclear Fusion*, 48, 024007.

[Zohm, 1996] Zohm, H. (1996). Edge localized modes (ELMs). *Plasma Physics and Controlled Fusion*, 38, 105.

[Zohm, 2010] Zohm, H. (2010). On the minimum size of DEMO. *Fusion Science and Technology*, 58, 613.

Danksagung

Eine experimentelle Doktor-Arbeit in einem Großprojekt bedarf der Zusammenarbeit und Unterstützung vieler Leute. Deshalb geht der größte Dank an die ASDEX Upgrade und TCV Teams, ohne die diese Arbeit nicht möglich gewesen wäre.
Dennoch gibt es einige Leute, denen ich hier besonders danken möchte:

Ich bedanke mich bei meinem Doktorvater Professor Hartmut Zohm, der mir nicht nur die Möglichkeit zu dieser Arbeit gab, sondern mir auch immer mit einem offenen Ohr zur Verfügung stand. Ich möchte mich aber auch für die Freiheiten bedanken, die du mir gegeben hast, durch die ich persönlich sicher viel gelernt habe, auch in dem Wissen, dass du mich einfängst sollte ich die Spur verlieren.

Besonderen Dank bin ich auch Thomas Eich und Bernhard Sieglin verpflichtet. Durch euch kam ich bereits während meiner Masterarbeit zu einer erstklassigen Betreuung. Die tägliche Arbeit mit euch hat meine Doktorarbeit geprägt.

Ich danke der '15 Uhr IR-Besprechung' mit Bernhard Sieglin und Dirk Nille, bei der nicht nur Kaffee getrunken wurde, sondern auch die kleineren und größeren Probleme des (Berufs) Alltags diskutiert wurden.

Speziellen Dank richte ich an Wolfgang Suttrop und Markus Teschke für die Unterstützung beim Einstellen der Stromversorgung für die Störspulen. Ohne euch wären die Studien nicht in diesem Umfang möglich gewesen.

Mit Matthias Willensdorfer, Wolfgang Suttrop, Dominik Brida und Tilmann Lunt konnte ich immer über den Einfuss der Störspulen auf den Plasmarand diskutieren.

Bei Albrecht Herrmann und Elisabeth Wolfrum bedanke ich mich für die Unterstützung während meiner Doktorarbeit.

Ich hatte während dieser Doktorarbeit das Glück auch über den Tellerrand schauen zu dürfen. Dabei traf ich auf ein freundliches und hilfsbereites Team bei TCV. Besonders bedanken möchte ich mich bei Stefano Coda, Roberto Maurizio, Christian Theiler, Holger Reimerdes, Benoit Labit und Antoine Merle des Swiss Plasma Centers sowie Alberto Gallo von CEA Caderache für die Zusammenarbeit bei diesen Experimenten.

Teile dieser Doktorarbeit wurden innerhalb des europäischen MST1 von Eurofusion durchgeführt. Hierfür möchte ich mich bei meinen Ansprechpartnern Matthias Bernert, Antii Hakola und Hendrik Meyer bedanken.

Zuletzt einen Dank an alle, die mich unterstützt haben, die ich unwissentlich in meiner Aufzählung vergessen habe.